# Design and Control of a Portable AO System

## A Continuous Model Based Approach

R.I. van Genderen

Master of Science Thesis

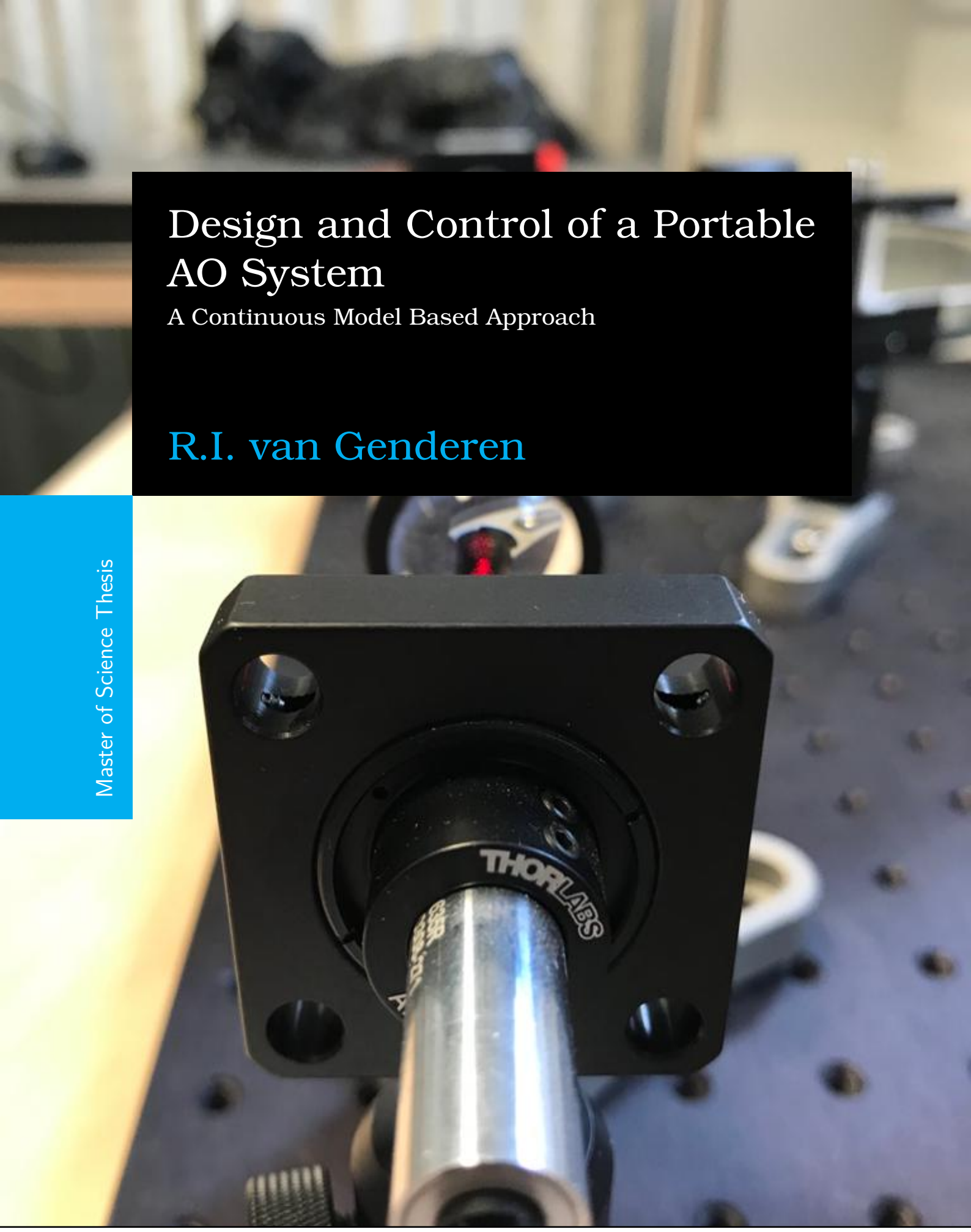


TU Delft Delft University of Technology

Delft Center for Systems and Control

# Design and Control of a Portable AO System

## A Continuous Model Based Approach

Master of Science Thesis

For the degree of Master of Science in Systems and Control at Delft University of Technology

R.I. van Genderen

June 9, 2021

Faculty of Mechanical, Maritime and Materials Engineering (3mE) · Delft University of Technology

The work in this thesis was supported by OKOTech. Their cooperation is hereby gratefully acknowledged.


# Abstract

In the field of Adaptive Optics (AO) a new development has been introduced recently: the Wavefront Sensorless Adaptive Optics (WFSless AO) approach, which only uses camera measurements to optimize image quality and does not use a Shack-Hartman (SH) Wavefront Sensor (WFS) [Booth, 2006, Débarre et al., 2009, Hinnen et al., 2008]. In order to optimize the image quality of a point source or an extended object, the residual wavefront should be minimised as much as possible. The Model Based Approach [Booth, 2007, Linhai and Rao, 2011] is a very promising approach which can be used for this optimisation, resulting in a significant reduction in the amount of measurements. This approach uses an initial measurement and then excites all the modes that need to be optimised separately and takes a measurement of the intensity distribution after each excitation. Then, the Second-Moment (SM)'s of the measured intensity distributions are computed and used for the computation of the optimal control input, which is the coefficient vector in a Zonal representation of the wavefront. The control vector can be used to minimise the residual wavefront and thus optimise the image quality. However, in this approach it is assumed that the incoming wavefront does not change between the first and last measurement. This assumption is called the *frozen window time* and it is not valid for real-time problems. In [Lianghua et al., 2017] a solution was proposed for this problem, by using a precomputed independent set of modes, which allows a decoupling of the modes and computations and reduces the *frozen window time*. Unfortunately, this research introduces more measurements which leads to more delay.

In this thesis a new approach will be presented, the Continuous Model Based Approach. This approach tries to solve both problems simultaneously: a reduction of the number of measurements and a reduction of the frozen window time. The number of measurements will be reduced by combining the excitation and optimisation step and the frozen window time will be reduced by using a two step optimisation, based on [Lianghua et al., 2017]. First, the validity of this approach will be proven mathematically and with simulations, then it will be tested in experiments. In order to make the step to real-time experiments, also an online calibration method will be introduced, proven and tested. This is also a new technique, based on the Model Based Approach [Linhai and Rao, 2011] and can be used to obtain the correlation matrix for any set of modes, focussed on actuator responses.

# Table of Contents

# List of Figures

# Preface

With this thesis I not only finalise my MSc degree in Systems and Control, but also my time as a student. It has been an amazing journey. I have learned so much during the last few years, not only about the incredible world of technology, but also about working on projects and being an engineer. During this project, I really enjoyed the SILly seminars. The discussions with other students greatly impacted the process of my thesis. I want to thank Oleg for organising these seminars and creating a safe environment, where students could ask questions and give and receive feedback. I also want to thank you personally, Oleg for all your help and the nice discussions we had. You were always available when I needed your help and pointed me in the right directions with challenging questions and new insights. I really enjoyed working with you throughout the last year! I want to thank Gleb as well for guiding me through the project. Especially in the beginning, by guiding me to find a topic for my thesis. You showed me that it was my project and thus my decision, which path I wanted to follow. This was the first time that someone really made me choose my own path. I learned a lot during this process.

Throughout the entire project, there have been some people close to me that kept me grounded with both feet. Especially during my eureka moments, when I was feeling a little crazy, Noes you were always there to talk and discuss my ideas. Thank you! I also want to thank my parents for listening to my ideas and keeping me motivated throughout the year. There is also someone who deserves a special thank you. Not only for always listening to me, but also for forcing me to think about my well being and get some rest now and then. You are probably the person that I look up to the most in this world and want you to know that I really appreciate everything you have done for me. Lot, you really helped me through the last year and I could not have done it without you.

Writing this thesis has been an amazing experience and I hope you enjoy reading it.

Yours sincerely,

Delft, University of Technology
June 9, 2021

R.I. van Genderen

# Introduction

In the field of AO a lot of research has been done over the years and the technology of AO-systems has become incredibly complicated, big and expensive [Hinnen, 2007, Hippler, 2019, Spyromilio, 2008]. In order to make this incredible technology accessible to everyone, an implementation must be realized that can be implemented on very simple set-ups (such as telescopes for amateur astronomers) and which corrects for low order aberrations. One way of achieving this, is by implementing a relatively new part of AO, a WFSless AO approach.

In the WFSless AO approach, a metric must be optimised that describes the image quality, such as; the maximum intensity, image sharpness or SM of the intensity distribution [Schutter, 2018, Vorontsov and Carhart, 1997]. In this thesis, first the image quality of a point source is discussed, followed by the proof for extended objects. One of the metrics that is commonly used, is the SM of the intensity distribution of the image [Booth, 2006, Débarre et al., 2009]. For this metric it is proven that the SM of the intensity distribution is proportional to the Mean Squared Gradient (MSG) [Yang et al., 2015]. Using this proportionality, a new method is introduced: the General Model Based approach [Booth, 2007, Linhai and Rao, 2011]. By applying a known aberration to the incoming wavefront and measuring the difference in the intensity distribution, the most optimal control vector is computed. This control vector contains the coefficients for a Zonal wavefront representation, which consists of the set of modes used for the optimisation. With this method, the total number of required measurements is reduced to $N+1$, where $N$ is the number of modes that is accounted for. One of the limitations of this approach is the assumption that the incoming wavefront does not change between the first and last measurement, this assumption is called the frozen window time. In the approach proposed by [Lianghua et al., 2017], this window is reduced significantly and the modes are decoupled. Resulting in a decrease of the computation time for one mode, but an increase in the total number of iterations. Both methods rely on the assumption that the incoming wavefront remains frozen for a certain time, but in more turbulent situations, such as astronomy, this assumption might not hold and more research on dynamic situations is needed.

The first part of this research project was focussed on the design and control of a small portable AO device. In the process of acquiring the required knowledge for this part of research, a niche was found. As discussed above, the *frozen window time* assumption is not valid and it seems scientifically more interesting to look into new ways of solving this problem, before looking at the design and control of the entire system. This thesis will contribute to the field of research by proposing two new methods. First, a new approach for the optimisation process is proposed: the Continuous Model Based Approach, which decreases the *frozen window time*, whilst keeping the total number of iterations as low as possible. The second contribution focusses on the empirical calibration of the system. The empirical calibration procedure is needed for the practical implementation of the experiments, which are conducted to prove the efficiency and reliability of the new proposed method. In order to overcome errors introduced by the experimental setup, such as alignment, focussing or approximation errors (e.g. in the actuator responses), an online empirical calibration procedure is preferred, compared to analytical or numerical calibration procedures. In this thesis a calibration procedure is proposed that computes the correlation matrix of the system, taking into account any errors introduced by the system. The two methods are combined and tested with experiments.

This thesis will be built up in the following way: first an overview of the important literature will be presented. In this part the turbulence model will be discussed, an overview of the research up till now will be presented with all the different components, the used metric and different sets of modes will be evaluated and then two different Model Based Approaches will be introduced. The last part of the literature review focusses on an online mirror calibration procedure and the implementation of an extended object for the different Model Based Approaches. After all the relevant literature has been summarised, the new method will be introduced and the mathematical proof of the new method will be presented. Next, the results of the simulations and experiments will be presented and discussed. Then, a comparison will be made between two existing methods (the General and Synchronous Model Based Approach) and the new proposed method. Lastly, a conclusion will be drawn on the effectiveness and reliability of this new method.

# Part I

# Literature Summary

# Chapter 1

# Turbulence Model

This chapter introduces the reasons, challenges and limitations of the principles of Adaptive Optics (AO). It will explain why stars are not sharp when looking at them and why a very large telescope might not yield images with better quality, compared to smaller telescopes. The basic ideas behind turbulence will be explained first, followed by the representation of the (aberrated) wavefront. Then, the Fried parameter is introduced, as this is an important parameter in the turbulence modelling and in determining the limiting factor for the sharpness of an aberrated image. Besides turbulence, also the diffraction limited resolving power of a telescope is discussed when there would be no turbulence. In the last section, a solution is presented, in order to overcome the deterioration of the image quality due to aberrations introduced by turbulence.

## 1.1 Turbulence modelling

In order to understand the idea of turbulence, first the idea of a wavefront must be explained. When a star emits light, it emits light rays. When these rays are in phase, a line can be

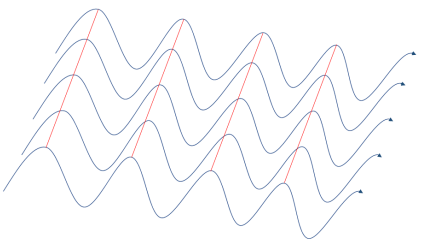

**Figure 1-1:** The blue lines represent light rays and the red lines connect the parts of the waves that are in equal phase. As a reference point, the top of the waves is used.

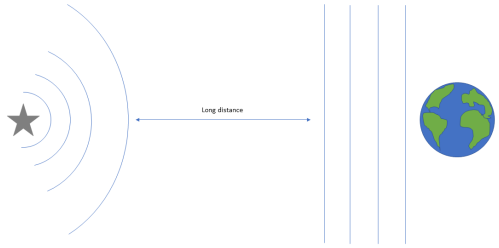


**Figure 1-2:** Example of long propagation distance, making the incoming wavefront flat

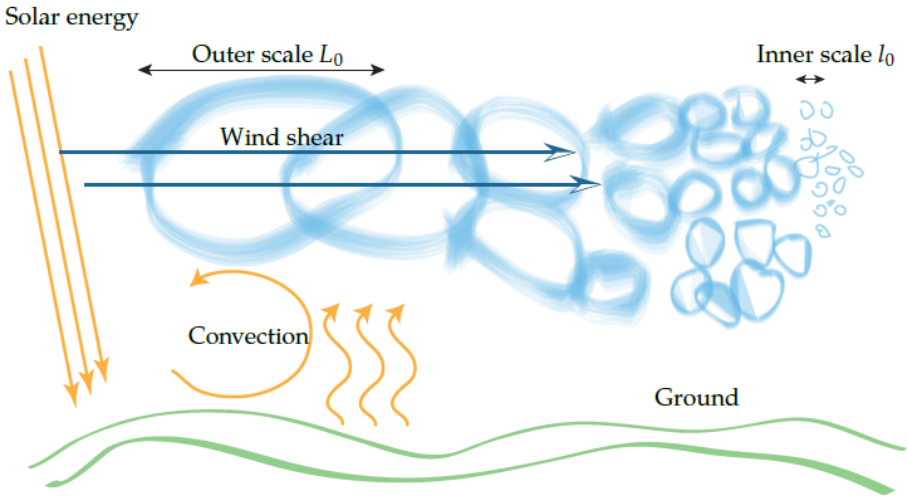


**Figure 1-3:** Example of Kolmogorov turbulence model, from the lecture notes [Verhaegen et al., 2017]

drawn over the part of the waves that is in equal phase. This can be seen in Figure 1-1 in the red lines and it can be extended into the third dimension, where the resulting plane is called a wavefront.
Once a star has emitted the light, it will be in a spherical form. After it has travelled a long distance, it can be assumed that this spherical form can be neglected and the incoming wavefront can be approximated by a planar wavefront. This is visualised in Figure 1-2.

## 1.2 Kolmogorov Turbulance Model

One of the first to discover the relation between image quality and telescope diameter, was Sir Isaac Newton. However, in his research he found that there would also be a certain bound on the performance of the telescope. He blamed the so-called perpetual tremor of the air, which could be observed in the twinkling of stars for example. With this idea, he was one of the first to directly link the turbulence of the air to the deterioration of image quality. Later, Andrey Kolmogorov introduced the theory that the turbulence is a result of bubbles of air

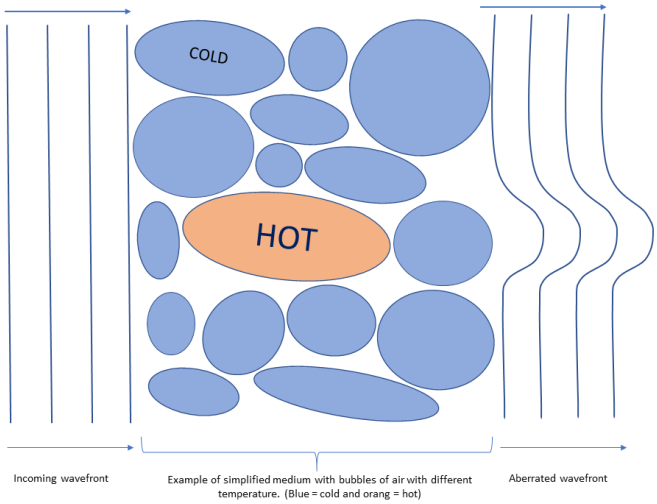


**Figure 1-4:** Example of a wavefront aberration in a simplified form

with different temperatures. These bubbles of air are the result of the absorption of sun light by the earth. The bubbles start big, but then degrade into smaller bubbles and eventually dissipate as heat [Verhaegen et al., 2017], see Figure 1-3. As the warmer bubbles of air have a smaller density, light will move faster through the warmer bubbles, compared to the colder bubbles. This can be explained by computing the *optical path length* of every point in the incoming wavefront [Verhaegen et al., 2017]:

$$\text{OPL} = \int_P n(\mathbf{r})\mathrm{d}\mathbf{r}, \tag{1-1}$$

where $n(\mathbf{r})$ is the refraction index, dependent on position $\mathbf{r}$. This effect creates a difference in the phase as the medium through which the light travels is not homogeneous. This results in an aberration in the incoming wavefront, see Figure 1-4 for an example. Of course, this is only a really simplified aberration and in the real atmosphere the aberration will be much more complex due to the random and dynamic nature of the atmosphere and the turbulence that causes the aberration.

## 1.3 Point Source

The concept of a point source is important for the resolution of a telescope. A star is an example of a point source. If the plane waves of a star reach the telescope and are focussed by a lens, an airy disk can be observed. This airy disk defines the smallest available angular resolution observable and can be computed with the *Rayleigh Criterion*.

## 1.4 Rayleigh Criterion

The *Rayleigh Criterion* describes the angular resolution at which the two airy disks of two different point sources can still be distinguished:

$$sin(\theta) \approx 1.22\frac{\lambda}{D} \tag{1-2}$$

where $\lambda$ is the wave length of the light and D is the diameter of the telescope. Here it can be seen that a larger diameter will also lead to a more detailed image. However, as stated before, after a certain diameter the turbulence will become the limiting factor and active AO is needed to deal with the turbulence and get a higher quality image. This limiting factor will be discussed in the next section.

## 1.5 Fried Parameter

For the phase delay caused by the difference in the OPL, a so-called structure function can be constructed [Tatarskii, 1971, Verhaegen et al., 2017]:

$$D_\phi(\boldsymbol{\xi}) = \langle|\phi(\mathbf{x}) - \phi(\mathbf{x}+\boldsymbol{\xi})|\rangle, \tag{1-3}$$

which can be rewritten into [Roddier, 1999]

$$D_\phi(\boldsymbol{\xi}) = 2.91k^2(cos(\gamma))^{-1}\xi^{5/3}\int C_N^2(h)\mathrm{d}h, \tag{1-4}$$

where $\gamma$ is the Zenith angle and $C_N^2$ is the *Index Structure Coefficient*. This equation can be simplified into

$$D_\phi(\boldsymbol{\xi}) = 6.88\left(\frac{\xi}{r_0}\right)^{5/3}, \tag{1-5}$$

where $r_0$ is the Fried parameter. This parameter can be seen as a sort of measurement for the turbulence and varies between the $5cm$ for high turbulence and $20cm$ for lower turbulence [Verhaegen and Verdult, 2007]. It can be computed with

$$r_0 = \left(0.423k^2(cos(\gamma))^{-1}\xi^{5/3}\int C_N^2(h)\mathrm{d}h\right)^{-3/5} \tag{1-6}$$

and it is used for several different computations, e.g. the Strehl ratio or the Power Spectral Density (PSD). The PSD will bediscussed in the next section.

## 1.6 Power Spectral Density

The PSD of the Kolmogorov turbulence model is computed using [Noll, 1976]

$$\Phi(f) = 0.023r_0^{-3/5}f^{-11/3}, \tag{1-7}$$

where

$$f = \sqrt{f_x^2 + f_y^2 + f_z^2}, \tag{1-8}$$

which denotes the spatial frequency. When the spatial frequency becomes very small, the PSD goes to infinity. To overcome this problem, an adapted version is introduced: the modified Von Kármán turbulence model with the PSD defined as [Verhaegen et al., 2017]

$$\Phi(f) = \frac{0.023 r_0^{-\frac{5}{3}}}{\left(f^2 + f_0^2\right)^{\frac{11}{6}}} \mathrm{e}^{-\left(\frac{f}{f_i}\right)^2}. \tag{1-9}$$

The PSD can be used to compute the *Resolving power* $\mathcal{R}$. This can be used to find the limiting factor in the process of finding the highest quality image and is computed using:

$$\mathcal{R} = \int \Phi(f) \mathrm{d}f = \int T(f) B(f) \mathrm{d}f, \tag{1-10}$$

where $T(f)$ is telescope transfer function and $B(f)$ the *spectrum* of the wavefront aberration. The last part of Equation 1-10 can be used to find the limiting factor in the process and this is described in the next section.

## 1.7 Limiting Factor Image Quality

As can be seen in Equation 1-10, either the turbulence or the telescope diameter is the limiting factor for obtaining higher quality images. If the wavefront is assumed to be flat, i.e. there is no aberration, then $B(f) = 1$ and the limiting factor will be the *Resolving Power* of the telescope. This is called the diffraction limited case. On the other hand, if there is an aberration (induced by turbulence) and the telescope is assumed to be significantly large, the *Resolving Power* is assumed to be limited by the turbulence, which is then related to the Fried parameter.

## 1.8 Single or Multi Layer Turbulence Approximation

Due to the random and dynamic behaviour of the turbulence, it is very difficult to simulate it. One of the approximations that has been widely used in the literature, was proposed by Taylor, [Taylor, 1969]. He approximates the turbulence as a frozen flow and shows the correlation between two fixed points at various wind speeds. Using this approach, the turbulence can be modelled as one or more fixed layers that move over the aperture of the telescope with different wind speeds and directions [Hinnen, 2007]. A schematic overview of a one layered turbulence approximation can be seen in Figure 1-5 and comes from [Hinnen, 2007]. If a one layer turbulence is assumed, the process can be described by a Vector Auto-Regressive (VAR) model. If a first order VAR model is implemented the proces becomes:

$$\phi(k+1) = A\phi(k) + w(k), \tag{1-11}$$

where $w(k)$ represents the process noise and $A$ the system matrix of this process. A lot of research has been done on acquiring this matrix and solutions can be found in many textbooks, e.g. [Verhaegen and Verdult, 2007]. For the dynamic turbulence the OOMAO [Conan and Correia, 2014] toolbox in matlab is used to create moving window turbulence models.

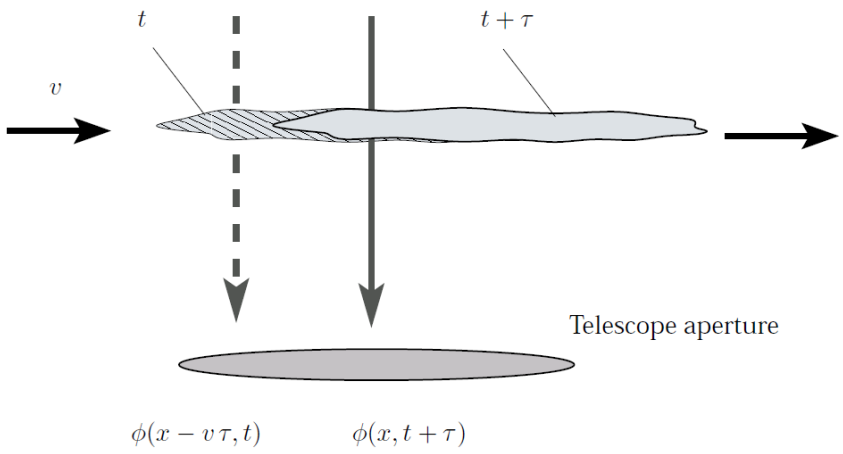


**Figure 1-5:** One layer turbulence approximation from [Hinnen, 2007]

## 1.9 Wavefront Representation

For simulations, it is important to generate, describe and compute the incoming wavefront. A very common way of constructing the incoming wavefront is by a combination of modes, such as the Zernike polynomials [Dai, 1995] or the Lukosz-Braat polynomials [Booth, 2007]. The incoming wavefront can be described by

$$\psi(x,y) = \sum_{i=1}^{\infty} \nu_i F_i(x,y), \tag{1-12}$$

where $\nu_i$ is the coefficient corresponding to the $i^{th}$ mode of the chosen set $F_i(x,y)$. In chapter 4, several different modes and their characteristics will be discussed and compared. The coefficients of a wavefront can be estimated using a minimal least squares approach [Fried, 1977], which is discussed in Appendix D and in [Verhaegen and Verdult, 2007].

## 1.10 Root Mean Squared Error

In order to compare the residual wavefront the Root Mean Squared Error (RMSE) of the residual wavefront can be computed. This value can be used as a measure for the quality of the residual wavefront and can be computed with

$$RMSE = \sqrt{\frac{1}{A}\sum_{i=1}^{N}\sum_{j=1}^{M} P(i,j)(\phi(i,j) - \phi_{DM}(i,j))^2}, \tag{1-13}$$

where A is the area of the aperture $P(x,y)$ and M and N are respectively the x- and y-dimensions of the matrix that is used to describe the wavefront.

# Chapter 2

# WFSless AO Setup and Components

To optimise the image quality of a point source or an extended object, a Wavefront Sensorless Adaptive Optics (WFSless AO) approach can be used. There has been a lot of research in this field of science [Booth and Jesacher, 2013, Pozzi et al., 2017, Song et al., 2010] and many more. In this Chapter an overview of this field of science will be given. First a general overview will be given (section 2.1), followed by the different elements used in the setup.

## 2.1 General Overview of WFSless AO

In the WFSless AO approach, the Wavefront Sensor (WFS) is left out of the system and the camera measurements are used as an input to find the most optimal control vector for the Deformable Mirror (DM). In Figure 2-1, the general setup of a WFSless AO configuration is shown. It can be seen that the WFS is left out of the setup and that the only available sensor is the CCD-sensor. The CCD-sensor measures the intensity and this intensity measurement is used as an input for the controller. A disadvantage of this method is that the intensity measurement can not be used directly for wavefront correction. A lot of iterations are needed to find the optimal control and combined with the delay that every iteration introduces, this can add up to a significant delay. This becomes a problem when the incoming aberration is not static, but dynamic or time-varying, such as in astronomy. Another important challenge of this approach is to find the global optimum and avoid getting stuck in a local optimum.

## 2.2 Deformable Mirror

For this thesis a 17channel Tip/Tilt MicroMachinedDM from OKOTECH is available [OKO Technologies, 2011]. This is a DM designed for correcting low-order aberrations in the incoming wavefront. This DM has a maximum update frequency of $1kHz$ and a maximum stroke of $9.4\mu m$. The actuator configuration can be seen in Figure 2-2. Using the actuator responses

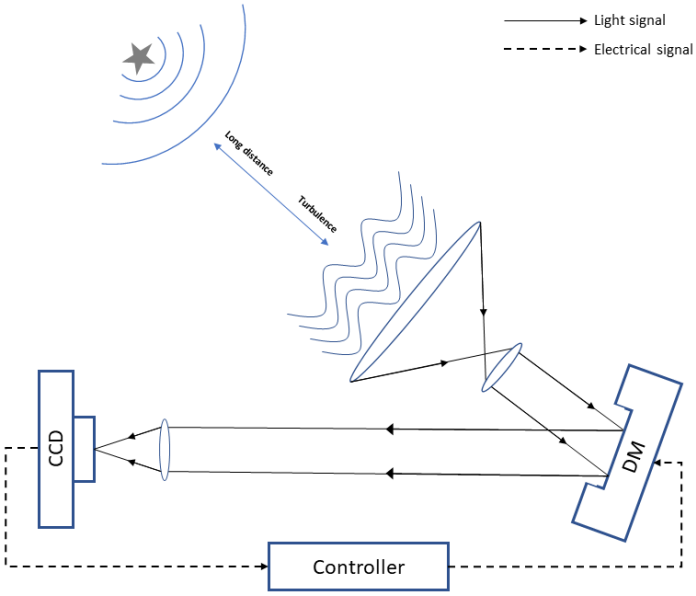


**Figure 2-1:** Overview of WFSless AO configuration

in Figure 4-1, it is assumed that one can simulate all the possible aberrations in the span of this DM by a linear combination of the actuator responses:

$$\phi_{DM}(x,y) = \sum_{i=1}^{N} \nu_i E_i(x,y), \tag{2-1}$$

where $\nu_i$ is the coefficient corresponding to the $i^{th}$ actuator response $E_i(x,y)$. It should be noted however, that the introduced phase delay introduced by the DM is computed with

$$\Delta\phi_{DM}(x,y) = 2\frac{\Delta l(x,y)2\pi}{\lambda}, \tag{2-2}$$

where $\Delta l(x,y)$ is the deformation of the DM in meters at $(x,y)$ and $\lambda$ is the wavelength of the incoming wavefront in meters. The factor 2 comes from the path that the light travels. If the DM is retracted, the light has to travel this path twice (towards the DM and away from the DM), so the introduced phase delay is multiplied with a factor 2.

## 2.3 Membrane DM

Because a membrane DM is used, not the full aperture can be used for the approximation, but only a small part. This aperture can be simulated as

$$P(x,y) = \begin{cases} 1, & r \leq |R| \\ 0, & r > |R| \end{cases}, \tag{2-3}$$

where $R$ is the recommended radius of the MMDM and

$$r = \sqrt{(x-x_0)^2 + (y-y_0)^2}. \tag{2-4}$$

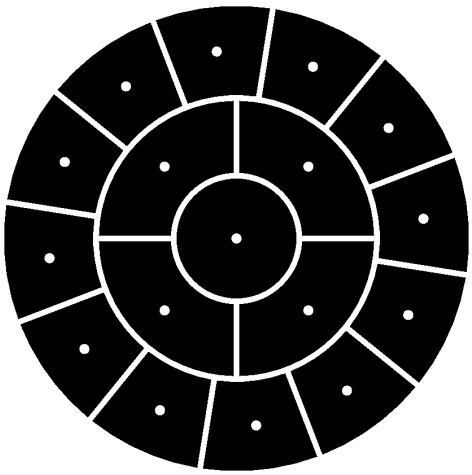

**Figure 2-2:** Actuator positions of 17 actuator MMDM of OKOtech bv.

**(a)** Full aperture of the DM **(b)** Recommended (small) beam diameter

**Figure 2-3:** Two apertures for the DM. The right picture shows the recommended beam diameter and the left shows the full aperture.

This is due to the borders, where the membrane of the DM is attached to the machine itself. Therefore, these borders can not move and it is recommended to only use a smaller diameter. This is visualized in Figure 2-3.

## 2.4 CCD Camera

The only available sensor in this setup will be the CCD-sensor. This sensor measures the light intensity and this is used as an input for the controller. The sensor that will be used for this project is UI-154xLE-M. The specifications can be found in Figure 2-4

## 2.5 Noise Implementation

Noise measured by the CCD camera consists of a combination of read-out noise and shot-noise [Piscaer et al., 2020]:

$$v(k) = v_{shot}(k) + v_{read}(k), \tag{2-5}$$

where $v(k)$ is the measurement noise, $v_{shot}(k)$ the shot noise and $v_{read}(k)$ the read-out noise. The shot noise can be approximated as a Poisson distribution: $(y_{true}(k) + v_{shot}(k)) \sim$

**Table 1: Key Performance Parameters**

| Parameter | | Value |
|---|---|---|
| Optical format | | 1/2-inch (5:4) |
| Active imager size | | 6.66 mm (H) x 5.32 mm (V) |
| Active pixels | | 1,280 H x 1,024 V |
| Pixel size | | 5.2 µm x 5.2 µm |
| Shutter type | | Electronic rolling shutter (ERS) |
| Maximum data rate/ master clock | | 48 MPS/48 MHz |
| Frame rate | SXGA (1280 x 1024) | 30 fps progressive scan; programmable |
| ADC resolution | | 10-bit, on-chip |
| Responsivity | | 2.1 V/lux-sec |
| Dynamic range | | 68.2 dB |
| $SNR_{MAX}$ | | 45 dB |
| Supply voltage | | 3.0 V–3.6 V, 3.3 V nominal |
| Power consumption | | 363 mW at 3.3 V (operating); 294 µW (standby) |
| Operating temperature | | 0°C to +70°C |
| Packaging | | 48-pin CLCC |

**Figure 2-4:** List of the specifications of the UI-154xLE-M camera, which can be found on the website: https://www.1stvision.com/cameras/sensor_specs/MT9M001-D.pdf, [Semiconductor]

$Pois(y_{true})$. The read-out noise is a gaussian distributed noise: $v_{read}(k) \sim \mathcal{N}(0, \sigma_r^2 I)$. In simulations, this is implemented as the Signal to Noise Ratio (SNR). Where the SNR is computed as a percentage of the mean of the intensity distribution.

## 2.6 Control Algorithm

The control algorithm in a WFSless AO approach uses the measurements from the CCD camera directly. Some examples are optimisation algorithms, such as step search or Stochastic Gradient Descent (SGD), a model based approach or a prediction method, such as a Kalman filter [Piscaer et al., 2019, 2020]. The optimisation algorithms aim to optimise a certain metric, that describes the quality or a feature of an image or point source. The main disadvantages of these optimisation algorithms is that the number of iterations is relatively high and it is not always the global optimum that is found. The model-based approach on the other hand converges to the optimal solution relatively fast and two implementations will be discussed in chapter 5 and chapter 6.

# Chapter 3

# Second Moment of the Intensity distribution

In order to compare the quality of images, a metric can be used. These metrics are used by the optimisation algorithms and the characteristics of the metrics are important for the number of iterations. There are several different metrics that can be used, such as the maximum intensity metric, the sharpness, the Strehl ratio and the Second-Moment (SM) based metric . The choice for the most optimal metric is based on the requirements for the system and it is important to choose a metric that has its most optimal value when there is no aberration. Another important feature is convexity of the metric. The metric should be convex in order to find the most optimal value and not get stuck in a local optimum. The metric that will be extensively discussed, the SM-metric, will be used throughout the rest of this thesis due to the important properties, which will be discussed in more detail this chapter and in Appendix A for point sources and Appendix B for extended objects.

## 3.1 Intensity distribution of a point source

Because a Wavefront Sensor (WFS) is excluded from the system, another input is needed for the control algorithm. One of the features of light that can be measured is the intensity distribution of the incoming light and it can be measured by a simple CCD-sensor. In this section a mathematical expression for the intensity distribution for a point source is derived. In chapter 8 and in Appendix B a derivation on the intensity distribution for an extended object will be discussed. The intensity distribution can be described by the convolution of the Point Spread Function (PSF) and the object or light distribution $o(x, y)$ of the real object

$$i(x, y) = h(x, y) * o(x, y), \tag{3-1}$$

where $i(x, y)$ is the 'to be quantified' intensity distribution. When the object is a point source, e.g. a star, described by the delta function $\delta(x, y)$, Equation 3-1 simplifies to:

$$i(x, y) = h(x, y) * \delta(x, y) \tag{3-2}$$
$$i(x, y) = h(x, y). \tag{3-3}$$

Now the intensity distribution can be described by $h(x, y)$, which is the PSF of the aberration and it can be computed using:

$$i(x, y) = |\mathcal{F}(aP(u, v)e^{-i\phi(u,v)})|^2, \tag{3-4}$$

where $(u, v)$ are the coordinates in the pupil plane and $P(u, v)$ is the aperture discussed in section 2.3. Using the intensity distribution, metrics can be used for optimisation, such as the maximum intensity, image sharpness or SM of the intensity distribution.
It should be taken into account that this derivation uses a point source as an object image. However, if an extended source is to be optimized, several extra steps need to be taken before it can be described by a metric and optimised. These steps will be described in chapter 8 and Appendix B.

## 3.2 Second-Moment Based Metric

One of the metrics that first led to a significant decrease in number of iterations was the SM based metric. This metric uses the intensity measurement of the image and computes its second moment. The intensity can computed using the Fourier transform of the image and its phase and can be found in Equation 3-4. In real life experiments, the intensity distribution can be simply measured with a CCD-sensor. The SM is computed with

$$J_{SM}(I) = \frac{\sum_{i,j} I(i, j) \cdot ((i - x_0)^2 + (j - y_0)^2)}{\sum_{i,j} I(i, j)}, \tag{3-5}$$

where $x_0$ and $y_0$ represent the computed centroids of the intensity measurement and must be computed first:

$$x_0(i, j) = \frac{\sum_{i,j} I(u, v) \cdot i}{\sum_{u,v} I(u, v)}, \tag{3-6}$$
$$y_0(i, j) = \frac{\sum_{i,j} I(u, v) \cdot j}{\sum_{u,v} I(u, v)}. \tag{3-7}$$
$$\tag{3-8}$$

This metric exhibits parabolic behaviour, which can be observed through the quadratic terms in the formula. This metric is the basis for one of the important developments in this field of research. It is used as a metric in the general model based approach and for the Masked Detector Signal (MDS). In chapter 5, Appendix A and Appendix B the derivation of this method can be found. This metric can be used to extend these methods from point sources to extended objects, which is briefly discussed in chapter 8 and more elaborate in Appendix B.

# Chapter 4

# Mode Selection

When optimising the image quality of a point source or an extended object, actually the coefficient vector or combination of a set of modes is optimised. An intuitive example for this set of modes is the set of actuator responses, as the control vector directly represents a combination of these responses. The actuator responses can be seen in Figure 4-1. In [Linhai and Rao, 2011], it is stated that any set of modes can be used for optimisation. However, not all sets will be the most optimal bases [Booth, 2007, Debarre et al., 2007, Soloviev, 2020] and in Wang and Booth [2009] and optimal set of modes is proposed. There are several sets of modes that exhibit different features in orthogonality in the direct functions or in the gradients of these functions. It must be noted however, that the computed optimal control vector must converted to a voltage vector, if a set is used that is not the set of actuator responses, before applying it to the Deformable Mirror (DM). In this section the features of the different sets will be discussed and some well known sets will be evaluated, comparing the discussed features. It should be taken into account that these sets are used to approximate the incoming wavefront, because the adaptive element might not be able to represent the incoming wavefront entirely. This will be discussed in the last section of this chapter.

## 4.1 Wavefront Representation of the DM

As discussed in section 1.9, the incoming wavefront can be described by a combination of modes, when modelling the system for a simulation. However, the DM is usually not able to represent an infinite amount of polynomials and its span is bounded by the number of actuators and their positioning. So, when trying to represent the incoming wavefront, there will always be a part that is orthogonal to the span of the DM. This can be described by

$$\phi(x, y) = \phi_{DM}(x, y) + \phi_{\perp}(x, y), \tag{4-1}$$

where $\phi_{DM}$ is the part of the wavefront that can be modelled by the DM and $\phi_{\perp}$ is the part orthogonal to the wavefronts represented by the DM. So, in order to find the most optimal set of modes, this orthogonal part must be minimized. In the next section two performance characteristics for this minimisation are proposed.

## 4.2 Orthogonality of the set of modes

There are several things that can be used to compare the performance of a set of modes. In [Soloviev, 2020], two *rms* residuals are proposed: the *rms* of the residual wavefront and the *rms* of the residuals of the gradients of the wavefront. The idea is to find a set of modes that minimises the *rms* of both residuals.

To compute the orthogonality of a set of modes, a correlation matrix can be computed. This can be done for the set itself and for the gradients of the set. The following equations can be used for the polynomials and the gradients of the polynomials respectively:

$$K_{i,j} = \frac{1}{R} \iint_R [F_i(x,y)F_j(x,y)]\, dxdy, \tag{4-2}$$

$$S_{i,j} = \frac{1}{R} \iint_R \left[ \frac{\partial}{\partial x} F_i(x,y) \frac{\partial}{\partial x} F_j(x,y) + \frac{\partial}{\partial y} F_i(x,y) \frac{\partial}{\partial y} F_j(x,y) \right] dxdy. \tag{4-3}$$

The result is a matrix, which displays the correlation between the different modes. If this matrix is diagonal, the set of modes is orthogonal. However, the correlation matrices of both the polynomials and their gradients should exhibit the diagonal behaviour in order for the set to be orthogonal. In the next sections four examples for different sets of modes will be presented. In section 6.1 it will be explained what the advantages of an orthogonal set are.

## 4.3 Actuator Responses

For the set of modes that can be used for the optimisation algorithms, a very common and intuitive choice is the set of actuator responses. In Figure 4-1 one can see the actuator responses of a 17-actuator MMDM, a DM from OKOtech with an actuator positioning that can be seen in Figure 2-2. The responses of the actuators are an intuitive base to chose and together they span the base of all possible wavefronts that can be represented by the DM. The correlation matrices of this set are computed and can be seen in Figure 4-2. It can be seen that the matrices are not diagonal. This implies that these modes are not orthogonal. Especially between the first five actuators a lot of correlation is observed, which can be explained by looking at the actuator responses in Figure 4-1. The first 5 actuator responses look similar. The correlation between the modes and the gradients of the modes suggests that this might not be the most optimal set of modes to use for optimisation.

## 4.4 Zernike Polynomials

Another example of a set of modes is the set of Zernike Polynomials [Hernández-Gómez et al., 2014]. These polynomials exhibit orthogonal behaviour in the polynomials itself. This can be seen in Figure 4-3, where the left picture shows a matrix with only non-zero elements on the diagonal. The gradients of the Zernike polynomials are not uncorrelated, see the right plot in Figure 4-3. The Zernike Polynomials are frequently used for wavefront representation, when a modal representation is used. In Appendix C, the Zernike and LB-polynomials are shown and evaluated in more detail. The polynomials will be shown, together with their correlation matrices.

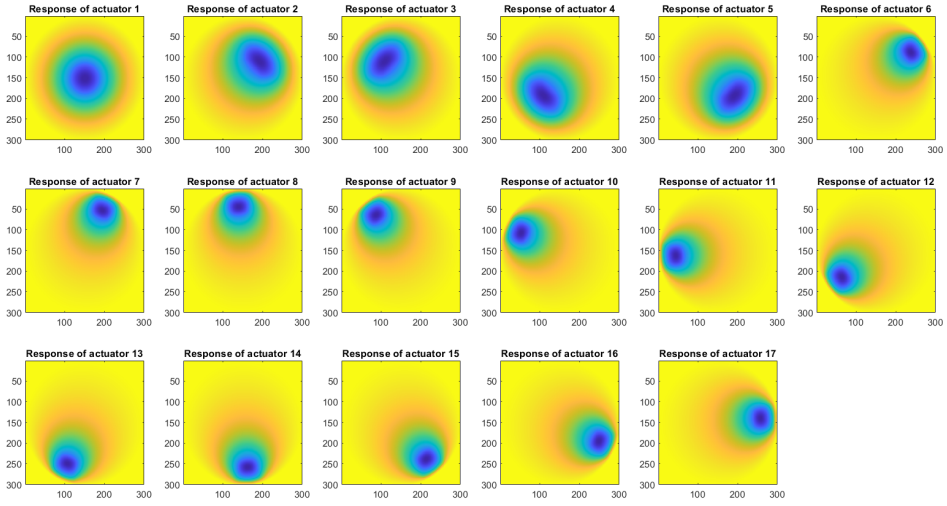


**Figure 4-1:** Actuator responses of 17 actuator MMDM of OKOtech bv.

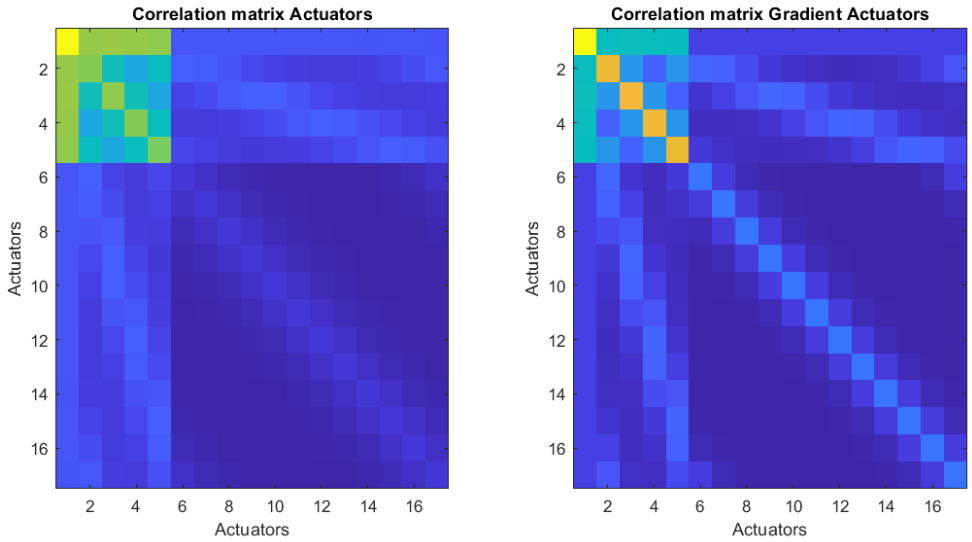


**Figure 4-2:** Correlation matrix of the actuator responses (left) and the correlation matrix of the gradients of the actuator responses (right), both computed with the optimal aperture, which can be seen in Figure 2-3b

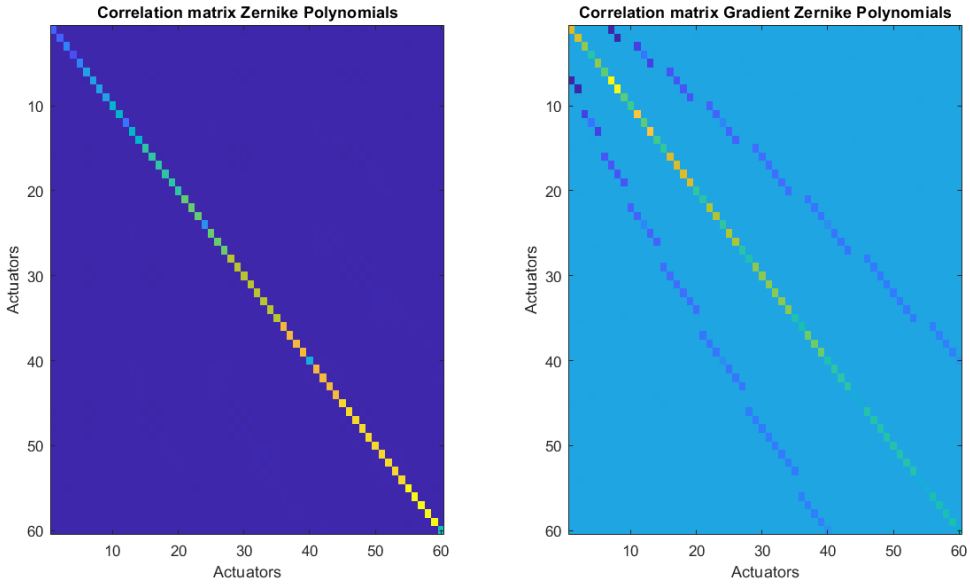


**Figure 4-3:** Correlation matrix of the Zernike Polynomials (left) and the correlation matrix of the gradients of the Zernike Polynomials (right)

## 4.5 Lukosz-Braat Polynomials

Using the approach described in [Debarre et al., 2007], the conversion matrix can be computed, which yields the LB polynomials which can be found in Appendix C. Another approach can be by using the Cholensky decomposition [Soloviev, 2020].

## 4.6 Representing the polynomials with a low order DM

In this section the representation of the Zernike- and LB-polynomials by a low-order DM will be discussed. If the polynomials are used as a bases for optimisation, it is important to check if these polynomials can be represented well enough or if there is a need for an optimised basis based on the actuator responses. In order to answer that question, it must be noted that this DM is a membrane based DM and is thus fixed at the borders of the mirror. In order to use the mirror in the most optimal way, only a small part can be used. This means that also the polynomials and their representations will be evaluated in this 'smaller' region. The approximations are made using a linear least squares approximation, discussed in Appendix D. In Appendix C, the representation of the Zernike and LB-polynomials will be evaluated in more detail. In Figure C-3, the representations of the Zernike polynomials by the DM are plotted for the first 18 polynomials, excluding the piston term. In Figure C-4, the representations of the LB polynomials by the DM are plotted for the first 18 polynomials, excluding the piston term. In order to see if this approximation can be used, also the correlation matrices are computed for the normal Zernike and LB polynomials and their gradients and the representations by the DM of the Zernike and LB polynomials and their gradients. These matrices can be seen in Figure C-5 and Figure C-6.

For the Synchronous Model Based approach, it is important to choose an independent basis. In this section the main disadvantage of a basis with a non-diagonal correlation matrix of the gradients will be discussed. The actuator responses or the Zernike Polynomials are examples of bases that have non-diagonal gradient-based correlation matrices. Due to cross-correlation between the different modes in these sets, the optimal solution for the control vector (computed with Equation 5-19) is computed by solving a set of linear equations. This implies that all the modes must be excited and measured before Equation 5-19 can be solved. This means that the total time between the first measurement and the last measurement is dependent on the total number of modes. In Figure 5-1 a schematic representation of the procedure is displayed. In this picture also the *Frozen Window Time* is introduced, which is an important assumption for this approach. The *Frozen Window Time* lasts from the initial measurement until the computation of the optimal control vector and it is assumed that the incoming wavefront does not change over this period of time. This assumption is needed, because the set of linear equations can not be solved if the incoming wavefront were to change. In section 5.3 the validity of this assumption will be discussed.

In the method proposed by [Booth, 2007], the Lukosz-Braat polynomials are used as the set of modes. This basis has a diagonal correlation matrix for the gradients of the polynomials. However, it should be taken into account that the DM should be able to represent these polynomials. In the case of a low-order DM, such as the 17channel MMDM from OKOTech, this might not be possible (as explained in section 4.6) and the optimal modes should be computed using a method proposed by [Lianghua et al., 2017]. This method finds the most optimal modes using a Singular Value Decomposition (SVD) of the correlation matrix of the gradients of the actuator responses. In section 6.1, the derivation of the most optimal modes is given. For the derivation of the General Model Based Approach, also other sets of modes can be used, such as the actuator responses or Zernike/Lukosz-Braat polynomials.

## 4.7 An Independent Set of Modes

In [Lianghua et al., 2017], a set is proposed that exhibits the features of an independent set. This means the the correlation matrix (or cross-talk matrix) is diagonal. Using an independent set has some benefits, compared to non-indendent sets. This will be explained in chapter 6. As could be seen in Figure 4-2, the set of actuator responses is not an independent set of modes. The Lukosz-Braat Polynomials are an example of an analytical independent set. Another way of finding a suitable set of modes for this method is using the actuator responses as a basis and compute an orthogonal set from these responses numerically. In Figure 4-2 it was observed that the actuator responses itself are not an independent set of modes. This implies that there is always some influence on other modes when updating 1 specific mode. In order to decouple the actuator responses or make the modes fully independent, a singular value decomposition of the correlation matrix is computed such that:

$$L = U^{-1}S(V^T)^{-1}, \tag{4-4}$$

where $L$ is a diagonal matrix and $U$ can be used to find the new set of modes corresponding to $L$, $G(x, y)$:

$$G(x, y) = U^{-1}F(x, y), \tag{4-5}$$

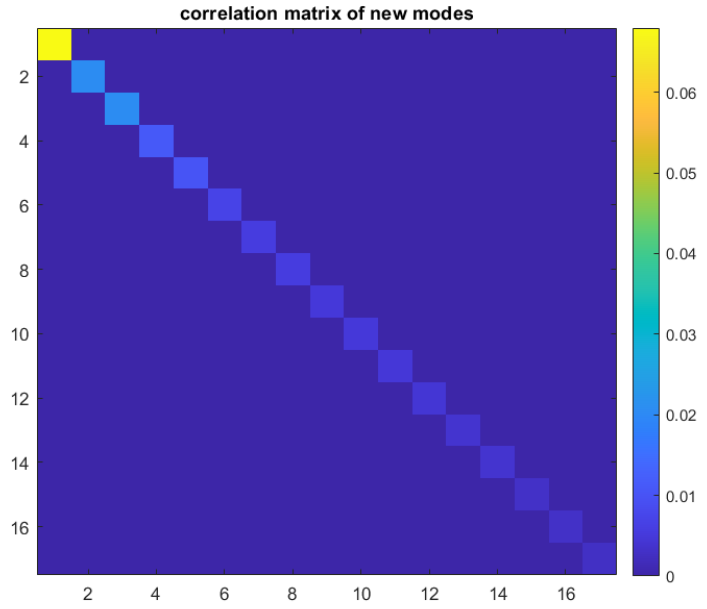


**Figure 4-4:** Correlation matrix of the new independent modes

where $F(x, y)$ represents the set of actuator responses. Plotting $L$ yields the expected correlation matrix, i.e. a diagonal matrix, see Figure 6-1. In Figure 6-2, the responses of the new modes can be found and it can be seen that they are very different from the original actuator responses.

# Chapter 5

# A General Model Based Approach

Using an approach proposed by M.J. Booth [Booth, 2006], an optimal solution could be found in $N+1$ iterations, where $N$ is the number of modes in the chosen set. The General Model Based Approach is a method that uses the proportionality discussed in Appendix A of light in order to compute the optimal solution. In order to apply this method several steps must be taken, proposed by [Linhai and Rao, 2011], which will be explained in the following section. Also, the proportionality of the change in the intensity distribution and the Mean Squared Gradient (MSG) [Yang et al., 2015] is used. This proportionality is proven and written out in Appendix A for completeness and because this is a very important relation for this approach:

$$\int_{\mathbb{R}^2} \left(I(\mathbf{u}) - I_0(\mathbf{u})\right) \mathbf{u}^2 \mathrm{d}\mathbf{u} = \frac{a^2}{4\pi^2} \int_{\mathbb{R}^2} P(\mathbf{x})^2 \left|\bigtriangledown \phi(\mathbf{x})\right|^2 \mathrm{d}\mathbf{x}, \tag{5-1}$$

which can then be normalized by dividing it by the total power, where it is assumed that the sum of the intensity does not change over time:

$$\int_{\mathbb{R}^2} I(\mathbf{u}) \mathrm{d}\mathbf{u} = \int_{\mathbb{R}^2} i_0(\mathbf{u}) \mathrm{d}\mathbf{u} = \int_{\mathbb{R}^2} a^2 P(\mathbf{x})^2 \mathrm{d}\mathbf{x} \tag{5-2}$$

and written as:

$$\frac{\int_{\mathbb{R}^2} \left(I(\mathbf{u}) - I_0(\mathbf{u})\right) \mathbf{u}^2 \mathrm{d}\mathbf{u}}{\int_{\mathbb{R}^2} I(\mathbf{u}) \mathrm{d}\mathbf{u}} = \frac{a^2}{4\pi^2} \frac{\int_{\mathbb{R}^2} P(\mathbf{x})^2 \left|\bigtriangledown \phi(\mathbf{x})\right|^2 \mathrm{d}\mathbf{x}}{\int_{\mathbb{R}^2} a^2 P(\mathbf{x})^2 \mathrm{d}\mathbf{x}}. \tag{5-3}$$

## 5.1 Masked Detector Signal

The metric used for optimisation is based on the Second-Moment (SM)-metric explained in section 3.2 and this metric lead to the Masked Detector Signal (MDS), which is introduced in [Linhai and Rao, 2011] and can be computed with

$$\mathrm{MDS} = \frac{\iint_{x,y} I(x,y) \left(1 - \frac{|r|^2}{R^2}\right) \mathrm{d}x\mathrm{d}y}{\iint_{x,y} I(x,y) \mathrm{d}x\mathrm{d}y}, \tag{5-4}$$

which is only integrated over the area where $r < R$, where $R$ is a suitably chosen Detector radius and it should be weighted by the system's Diffraction Limitation. The value for $r$ can be computed with

$$r = \sqrt{(x_i - x_0)^2 + (y_i - y_0)^2}, \tag{5-5}$$

where $x_0$ and $y_0$ represent the centroids computed using Equation 3-6.

## 5.2 N+1 Iteration Solution

In order to come up with the most optimal control vector, the proportionality between the MSG and the difference in the SM of the intensity measurement will be used. In this approach, a known aberration ($\beta F(x,y)$) is added to the incoming wavefront ($\phi(x,y)$) [Booth, 2007, Linhai and Rao, 2011]

$$\varepsilon(x,y) = \phi(x,y) + \beta F_i(x,y), \tag{5-6}$$

where $F_i(x,y)$ represents the $i$-th mode in the chosen set of modes, e.g. the actuator responses or Zernike polynomials, and $\beta$ a predetermined coefficient. Now the difference in the SM of the intensity distribution is measured and computed with

$$w_{i,init} \approx SM_i - SM_{init}, \tag{5-7}$$

where $SM_i$ represents the new measured SM and $SM_{init}$ the initial measurement. Both SM's are equal to the corresponding MSG's and can be written as:

$$SM_i - SM_{init} = \frac{1}{R}\int_R \left[\left(\frac{\partial}{\partial x}\varepsilon(x,y)\right)^2 + \left(\frac{\partial}{\partial y}\varepsilon(x,y)\right)^2\right] - \frac{1}{R}\int_R \left[\left(\frac{\partial}{\partial x}\phi(x,y)\right)^2 + \left(\frac{\partial}{\partial y}\phi(x,y)\right)]^2\right] dxdy, \tag{5-8}$$

where Equation 5-6 can be substituted for $\varepsilon(x,y)$, resulting in

$$\begin{aligned} SM_i - SM_{init} = {} & \frac{1}{R}\int_R \left[\left(\frac{\partial}{\partial x}\phi(x,y) + \beta\frac{\partial}{\partial x}F_i(x,y)\right)^2 + \left(\frac{\partial}{\partial y}\phi(x,y) + \beta\frac{\partial}{\partial y}F_i(x,y)\right)^2\right] dxdy \\ & - \frac{1}{R}\int_R \left[\left(\frac{\partial}{\partial x}\phi(x,y)\right)^2 + \left(\frac{\partial}{\partial y}\phi(x,y)\right)^2\right] dxdy \qquad (5\text{-}9) \\ = {} & \frac{1}{R}\int_R \left[\left(\frac{\partial}{\partial x}\phi(x,y)\right)^2 + 2\beta\frac{\partial}{\partial x}F_i(x,y)\frac{\partial}{\partial x}\phi(x,y) + \beta^2\left(\frac{\partial}{\partial x}F_i(x,y)\right)^2\right. \\ & \left. + \left(\frac{\partial}{\partial y}\phi(x,y)\right)^2 + 2\beta\frac{\partial}{\partial y}F_i(x,y)\frac{\partial}{\partial y}\phi(x,y) + \beta^2\left(\frac{\partial}{\partial y}F_i(x,y)\right)^2\right] dxdy \\ & - \frac{1}{R}\int_R \left[\left(\frac{\partial}{\partial x}\phi(x,y)\right)^2 + \left(\frac{\partial}{\partial y}\phi(x,y)\right)^2\right] dxdy. \qquad (5\text{-}10) \end{aligned}$$

Using linearity of integrals, which states that any integral of linear terms can be represented by a linear combination of the integrals of the terms.

$$\begin{aligned} SM_i - SM_{init} = \; & \frac{1}{R}\int_R \Bigg[ \cancel{\left(\frac{\partial}{\partial x}\phi(x,y)\right)^2} + 2\beta\frac{\partial}{\partial x}F_i(x,y)\frac{\partial}{\partial x}\phi(x,y) + \beta^2\left(\frac{\partial}{\partial x}F_i(x,y)\right)^2 \\ & + \cancel{\left(\frac{\partial}{\partial y}\phi(x,y)\right)^2} + 2\beta\frac{\partial}{\partial y}F_i(x,y)\frac{\partial}{\partial y}\phi(x,y) + \beta^2\left(\frac{\partial}{\partial y}F_i(x,y)\right)^2 \\ & - \cancel{\left(\frac{\partial}{\partial x}\phi(x,y)\right)^2} - \cancel{\left(\frac{\partial}{\partial y}\phi(x,y)\right)^2} \Bigg] dxdy \\ = \; & \frac{1}{R}\int_R \Bigg[ 2\beta\frac{\partial}{\partial x}F_i(x,y)\frac{\partial}{\partial x}\phi(x,y) + \beta^2\left(\frac{\partial}{\partial x}F_i(x,y)\right)^2 + 2\beta\frac{\partial}{\partial y}F_i(x,y)\frac{\partial}{\partial y}\phi(x,y) \\ & + \beta^2\left(\frac{\partial}{\partial y}F_i(x,y)\right)^2 \Bigg] dxdy \\ = \; & \frac{1}{R}\int_R 2\beta\left[\frac{\partial}{\partial x}F_i(x,y)\frac{\partial}{\partial x}\phi(x,y) + \frac{\partial}{\partial y}F_i(x,y)\frac{\partial}{\partial y}\phi(x,y)\right] dxdy \\ & + \frac{1}{R}\int_R \beta^2\left[\left(\frac{\partial}{\partial x}F_i(x,y)\right)^2 + \left(\frac{\partial}{\partial y}F_i(x,y)\right)^2\right] dxdy, \end{aligned} \tag{5-11}$$

where $SM_i - SM_{init}$ can be simplified into $w_{i,init}$. Now Equation 5-11 can be written in the simplified form [Linhai and Rao, 2011], by substituting Equation 1-12 for $\frac{\partial}{\partial x}\phi(x,y)$:

$$W = 2\beta SV + \beta^2 S_m, \tag{5-12}$$

where

$$S = \begin{bmatrix} S_{1,1} & S_{1,2} & \cdots & S_{1,N} & \cdots & S_{1,M} \\ S_{2,1} & S_{2,2} & & \cdots & \cdots & \cdots \\ \vdots & & \ddots & S_{N-1,N} & \cdots & S_{N-1,M} \\ S_{N,1} & \cdots & S_{N,N-1} & S_{N,N} & \cdots & S_{N,M} \end{bmatrix}, \tag{5-13}$$

$$S_m = \begin{bmatrix} S_{1,1} \\ S_{2,2} \\ \vdots \\ S_{N,N} \end{bmatrix}, W = \begin{bmatrix} w_{1,init} \\ w_{2,init} \\ \vdots \\ w_{N,init} \end{bmatrix}, V = \begin{bmatrix} \nu_1 \\ \nu_2 \\ \vdots \\ \nu_N \\ \vdots \\ \nu_M \end{bmatrix}, \tag{5-14}$$

where $N$ is the number of modes that the Deformable Mirror (DM) can correct for and $M$ is the number of modes with which the incoming wavefront can be described. Usually $M > N$, but in [Lianghua et al., 2017] a method is proposed where $M = N$, making the $S$-matrix squared. The entries of the $S$-matrix can be computed using Equation 4-3. Now the control vector, which contains the coefficients $\nu_i$ that represent the combination of modes that represent the incoming wavefront, can be computed by rearranging the terms in Equation 5-12 into

$$V = \frac{S^{-1}(W - \beta^2 S_m)}{2\beta}. \tag{5-15}$$

It should be taken into account that Equation B-3 is usually used as a metric and that $W$ should be converted from

$$w_{i,init} = SM_i - SM_{init} \approx c_0(1 - MDS_i) - c_0(1 - MDS_{init}) = -c_0(MDS_i - MDS_{init}), \quad (5\text{-}16)$$

into

$$w_{i,init} = -c_0 m_{i,init}, \quad (5\text{-}17)$$

where

$$m_{i,init} = MDSE_i - MDSE_{init}. \quad (5\text{-}18)$$

This resulting in

$$V = \frac{S^{-1}(c_0 M - \beta^2 S_m)}{2\beta}, \quad (5\text{-}19)$$

where

$$M = \begin{bmatrix} m_{1,init} \\ m_{2,init} \\ \vdots \\ m_{N,init} \end{bmatrix}. \quad (5\text{-}20)$$

Now the most optimal control vector can be found after $N+1$-measurements by solving a set of linear equations. However, as stated before, in a dynamic situation the delay between the initial measurement and the $N^{th}$ measurement increases with the number of modes and might become unstable in closed loop form in dynamic situations. In order for this method to work, it is assumed that the incoming aberration does not change between the initial measurement and the $(N+1)^{th}$ measurement. In Figure 5-1, a schematic overview is given of this method.

## 5.3 Frozen Window Assumption

In this section the *Frozen Window Time* will be discussed. As mentioned in section 5.2, all measurements are needed in order to solve the set of linear equations. Therefore, it is required for this method that the incoming wavefront does not change over time. This might hold in static situations, but it does not hold in dynamic situations. In static situations, the incoming wavefront does not change over time and in dynamic situations, the incoming wavefront does change over time.

This is a very important point of interest for this thesis, as the main goal is to design a system for astronomy. In astronomy, there must be dealt with turbulence, which is an example of a situation where dynamic aberrations occur. In order to apply this method, the *Frozen Window Time* must be reduced. In chapter 6, a method is described that reduces the *Frozen Window Time* drastically.

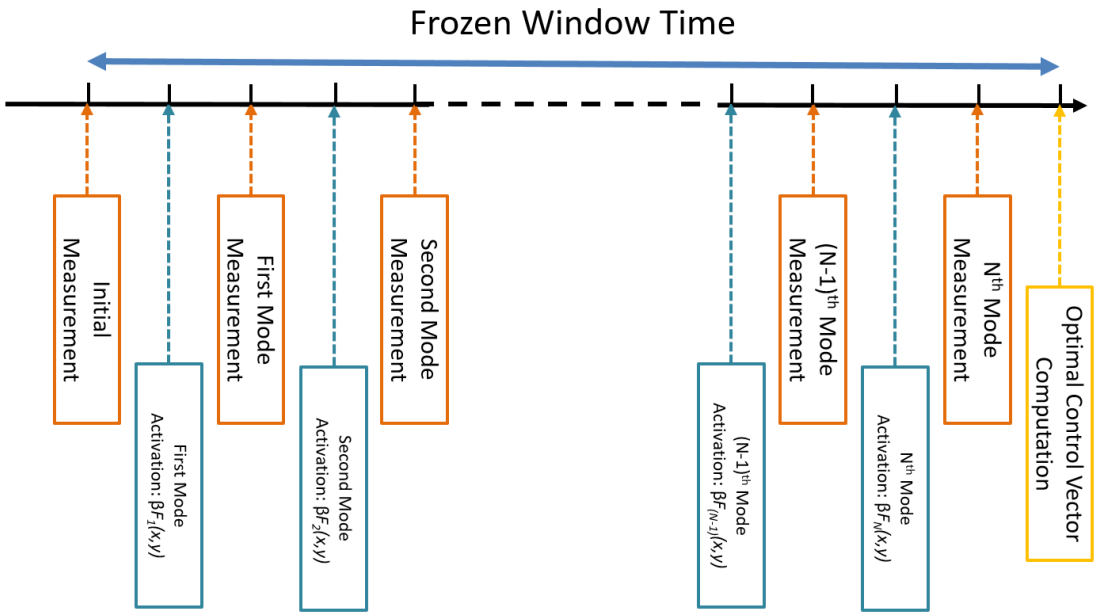


**Figure 5-1:** Schematic overview of General Model Based Approach over time. It should be taken into account that this is only a schematic representation of the process

# Chapter 6

# A Synchronous Model Based Approach

In order to reduce the *Frozen Window Time*, a method proposed by [Lianghua et al., 2017] is evaluated. The main idea of this approach is to decouple the set of modes and use the independent set of modes as a basis to update every modes independently. In order to do this, first a basis must be chosen or computed that is fully orthogonal, i.e. has a diagonal correlation matrix of the gradients of the set of modes. An example of this is the set of Lukosz-Braat polynomials, but for the Deformable Mirror (DM) that will be used in this thesis a new set must be derived, as the LB-polynomials can not be represented well enough. This will be done in section 6.1, followed by the results of this approach in section 6.2. In this section also the extra benefits for the computation time will be discussed and the development of the metric value over time will be compared to the method proposed in section 5.2.

## 6.1 An Independent Set of Modes

In order to decrease this delay, it is proposed in [Lianghua et al., 2017] to increase the total number of measurements to $2N$, and use every uneven measurement as the initial or comparison measurement and every even measurement to excite one mode and find the most optimum solution for that mode. In order to do so, the modes that are to be updated must be fully independent. If they are not, it is not possible to update one single mode, because other modes will influence the resulting Point Spread Function (PSF). As could be seen in Figure 4-2, the set of actuator responses is not an independent set of modes. So the Zernike- or LB-polynomials can be used for example. It first must be checked if the MMDM can represent these polynomials. This is done in section 4.6.

Another way of finding a suitable set of modes for this method is using the actuator responses as a basis and compute an orthogonal set from these responses. In Figure 4-2 it was observed that the actuator responses itself are not an independent set of modes. This implies that there is always some influence on other modes when updating 1 specific mode. In order to decouple the actuator responses or make the modes fully independent, a singular value

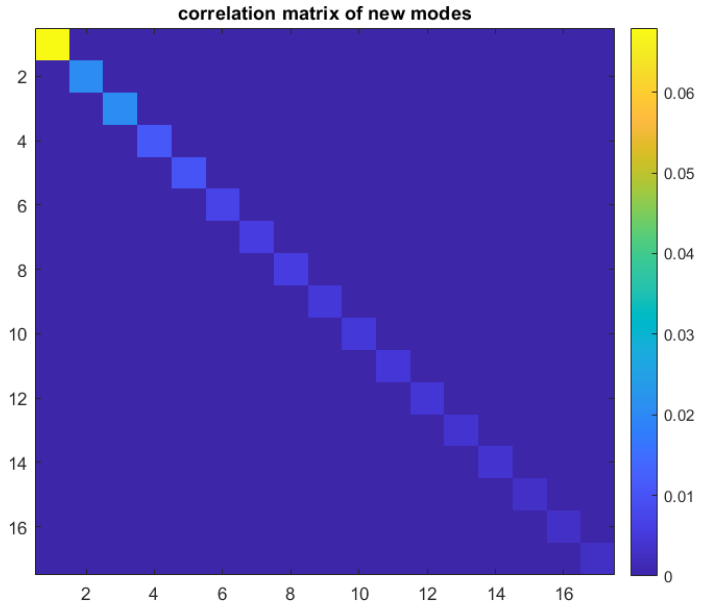


**Figure 6-1:** Correlation matrix of the new independent modes

decomposition of the correlation matrix is computed such that:

$$L = U^{-1}S(V^T)^{-1} \tag{6-1}$$

$L$ will now be a diagonal matrix and $U$ can be used to find the new set of modes corresponding to $L$, $G(x, y)$:

$$G(x, y) = U^{-1}F(x, y), \tag{6-2}$$

where $F(x, y)$ represents the set of actuator responses. Plotting $L$ yields the expected correlation matrix, i.e. a diagonal matrix, see Figure 6-1. In Figure 6-2, the responses of the new modes can be found and it can be seen that they are very different from the original actuator responses.

## 6.2 2N Iteration Solution

Now that an orthogonal basis is found for the DM, a solution for this method can be derived. As the correlation matrix of the new modes is diagonal, the control vector computation can be simplified from a matrix equation into a scalar computation. Starting with:

$$V = \frac{L^{-1}(c_0 M - \beta^2 L_m)}{2\beta} \tag{6-3}$$

This can be simplified, because $L$ is diagonal. This implies that every entry of $V$ can be computed by a scalar computation:

$$\nu_i = \frac{L_{i,i}^{-1}(c_0 m_{i,init} - \beta^2 L_{i,i})}{2\beta}, \tag{6-4}$$

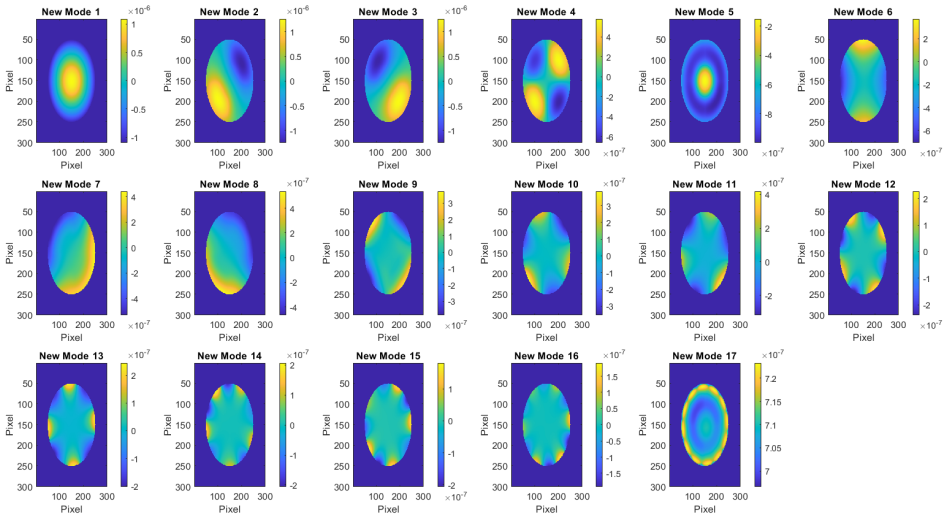


**Figure 6-2:** Responses of the new independent modes in the small aperture of the mirror

This method requires only 2 measurements to update 1 mode and it could be updated in N+1 measurements, but it is now also possible to update every mode separately. This has the advantage that the delay between the initial measurement and the update measurement can be reduced to only 2 measurements. With this, the *Frozen Window Time* decreases significantly and the goal of this method is achieved. However, with this method, also the computation time reduces significantly, as the control vector computation reduces from a matrix equation, to a scalar equation. One important downside of this method is the increase in the time to update all the modes, which increases from $N + 1$ to $2N$. In Figure 6-3, a schematic overview is given of the method proposed by [Lianghua et al., 2017].

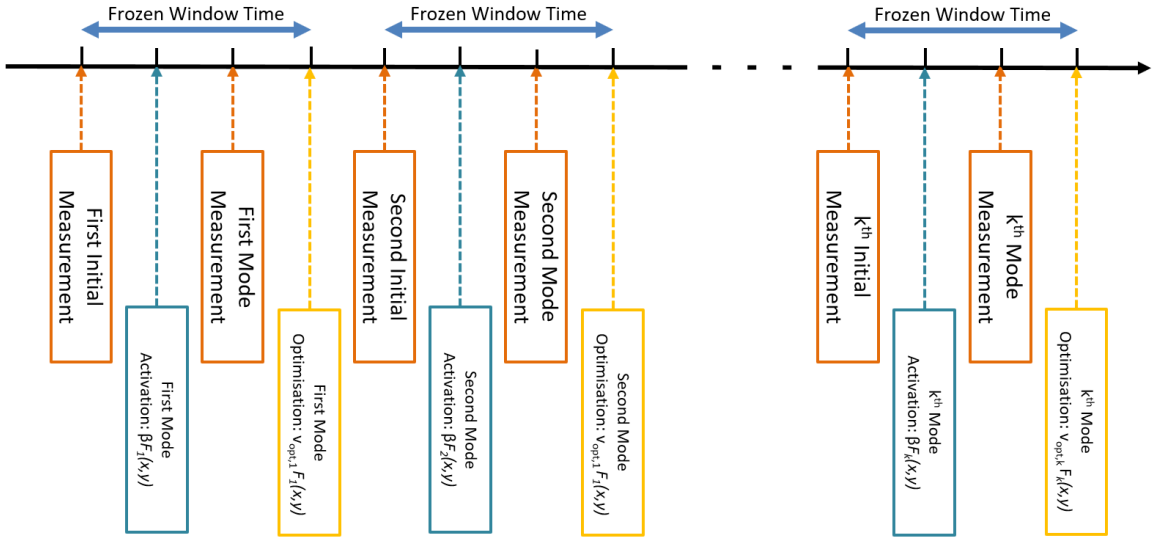


**Figure 6-3:** Schematic overview of the Synchronous Model Based Approach

# Chapter 7

# Mirror Calibration

In this chapter two different calibration techniques will be discussed. The first is based on the research of [Booth, 2011] and [Pozzi et al., 2018] and will be elaborately discussed in this chapter. The techniques from these researches are used as a basis for the new proposed online calibration procedure, which is based on the general model based approach. The SM will be used as a metric value instead of the Sharpness metric [Booth, 2011]. This calibration procedure will be introduced in this chapter, but discussed more extensively in section 9.1.

## 7.1 Emperical Mirror Calibration

Using simulations to verify certain methods is always desirable. It gives insight in the behaviour of a method and might show flaws in advance. However, those simulations are only a reflection of reality and in order to implement the methods into a real experiment, some important steps must be taken. There are some important errors that are not, or can not, be taken into account entirely, such as non-common path errors, alignment errors or errors in the basis set of the actuator responses. In order to overcome these problems, calibration is needed. In this calibration procedure, several different approaches can be taken. The two main different approaches are an online or offline approach. Using an offline approach has the advantage that a Wavefront Sensor (WFS) can be included in the system, which means that the delay introduced by the Deformable Mirror (DM) can be checked thoroughly and that an actual representation of the delay can be mapped. However, the offline calibration procedure does not take into account any misalignment errors if the system is replaced, it can introduce non-common path errors, due to extra optical elements, and it implies that the setup must be changed if one wants to calibrate the DM. Using an online calibration procedure has the advantage that any system induced errors will be taken into account and can be performed any time and also if anything is changed in the system. In [Booth, 2011] an online calibration procedure is proposed, which uses the Sharpness metric as a basis for the calibration. In order to solve this problem, they introduce several different steps. Starting with categorizing the modes, where the used set of modes is the set of Zernike polynomials. Then, the calibration procedure is initialized and at last also a check is done on the correlation matrix.

### 7.1.1 Mode Classification

Because the Sharpness metric is used, first some modes must be excluded from the used set of modes. In order to do this, first the set must be categorized. The used set in [Booth, 2011] is the set of Zernike polynomials, which inhibits some useful characteristics. In order to define the different categories, the effect of a mode on the intensity distribution is evaluated. There are 3 categories:

1. Modes that have no effect on image quality or displacement
2. Modes that have no effect on the resolution but do displace the PSF
3. Modes that have influence on the image quality and resolution

### 7.1.2 Displacement Free Modes

The first category includes only the piston term, the second category includes tip and tilt for a 2 dimensional image and also the defocus term for a 3 dimensional image and the last category includes all the other modes. In general, the piston term is always neglected as it has no effect on the image at all. Due to the used metric, in this approach the displacement modes must be dealt with first. These are modes that only displace the image. In order to get rid of these modes, first it is checked how much tip/tilt is present in every mode [Booth, 2011]. Then, an orthogonal projection is made, which projects the part of every mode that is displacement free.

### 7.1.3 Empirical Calibration

Next, the calibration procedure is started. This is done by applying a sequence of predefined input signals to all the different combinations of two modes. For every combination a number of these input signal are applied and the resulting metric values are stored in a vector. Then, due to the used metric, a 3 dimensional ellipse is formed and the measurements are fitted to the standard formula of an ellipse and the parameters that result from the fit represent the same values as the values in the correlation matrix. Once this new matrix is obtained, a Singular Value Decomposition is applied and used to obtain a new set of independent modes. Then, the empirical calibration is performed again to check if the resulting set of modes is indeed an orthogonal set of modes.

## 7.2 SM-based DM calibration

The method described in section 7.1 uses the Sharpness metric to find the correlation matrix. But it must be noted, that the Model Based Approach and its derivations all use the Second-Moment (SM) as a metric. This means that a different approach is needed, that is based partially on the above described method. In order to implement the SM-based DM calibration, the model based approach is used. In section 9.1, an extensive explanation and derivation of this procedure is presented.

# Chapter 8

# Extended Object

The research up till here has been based on a point source. Especially the metrics that have been derived are based on the assumption that the object image can be represented by a dirac function, which means that the object is neglected in the computations. However, it might be very interesting to look into objects that can not be represented as point sources, i.e. extended objects. In [Yang et al., 2015], an approach is proposed that uses a derivation of three steps to mathematically prove what metric to use for extended objects. First, a metric (the Masked Detector Signal (MDS)) is derived for a point source. Next, the point source is shifted to an arbitrary location and at last this shift is used to find a solution for an extended object.

The derivation for the first step is also given in Appendix A, up till the proportionality between the change in the second moment of the intensity distribution and the Mean Squared Gradient (MSG). Next, the important MDS is introduced. This is based on the practical limitations of the detector radius of the sensor and is defined as Equation B-3. In Appendix B, this relation is derived.

The next step in the derivation is proving that the point source can be located at any point on the sensor. In [Yang et al., 2015] it is proven that it does not matter where the point source is located, but it should be taken into account that an aberration in the form of tip/tilt would be undistinguishable from a point source at a shifted location. So the limitation of this derivation is that in the process, the tip/tilt aberrations should average zero. In Appendix B, the derivation of [Yang et al., 2015] is summarized in order to prove this relation. Once this identity is proven, it can be extended to the application on extended objects as well.

The last step in the derivation of a metric for extended object is combining the shifted point source and the assumption that an extended object can be represented as a combination of all point sources that represent the object image. This assumption is based on the image of an extended object, which can be described by a convolution of the object image and the Point Spread Function (PSF) of the aberration. In Appendix B the full derivation is presented, based on the derivation of [Yang et al., 2015]. The results are that the change in the intensity

distribution is still proportional to the MSG, see Equation B-14, and that the MDS could be used as a metric for an extended object if it is modified

$$\frac{\int_{\mathbb{R}^2}\left(i(\boldsymbol{u})-i_0(\boldsymbol{u})\right)|\boldsymbol{u}|^2\mathrm{d}\boldsymbol{u}}{\int_{\mathbb{R}^2} i(\boldsymbol{u})\mathrm{d}\boldsymbol{u}}=\frac{1}{4\pi^2}\frac{\int_{\mathbb{R}^2}\left(P(x)\varphi'_x(x)\right)^2\mathrm{d}x}{\int_{\mathbb{R}^2}P^2(x)\mathrm{d}x}. \tag{8-1}$$

This expression can be simplified when the Masked Detector Signal for Extended Objects (MDSE) is introduced, which can be computed with [Yang et al., 2015]

$$\mathrm{MDSE}=\frac{\int_{\mathbb{R}^2} i(\boldsymbol{u})\,|\boldsymbol{u}|^2\,\mathrm{d}\boldsymbol{u}}{\int_{\mathbb{R}^2} i(\boldsymbol{u})\mathrm{d}\boldsymbol{u}}, \tag{8-2}$$

which can be used to simplify Equation 8-1 into

$$\mathrm{MDSE}-\mathrm{MDSE}_0=c_0\mathrm{MSG}. \tag{8-3}$$

# Part II

# A Continuous Model Based Approach

# Introduction Continuous Model Based Approach

In the model based approach the most important assumption is the *frozen window time*. It assumes that the incoming wavefront does not change over time, from the initial measurement until the measurement for the last mode. In [Lianghua et al., 2017], a method is proposed that decreases this *frozen window time* significantly by decoupling all the modes. By doing so, it is possible to update every mode independently using only two consecutive measurements, which implies that the *frozen window time* can be decreased to only two measurements. The downside of this method is that the total number of measurements increases, as every mode needs two measurements, resulting in a total of $2N$ measurements. This means that the time between the initial measurement increases significantly and it is highly doubtful if this increases the quality and performance of such a system in dynamic situations. In this thesis a method is proposed which implements the decoupling of the system, while also decreasing the number of measurements from $2N$ to $N + 1$ measurements. This new method is referred to as the Continuous Model Based Approach (CMBA).

In order to implement the CMBA, it is assumed that the incoming wavefront does not change over the time between two measurements. Two measurements are needed to compute of the most optimal control input for one mode. In Figure 9-1 a schematic overview is given of the proposed method. It should be noted that the *frozen windows* overlap. However, it is assumed that every *frozen window* is different, i.e. the incoming wavefront is different for every *frozen window*. This might seem like a contradiction, as this might imply that the first *frozen window* must be the same as the second (as they overlap), and the second must be the same as the third and so on, but for this approach this is not the case. Even though these windows overlap, it is assumed that the wavefront in every window is based on the incoming wavefront at the time instance of the first measurement of the window. This implies that the wavefront is different for every window and that every measurement (except the first) is used twice and for a different computation.

In this part of the thesis, two new approaches will be presented and validated in simulations and experiments. First, the mathematical proof of the CMBA will be presented. To verify the efficiency and validity of the CMBA, simulations and experiments will be conducted and compared with two known methods; the General Model Based Approach (GMBA) and Synchronous Model Based Approach (SMBA). In order to be able to implement this method in the experimental setup, an extra part has been included for the calibration of the DM. The results for the simulations will be presented in chapter 10 and discussed in chapter 11. Lastly, conclusions will be drawn in chapter 12 and the recommendations for further research will be summarised.

# Chapter 9

# Method

In this section two new contributions to the field of Adaptive Optics (AO) are proposed: an online calibration procedure for the experimental implementation and a new method which uses a Wavefront Sensorless Adaptive Optics (WFSless AO) approach and is referred to as the Continuous Model Based Approach (CMBA). The CMBA uses only $N+1$ measurements and can be updated after each iteration. This reduces the number of measurements, compared to the Synchronous Model Based Approach (SMBA) [Lianghua et al., 2017], and it reduces the *frozen window time* significantly to only 2 measurements, compared to the $N+1$ measurements in the General Model Based Approach (GMBA) [Linhai and Rao, 2011].

This section will start with introducing the new online calibration procedure for the acquisition of the correlation matrix. This procedure is needed to overcome system induced errors and can be implemented on any system with a Deformable Mirror (DM) and CCD camera. Followed by explaining the general idea of the CMBA and the problem that arises when every mode is updated after every iteration. Then, a solution is formulated, where the most optimal control input is derived. Followed by the algorithm that solves this problem. In order to validate the online calibration procedure and the CMBA, first simulations are run and than experiments are conducted. The implementation of the simulations and experiments will be discussed in the last part of this section.

## 9.1 Mirror Calibration

Before the new method can be implemented, first the mirror must be calibrated. In order to overcome misalignment errors or non-common path errors, an online calibration method is preferred, as this approach takes these errors into account in its calibration. Implementing an offline calibration might result in a more accurate representation, but after the calibration, the DM must be positioned in the setup, where more errors might be introduced.

In the calibration procedure, there are several steps that need to be taken. First, a basis set must be chosen, such as the actuator responses or a precomputed set of (independent) modes. Then the correlation/crosstalk matrix must be determined and from this new obtained matrix, a singular value decomposition can be computed, which can be used to compute the new set of modes $G(x, y)$, based on the old set $F(x, y)$:

$$G(x, y) = \boldsymbol{B}F(x, y). \tag{9-1}$$

In order to obtain matrix $\boldsymbol{B}$, several different inputs are applied to the DM and the intensity distribution is measured. In the following sections, the different parts of the calibration will be described. Starting with the input computation and the used metric, followed by the calibration method itself, which is based on the model based approach.

### 9.1.1 Input Computation

In order to find the correlation matrix, all different combinations of two different modes are to be excited, resulting in the mirror induced aberration

$$\phi_{DM}(x, y) = \sum_{i=1}^{N} \beta_i F(x, y) \tag{9-2}$$

To excite the system, the same inputs are used as in [Booth, 2011]:

$$\begin{aligned} \beta(i) &= \gamma \cos(\tfrac{2\pi}{T} n) \\ \beta(j) &= \gamma \sin(\tfrac{2\pi}{T} n), \end{aligned} \tag{9-3}$$

for $i \neq j$, $\gamma$ is a scaling term and $T$ is the total number of excitations for every combination of modes. By using this approach, the total excitation will always be equal to $\gamma$.

Another choice for the control input can be to only excite one mode or another combination of modes. Because this approach is based on the research of [Booth, 2011], the above described input is used in this thesis and because it has been shown to work in simulations. It is beyond the scope of this thesis to look into the most optimal control input for this approach, but it is recommended to do so in further research.

### 9.1.2 Metric

As the model based approach implements the SM of the intensity distribution is the optimisation metric, it is also desired to use this metric for the calibration procedure. It should be taken into account that this is a different metric, compared to the research of [Booth, 2011] and [Débarre et al., 2008], where respectively the total intensity and sharpness metric are used. The computation of this metric is explained in section chapter 3 and because it uses the CoG of the intensity distribution as a middle point, it is not necessary to implement the displacement removal procedure.

### 9.1.3 Calibration Procedure

In order to find the correlation matrix, that will be used for the optimisation, a new method will be described that uses the model based approach as a basis. Using the following relation, which is equivalent to Equation 5-12:

$$SM_i - SM_{init} = 2\beta SV + \beta^2 S_m, \tag{9-4}$$

the goal is to solve for $S$. This can be achieved by rewriting the matrices into vectors with

$$SM_i - SM_{init} = 2\text{vec}(\beta V)^T \text{vec}(S) + \text{vec}(\beta^2)^T \cdot \text{vec}(I)^T \text{vec}(S), \tag{9-5}$$

which can be simplified into

$$SM_i - SM_{init} = (2\text{vec}(\beta V)^T + \text{vec}(\beta^2)^T \cdot \text{vec}(I)^T)\text{vec}(S) \tag{9-6}$$

and solved for S as

$$\text{vec}(S) = (2\text{vec}(\beta V)^T + \text{vec}(\beta^2)^T \cdot \text{vec}(I)^T)^{-1}(SM_i - SM_{init}) \tag{9-7}$$

This equation can only be solved if the aberration vector V is known. This can be solved by implementing a simple optimisation algorithm, such as a Stochastic Gradient Descent (SGD) or Coordinate Search (CS) algorithm. Then the resulting coefficient or control vector can be simply filled in in the equation. In the simulations, where there is no system induced error, this can be implemented by assuming a very small and equal error in the initial measurement. It must be taken into account that this error does not directly represent the system induced error. But after the calibration, this applied aberration (the control input used to generate it) does include the system induced aberration. It must also be taken into account that Equation 9-7 can only be used to compute the entries of matrix $S$ that correspond to the two excited modes($S_{i,i}$, $S_{i,j}$, $S_{j,i}$ and $S_{j,j}$). In order to solve for every value of the $S$ matrix, this means that all the combinations must be excited. In Figure 10-1, the resulting correlation matrix can be found. This correlation matrix can then be used to compute the new set of modes, based on the used set of modes, see Figure 10-2.

## 9.2 General Problem Statement

Once the mirror is calibrated, the optimisation of the image quality can be started. This can be done by using a model based approach for example, such as described in chapter 5. However, as mentioned in chapter 6, if the 'general' model based approach is used, the *frozen window time* becomes significantly large. In order to overcome this, a SMBA is proposed by [Lianghua et al., 2017], which decreases the *frozen window time* but increases the total number of measurements. In order to use as few measurements as possible, whilst keeping the *frozen window time* as short as possible, a new method is proposed. This 'new' method will be referred to as the CMBA. In the next sections, the mathematical proof validation for this method will be given. In chapter 10, experimental results for the method will be shown and discussed.

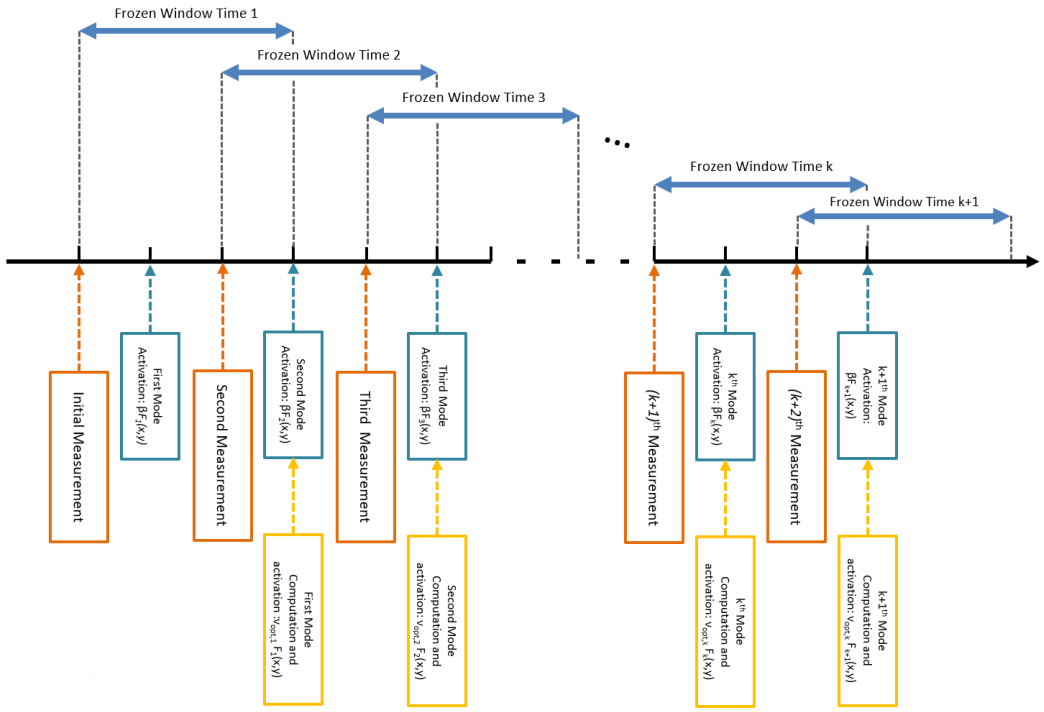


**Figure 9-1:** Schematic overview of the proposed method

## 9.3 Continuous Model Based Approach

In order to overcome the aforementioned problems of the *frozen window time* and the total number of iterations, two steps are combined in the optimisation process (compared to the SMBA). The optimisation of the previous mode will be combined with the addition of a known aberration to the next mode (which is needed to compute the optimal control input for the next mode). In Figure 9-1 a schematic overview of the proposed method is displayed. The combination of the optimisation and excitation is displayed by the yellow and blue boxes. The measurements are visualised in orange. It can be seen that this method uses less measurements but keeps the frozen window time relatively low. In order to find the needed steps in the process, several different steps will be taken, starting with a mathematical description of the situation. Then, a general problem statement will be formulated for this problem, followed by a solution.

### 9.3.1 General Approach

For this method the incoming wavefront is denoted as $\psi_0$ at $t = 0$. The optimal control vector $v$ is not known and is assumed to be equal to a column vector of zeros with length $N$. It is also assumed that the incoming wavefront remains the same for two consecutive measurements and is defined as the wavefront at the time instance of the first measurement. In this section

it will be shown that it is not possible to directly compute the most optimal control input if both the computed optimal control input for a mode and the known aberration for the next mode are applied to the DM. In order to show this, the first 3 updates will be discussed and extended to a more general case. In these cases, it is assumed that the optimal control input can be computed, using the GMBA described in for example [Linhai and Rao, 2011] and in subsection 9.3.2. Then this general result will be used to compute the optimal control input for a certain mode based on the approach of [Linhai and Rao, 2011] and it will be shown that there will be one variable too much for this approach. The next step will introduce a method which projects the most optimal Second-Moment (SM) of the intensity distribution and uses this projection to compute the new optimal control input for the next mode.

**First mode** In order to compute the first mode an initial measurement is taken at $t = 0$ and then a known aberration is added in the form of $\beta F_1(x, y)$. A second measurement is taken at $t = 1$ and the wavefronts at these two time instances can be described by

$$\begin{array}{lll} t = 0 & \phi_0 = & \psi_0 \\ t = 1 & \phi_{1A} = & \psi_0 + \beta F_1(x, y). \end{array} \tag{9-8}$$

With these two measurements the most optimal control input for the first mode, $\gamma_1$ can be computed and filled in the optimal control vector $v_1$.

$$v_1 = v_0 = zeros(N, 1), \tag{9-9}$$

$$v_1(1, 1) = \gamma_1. \tag{9-10}$$

It is assumed that the incoming wavefront has not changed over these two measurements, but in a real-time situation, the incoming wavefront has changed and at time instance $t = 1$, it can be denoted as $\psi_1$. Using this the second mode can be updated.

**Second mode** Now it is assumed that the wavefront at time instance $t = 1$ has changed and can be denoted by $\psi_1$. However, at time instance $t = 1$, a known aberration was added in the form of $\beta F_1(x, y)$ to compute the optimal control input $\gamma_1$. Now this optimal control input can be added in the next step (at time instance $t = 2$), together with the knwon aberration of the second mode. The wavefronts at the time instances $t = 1, 2$ can be described by

$$\begin{array}{lll} t = 1 & \phi_{1B} = & \psi_1 + \beta F_1(x, y) \\ t = 2 & \phi_{2A} = & \psi_1 + \sum_{i=1}^{\infty} v_{1,i} F_i(x, y) + \beta F_2(x, y). \end{array} \tag{9-11}$$

With the measurements at these two time instances, the most optimal control input $\gamma_2$ can be computed for the second mode and the optimal control vector updates to $v_2$:

$$v_2 = v_1 \tag{9-12}$$

$$v_2(2, 1) = \gamma_2 \tag{9-13}$$

**Third mode** Again, it is assumed that the wavefront at time instance $t = 2$ has changed and can be denoted by $\psi_2$. However, at time instance $t = 2$, a known aberration was added in the form of $\beta F_2(x, y)$ to compute the optimal control input $\gamma_2$. Now this optimal control input

can be added in the next step (at time instance $t = 3$), together with the knwon aberration of the second mode. The wavefronts at the time instances $t = 2, 3$ can be described by

$$\begin{array}{lll} t=2 & \phi_{1B} = & \psi_2 + \sum_{i=1}^{\infty} v_{1,i} F_i(x,y) + \beta F_2(x,y) \\ t=3 & \phi_{2A} = & \psi_2 + \sum_{i=1}^{\infty} v_{2,i} F_i(x,y) + \beta F_3(x,y). \end{array} \tag{9-14}$$

With the measurements at these two time instances, the most optimal control input $\gamma_3$ can be computed for the second mode and the optimal control vector updates to $v_3$:

$$v_3 = v_2 \tag{9-15}$$

$$v_3(3,1) = \gamma_3 \tag{9-16}$$

***$k^{th}$* mode** For a more general approach, the $k^{th}$ mode is used. Following the same approach as for the first two modes, the wavefronts at time instances $t = k, k+1$ can be described by

$$t = k \qquad \phi_{kB} = \psi_k + \sum_{i=1}^{\infty} v_{k-1,i} F_i(x,y) + \beta F_k(x,y), \tag{9-17}$$

$$t = k+1 \qquad \phi_{(k+1)A} = \psi_k + \sum_{i=1}^{\infty} v_{k,i} F_i(x,y) + \beta F_{k+1}(x,y). \tag{9-18}$$

With the measurements at these two time instances, the most optimal control input $\gamma_k$ can be computed for the second mode and the optimal control vector updates to $v_k$:

$$v_k = v_{k-1} \tag{9-19}$$

$$v_k(k,1) = \gamma_k \tag{9-20}$$

These representation can be used in the approach to compute the optimal control input. As stated earlier, in the above cases, it is assumed that it is possible that the optimal control input can be computed. In the following section, it will be shown that this is not necessarily true.

### 9.3.2 Optimal control input computation

In this section the following notations will be used for the derivatives w.r.t. the x- and y-direction, where it is assumed that the incoming wavefront can be described by a linear combination of a certain set of modes $F(x, y)$:

$$\frac{\partial}{\partial x}\psi_k = \sum_{i=1}^{\infty} v_i \frac{\partial}{\partial x} F_i(x,y) = \boldsymbol{v}\frac{\partial}{\partial x}\sum_{i=1}^{\infty} F_i(x,y) = \boldsymbol{v}\sum_{i=1}^{\infty}\frac{\partial}{\partial x}F_i(x,y) \tag{9-21}$$

$$\frac{\partial}{\partial y}\psi_k = \sum_{i=1}^{\infty} v_i \frac{\partial}{\partial x} F_i(x,y) = \boldsymbol{v}\frac{\partial}{\partial y}\sum_{i=1}^{\infty} F_i(x,y) = \boldsymbol{v}\sum_{i=1}^{\infty}\frac{\partial}{\partial y}F_i(x,y) \tag{9-22}$$

It is also assumed that the used set of modes exhibits orthogonal behaviour in the gradients of the set. Now the proportionality between the Mean Squared Gradient (MSG) and the change in the SM of the intensity distribution is used:

$$\iint_{\mathbb{R}^2} \underbrace{\left(\phi'_{kB}\right)^2}_{①} - \underbrace{\left(\phi'_{(k+1)A}\right)^2}_{②} = SM_{kB} - SM_{(k+1)A}, \tag{9-23}$$

where

$$\textcircled{1} \quad \left(\phi'_{kB}\right)^2 = \underbrace{\left(\frac{\partial}{\partial x}\phi_{kB}\right)^2}_{\textcircled{A}} + \underbrace{\left(\frac{\partial}{\partial y}\phi_{kB}\right)^2}_{\textcircled{B}}. \tag{9-24}$$

Now Equation 9-18 can be substituted in (A) and (B), which yields

$$\textcircled{A} \quad \left(\frac{\partial}{\partial x}\phi_{kB}\right)^2 = \left(\frac{\partial}{\partial x}\psi_k + \sum_{i=1}^{\infty} v_{k-1,i}\frac{\partial}{\partial x}F_i(x,y) + \beta\frac{\partial}{\partial x}F_k(x,y)\right)^2, \tag{9-25}$$

$$\textcircled{B} \quad \left(\frac{\partial}{\partial y}\phi_{kB}\right)^2 = \left(\frac{\partial}{\partial y}\psi_k + \sum_{i=1}^{\infty} v_{k-1,i}\frac{\partial}{\partial y}F_i(x,y) + \beta\frac{\partial}{\partial y}F_k(x,y)\right)^2, \tag{9-26}$$

where the value for $\beta$ can be rewritten as a column vector as

$$\boldsymbol{\beta_{upd,k+1}}(1:N) = \begin{bmatrix} 0 \\ 0 \\ \vdots \\ 0 \\ 0 \end{bmatrix}, \tag{9-27}$$

with $\boldsymbol{\beta_{upd,k+1}}(k+1) = \beta$, where $k+1$ represents the value of the next mode that is updated. Using

$$\boldsymbol{v}_{upd,k} = \boldsymbol{v}_k + \boldsymbol{\beta}_{upd,k+1}, \tag{9-28}$$

Equation 9-25 can be written as

$$\textcircled{A} \quad \left(\frac{\partial}{\partial x}\psi_k + \frac{\partial}{\partial x}\sum_{i=1}^{\infty} v_{upd,k,i}F_i(x,y)\right)^2 = \left(\frac{\partial}{\partial x}\psi_k\right)^2 + 2\left(\frac{\partial}{\partial x}\psi_k\sum_{i=1}^{\infty} v_{upd,k-1,i}\frac{\partial}{\partial x}F_i(x,y)\right) + \left(\sum_{i=1}^{\infty} v_{upd,k-1,i}\frac{\partial}{\partial x}F_i(x,y)\right)^2, \tag{9-29}$$

Equation 9-26 then becomes

$$\textcircled{B} \quad \left(\frac{\partial}{\partial y}\psi_k + \frac{\partial}{\partial y}\sum_{i=1}^{\infty} v_{upd,k,i}F_i(x,y)\right)^2 = \left(\frac{\partial}{\partial y}\psi_k\right)^2 + 2\left(\frac{\partial}{\partial y}\psi_k\sum_{i=1}^{\infty} v_{upd,k-1,i}\frac{\partial}{\partial y}F_i(x,y)\right) + \left(\sum_{i=1}^{\infty} v_{upd,k-1,i}\frac{\partial}{\partial y}F_i(x,y)\right)^2. \tag{9-30}$$

Using the same approach for (2) yields

$$\textcircled{2} \quad \left(\phi'_{(k+1)A}\right)^2 = \underbrace{\left(\frac{\partial}{\partial x}\phi_{(k+1)A}\right)^2}_{\textcircled{C}} + \underbrace{\left(\frac{\partial}{\partial y}\phi_{(k+1)A}\right)^2}_{\textcircled{D}}. \tag{9-31}$$

For (C) and (D), using that the value for $\beta$ can be rewritten as a column vector as

$$\boldsymbol{\beta_{upd,k}}(1:N) = \begin{bmatrix} 0 \\ 0 \\ \vdots \\ 0 \\ 0 \end{bmatrix}, \tag{9-32}$$

with $\boldsymbol{\beta_{upd,k}}(k) = \beta$, where $k$ represents the value of the mode that is updated in this iteration. Now $\boldsymbol{v}_{upd,k-1}$ can be written as

$$\boldsymbol{v}_{upd,k-1} = \boldsymbol{v}_{k-1} + \boldsymbol{\beta}_{upd,k}, \tag{9-33}$$

which yields the equations for (C) and (D):

$$\text{(C)} \quad \left(\frac{\partial}{\partial x}\phi_{(k+1)A}\right)^2 = \left(\frac{\partial}{\partial x}\psi_k\right)^2 + 2\left(\frac{\partial}{\partial x}\psi_k \sum_{i=1}^{\infty} v_{upd,k,i}\frac{\partial}{\partial x}F_i(x,y)\right) + \left(\boldsymbol{v}_{upd,k}\sum_{i=1}^{\infty}\frac{\partial}{\partial x}F_i(x,y)\right)^2, \tag{9-34}$$

$$\text{(D)} \quad \left(\frac{\partial}{\partial y}\phi_{(k+1)A}\right)^2 = \left(\frac{\partial}{\partial y}\psi_k\right)^2 + 2\left(\frac{\partial}{\partial y}\psi_k \boldsymbol{v}_{upd,k}\sum_{i=1}^{\infty}\frac{\partial}{\partial y}F_i(x,y)\right) + \left(\sum_{i=1}^{\infty} v_{upd,k,i}\frac{\partial}{\partial y}F_i(x,y)\right)^2. \tag{9-35}$$

Now (1) − (2) can be solved, which yields:

$$
\begin{aligned}
(1)-(2) = \;& (A)+(B)-\big((C)+(D)\big) = (A)-(C)+(B)-(D)\\
=\;& \left(\frac{\partial}{\partial x}\psi_k\right)^2 + 2\left(\frac{\partial}{\partial x}\psi_k \sum_{i=1}^{\infty} v_{upd,k-1,i}\frac{\partial}{\partial x}F_i(x,y)\right) + \left(\sum_{i=1}^{\infty} v_{upd,k-1,i}\frac{\partial}{\partial x}F_i(x,y)\right)^2 - \left(\frac{\partial}{\partial x}\psi_k\right)^2\\
&- 2\left(\frac{\partial}{\partial x}\psi_k \sum_{i=1}^{\infty} v_{upd,k,i}\frac{\partial}{\partial x}F_i(x,y)\right) - \left(\sum_{i=1}^{\infty} v_{upd,k,i}\frac{\partial}{\partial x}F_i(x,y)\right)^2\\
&+ \left(\frac{\partial}{\partial y}\psi_k\right)^2 + 2\left(\frac{\partial}{\partial y}\psi_k \sum_{i=1}^{\infty} v_{upd,k-1,i}\frac{\partial}{\partial y}F_i(x,y)\right) + \left(\sum_{i=1}^{\infty} v_{upd,k-1,i}\frac{\partial}{\partial y}F_i(x,y)\right)^2 - \left(\frac{\partial}{\partial y}\psi_k\right)^2\\
&- 2\left(\frac{\partial}{\partial y}\psi_k \sum_{i=1}^{\infty} v_{upd,k,i}\frac{\partial}{\partial y}F_i(x,y)\right) - \left(\sum_{i=1}^{\infty} v_{upd,k,i}\frac{\partial}{\partial y}F_i(x,y)\right)^2\\
=\;& 2\left(\frac{\partial}{\partial x}\psi_k \sum_{i=1}^{\infty} v_{upd,k-1,i}\frac{\partial}{\partial x}F_i(x,y)\right) - 2\left(\frac{\partial}{\partial x}\psi_k \sum_{i=1}^{\infty} v_{upd,k,i}\frac{\partial}{\partial x}F_i(x,y)\right)\\
&+ \left(v_{upd,k-1,i}^2 - v_{upd,k,i}^2\right)\left(\sum_{i=1}^{\infty}\frac{\partial}{\partial x}F_i(x,y)\right)^2\\
&+ 2\left(\frac{\partial}{\partial y}\psi_k \sum_{i=1}^{\infty} v_{upd,k-1,i}\frac{\partial}{\partial y}F_i(x,y)\right) - 2\left(\frac{\partial}{\partial y}\psi_k \sum_{i=1}^{\infty} v_{upd,k,i}\frac{\partial}{\partial y}F_i(x,y)\right)\\
&+ \left(v_{upd,k-1,i}^2 - v_{upd,k,i}^2\right)\left(\sum_{i=1}^{\infty}\frac{\partial}{\partial y}F_i(x,y)\right)^2\\
=\;& 2\frac{\partial}{\partial x}\psi_k \sum_{i=1}^{\infty}\left(v_{upd,k-1,i} - v_{upd,k,i}\right)\frac{\partial}{\partial x}F_i(x,y) + \left(\sum_{i=1}^{\infty}\left(v_{upd,k-1,i}^2 - v_{upd,k,i}^2\right)\frac{\partial}{\partial x}F_i^2(x,y)\right)\\
&+ 2\frac{\partial}{\partial y}\psi_k \sum_{i=1}^{\infty}\left(v_{upd,k-1,i} - v_{upd,k,i}\right)\frac{\partial}{\partial y}F_i(x,y) + \left(\sum_{i=1}^{\infty}\left(v_{upd,k-1,i}^2 - v_{upd,k,i}^2\right)\frac{\partial}{\partial y}F_i^2(x,y)\right).
\end{aligned}
$$

Now Equation 9-21 and Equation 9-22 can be substituted as a representation for the incoming wavefront, which yields

$$
\begin{aligned}
SM_{kB} - SM_{(k+1)A} = \iint_{\mathbb{R}^2} \;& 2\sum_{j=1}^{\infty} v_j \frac{\partial}{\partial x}F_j(x,y)\sum_{i=1}^{\infty}\left(v_{upd,k-1,i} - v_{upd,k,i}\right)\frac{\partial}{\partial x}F_i(x,y)\\
&+ \left(\sum_{i=1}^{\infty}\left(v_{upd,k-1,i}^2 - v_{upd,k,i}^2\right)\frac{\partial}{\partial x}F_i^2(x,y)\right)\\
&+ 2\sum_{j=1}^{\infty} v_j \frac{\partial}{\partial y}F_j(x,y)\sum_{i=1}^{\infty}\left(v_{upd,k-1,i} - v_{upd,k,i}\right)\frac{\partial}{\partial y}F_i(x,y)\\
&+ \left(\sum_{i=1}^{\infty}\left(v_{upd,k-1,i}^2 - v_{upd,k,i}^2\right)\frac{\partial}{\partial y}F_i^2(x,y)\right)\mathrm{d}x\mathrm{d}y,
\end{aligned}
$$

which can be written in a simplified matrix form as

$$
SM_{(k+1)A} - SM_{kB} = 2(\boldsymbol{v}_{upd,k-1} - \boldsymbol{v}_{upd,k})\boldsymbol{SV} + (\boldsymbol{v}_{upd,k-1}^2 - \boldsymbol{v}_{upd,k}^2)\boldsymbol{S}_m, \tag{9-36}
$$

where

$$\boldsymbol{S} = \begin{bmatrix} S_{1,1} & S_{1,2} & \cdots & S_{1,N} & \cdots & S_{1,M} \\ S_{2,1} & S_{2,2} & & \cdots & \cdots & \cdots \\ \vdots & & \ddots & S_{N-1,N} & \cdots & S_{N-1,M} \\ S_{N,1} & \cdots & S_{N,N-1} & S_{N,N} & \cdots & S_{N,M} \end{bmatrix}, \tag{9-37}$$

$$\boldsymbol{S}_m = \begin{bmatrix} S_{1,1} \\ S_{2,2} \\ \vdots \\ S_{N,N} \end{bmatrix}, \boldsymbol{V} = \begin{bmatrix} \nu_1 \\ \nu_2 \\ \vdots \\ \nu_N \\ \vdots \\ \nu_M \end{bmatrix}, \tag{9-38}$$

where

$$S_{i,j} = \frac{1}{R} \iint_R \left[ \frac{\partial}{\partial x} F_i(x,y) \frac{\partial}{\partial x} F_j(x,y) + \frac{\partial}{\partial y} F_i(x,y) \frac{\partial}{\partial y} F_j(x,y) \right] dxdy. \tag{9-39}$$

Using the approach of [Lianghua et al., 2017], the modes can be decoupled and the resulting $S$-matrix becomes diagonal. This implies that Equation 9-36 boils down to a multiplication of scalar values. This will be used later in the next step. The update vectors $\boldsymbol{v}_{upd,k}$ and $\boldsymbol{v}_{upd,k-1}$ are defined as

$$\begin{aligned} \boldsymbol{v}_{upd,k} &= \boldsymbol{v}_k + \boldsymbol{\beta}_{upd,k+1} \\ &= \boldsymbol{v}_{k-1}(:) - v_{k-1}(k) + \gamma_k + \boldsymbol{\beta}_{updt,k+1} \qquad (9\text{-}40) \\ \boldsymbol{v}_{upd,k-1} &= \boldsymbol{v}_{k-1} + \boldsymbol{\beta}_{updt,k}, \qquad (9\text{-}41) \end{aligned}$$

where $v_{k-1}(k)$ represents the $k^{th}$ value of the column vector $\boldsymbol{v}_{,k-1}$ and is only subtracted from the $k^{th}$ entry of this vector. $\gamma_k$ is also just a scalar value and only added to the $k^{th}$ entry of the column vector. Now the two vectors $\boldsymbol{v}_{upd,k}$ and $\boldsymbol{v}_{upd,k-1}$ can be subtracted as

$$\begin{aligned} \boldsymbol{v}_{upd,k-1} - \boldsymbol{v}_{upd,k} &= \boldsymbol{v}_{k-1} + \boldsymbol{\beta}_{updt,k} - (\boldsymbol{v}_{k-1}(:) - v_{k-1}(k) + \gamma_k + \boldsymbol{\beta}_{updt,k+1}) \\ &= v_{k-1}(k) - \gamma_k - \boldsymbol{\beta}_{updt,k+1} + \boldsymbol{\beta}_{updt,k} \\ &= \begin{bmatrix} 0 \\ \vdots \\ +v_{k-1}(k) - \gamma_k + \boldsymbol{\beta}_{updt,k} \\ -\beta_{updt,k+1} \\ \vdots \\ 0 \end{bmatrix} \qquad (9\text{-}42) \end{aligned}$$

and

$$\begin{aligned} \boldsymbol{v}^2_{upd,k-1} - \boldsymbol{v}^2_{upd,k} &= (\boldsymbol{v}_{k-1} + \boldsymbol{\beta}_{updt,k})^2 - (\boldsymbol{v}_{k-1}(:) - v_{k-1}(k) + \gamma_k + \boldsymbol{\beta}_{updt,k+1})^2 \\ &= \begin{bmatrix} 0 \\ \vdots \\ (v_{k-1}(k) + \boldsymbol{\beta}_{updt,k})^2 - \gamma_k^2 \\ -(\beta_{updt,k+1})^2 \\ \vdots \\ 0 \end{bmatrix}. \qquad (9\text{-}43) \end{aligned}$$

In Equation 9-42, it can be seen that this method yields two equations and can be written as:

$$\Delta SM_{k,k+1} = 2\Gamma^T \boldsymbol{S}\boldsymbol{v} + \Lambda^T \boldsymbol{S}_m, \tag{9-44}$$

where

$$\Gamma = \begin{bmatrix} +v_{k-1}(k) - \gamma_k + \boldsymbol{\beta}_{updt,k} \\ -\beta_{updt,k+1} \end{bmatrix} \quad \text{and} \quad \Lambda = \begin{bmatrix} (v_{k-1}(k) + \boldsymbol{\beta}_{updt,k})^2 - \gamma_k^2 \\ -(\beta_{updt,k+1})^2 \end{bmatrix}, \tag{9-45}$$

$$\Delta SM_{k,k-1} = SM_k - SM_{k-1}. \tag{9-46}$$

### 9.3.3 General Problem Statement

Equation 9-44 is to be solved for $\boldsymbol{v}$, but that would not be correct, as the measurement $SM_k$ is taken with a certain aberration added to it. Measuring it again after optimisation, would yield a different value for the $SM_k$. The problem is that there are now two aberrations added in one step; the known aberration of the next mode and the optimal control input of this mode. Thus, the change in the SM of the intensity distribution is dependent on these two changes and it must first be determined, what part of this change is dependent on the optimisation of this mode and what part is dependent on the (known) aberration of the next mode. One option would be to retake the measurement after the optimisation and before the introduction of the next aberration, but that introduces a delay, which is unwanted. Instead of retaking the image one can also reverse engineer the optimal SM for one mode. This SM can be seen as the lowest available SM for a certain mode, which can be achieved if the optimal control input is used as an input. Then this optimised SM can be used to compute the next optimal control input and is denoted as $SM_k^*$. This method uses two steps, first the initialisation and then the optimisation.

### 9.3.4 Computation of optimal SM and control input

In order to compute the optimal SM of the intensity distribution, first the optimal control input $\gamma_k$ must be computed. This can be done by a method described in many researches and is computed as:

$$\gamma_k = \frac{1}{2}\beta_{upd,k}^{-1} \boldsymbol{S}^{-1} \left( \Delta SM_{k-1,k} - \beta_{upd,k}^2 \boldsymbol{S}_m \right), \tag{9-47}$$

where $\beta_{upd,k}$ also includes the previous control input and actually equals (for continuity purposes)

$$\beta_{upd,k} = -2v_k\beta + \beta^2, \tag{9-48}$$

if the previous control input is not equal to zero. If both the SM's of the intensity distributions are known, before the known aberration $\beta_{upd,k}$ is applied and after. If the applied aberration is the only new aberration, this equation can be used to compute the most optimal control input, i.e. the control input that describes the incoming wavefront in the best possible way and can thus be used as the most optimal control input for the DM. However, it should also be taken into account that this formula only solves this problem if solely the known aberration $\beta_{upd,k}$ is applied. But, in order to reduce the number of measurements, also the optimal control input of the previous mode is applied. This can be solved by separating the

total change in the SM of the intensity distribution. This change is dependent on the two changes (optimisation and excitation) and it can be separated, because an independent set of modes is used. The next step is to compute the projection of the SM of the intensity distribution if the optimal control input would have been applied. This is done by computing the SM of the optimised mode using the last measurement. First, the change in SM (between the optimised previous SM and after the excitation with $\beta$):

$$SM^*_{k-1} - SM_k = 2\beta \boldsymbol{S}\gamma_k + (-2v_k\beta + \beta^2)\boldsymbol{S}_m, \tag{9-49}$$

where $SM^*_k$ denotes the SM if the optimal control input ($\gamma_k$) is applied and it is the only unknown in this equation. Now, the projection can be computed with the knowledge that not $\beta$ is applied, but $(v_k - \gamma_k)$. This yields

$$SM^*_{k-1} - SM^*_k = 2\left(v_k - \gamma_k\right)\boldsymbol{S}\gamma_k + ((-2v_k(v_k - \gamma_k) + (v_k - \gamma_k)^2))\boldsymbol{S}_m, \tag{9-50}$$

which can be simplified into

$$SM^*_{k-1} - SM^*_k = -(\gamma_k - v_k)^2\boldsymbol{S}(k,k). \tag{9-51}$$

From this equation, $SM^*_k$ can be easily computed. This optimised SM can be used to compute the optimal control vector for the next mode with Equation 9-47. For the simulations, the Masked Detector Signal (MDS) is used due to the capability of extending its use to extended objects, see section 5.1. This metric is related to the SM of the intensity distribution with Equation 5-17. It must be noted that a maximum metric value of 1 can be achieved for the measurements, due to the computation of the MDS. However, it might occur, due to error build-up in the computations, that the optimal MDS reaches a value above 1. If this happens, this optimisation run is classified as failed and is not taken into account for the comparison. The succes rates of the different simulations can be found in Table 10-1.

## 9.4 Simulations

To validate the new method, it will be compared to the GMBA and the SMBA in simulations first. After the empirical calibration procedure, these three optimisation methods will be run and tested with different levels of noise and different (random) initial aberrations of different magnitudes. The used levels of noise and maximum amplitudes of the initial aberrations can be found in Table 9-1. Every optimisation method is run 500 times for every combination of the noise level and aberration magnitude to get an overview of the resulting values for the Root Mean Squared Error (RMSE) of the residual wavefront and the MDS of the resulting intensity distribution. The results can be found in subsection 10.1.1 and subsection 10.1.2.

| Variable | Value | | | | |
|---|---|---|---|---|---|
| SNR | 0.01 | 0.1 | 0.5 | 1 | 5 |
| Aberration Magnitude | 5 [rad] | 15 [rad] | 30 [rad] | 50 [rad] | |

**Table 9-1:** Overview of the different levels of noise and initial aberration magnitudes

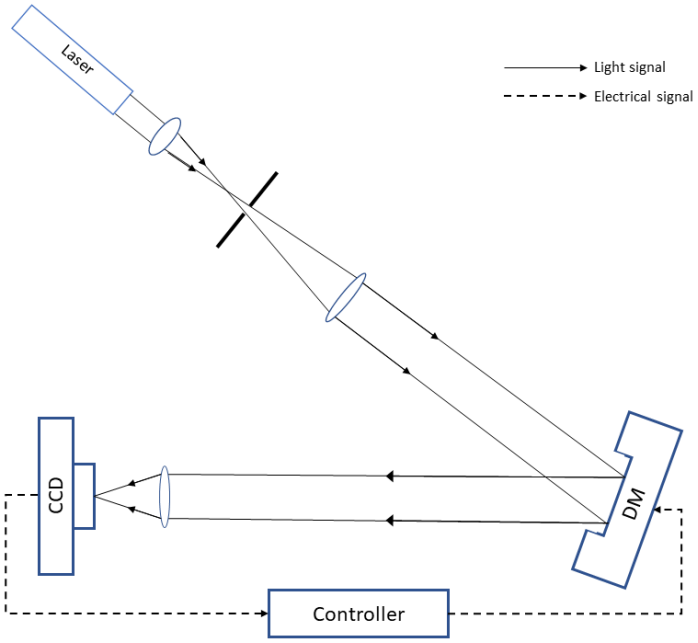


**Figure 9-2:** Schematic overview of Setup used for the Experiments

## 9.5 Experiment

In order to verify the new method, experiments are conducted as well. The results are compared with methods that have been verified in earlier papers, such as the GMBA and the SMBA. An aberration disk is used for the generation of different random aberrations.

### 9.5.1 Layout of the Setup

In Figure 9-2, a schematic representation of the experimental setup is shown. In order to overcome any alignment or focussing errors, an empirical calibration will be performed, as described in section 9.1. The mirror that is used will be the 17 actuator MMDM with Tip/Tilt, see section 2.2 for the specifications. The CCD-camera is the camera discussed in section 2.4.

### 9.5.2 Turbulence Generation

In order to generate random aberrations, approximately corresponding to the Kolmogorov turbulence model, a disk is used with added aberrations. For the aberrations, hairspray is used, which generates bubbles of different sizes and can be used for the aberration generation. This disk is turned after each optimisation and different aberrations are generated.

### 9.5.3 Noise

Due to the camera output, which is an integer in the range of 0-255, the (low-level) noise starts to play a significant role in the experiments. It was seen that the Center of Gravity of the intensity distribution was influenced by the Poissonian shot noise significantly and in order to get more reliable results, a threshold was implemented to get rid of the lower value inputs of the camera. This threshold ensures that the Center of Gravity is less effected by the noise and with visual inspection, the height of the threshold was determined.

### 9.5.4 Experimental setup

A total of 4 runs, each consisting of 50 tests, are conducted. Before the optimisation processes are executed, first the online empirical procedure is run. This procedure is repeated in the beginning of every test with the same parameters to be able to compare the results. To judge the efficiency of every method, also a simple coordinate search algorithm is used to compute the optimal control input and the corresponding 'optimal' metric values.

After the online empirical calibration procedure, the proportionality parameter $c_0$ is tuned manually. This is the parameter that weights the difference in the metric value. This is done for the all the optimisation processes first, after which an aberration is added to the system and the optimisation algorithms are run to correct for the aberration.

The metric values after the optimisation processes are computed for every method and will be used to compare the efficiency of every approach. Also the metric value of the initial aberration is computed and improvement percentages are computed, based on the mean initial and optimised metric values. As a ground truth, also a CS-algorithm is run and the resulting metric value is used as the highest achievable metric value.

# Chapter 10

# Results

In this chapter, the results from the simulations and experiments will be displayed. First, the results of the simulations will be visualised. Then, the results of the experimental implementation will be presented. For the simulations, the Root Mean Squared Error (RMSE) of the residual wavefront and the Masked Detector Signal (MDS) will be used to compare the efficiency and reliability of the three different approaches. For the experiments, the RMSE of the residual wavefront is not available and only the MDS will be used for comparison.

## 10.1 Simulations

To verify the different approaches and check the validity of the new approach, first simulations are performed. These simulations include the empirical calibration, the General Model Based Approach (GMBA), the Synchronous Model Based Approach (SMBA) and the Continuous Model Based Approach (CMBA). All the model based approaches use the empirical calibration procedure and are later compared for the RMSE of the residual wavefront and the MDS. In section 9.4, the inputs for the simulations are introduced.

### 10.1.1 Empirical Calibration

To check the validity of the proposed calibration method, first a set of simulations is performed. The result of the empirical calibration procedure can be seen in Figure 10-1. To check if this matrix can be used for the optimisation, it is implemented in the optimisation methods and the results can be seen in subsection 10.1.2. The resulting correlation matrix can be compared to the numerically obtained correlation matrix, see Figure 4-2 and the resulting set of modes that results from a singular value decomposition can be seen in Figure 10-2.

### 10.1.2 Optimisation of Image Quality

After the empirical calibration procedure has finished, the optimisation process can start. In this section the results for the simulations of the three different approaches will be visualised.

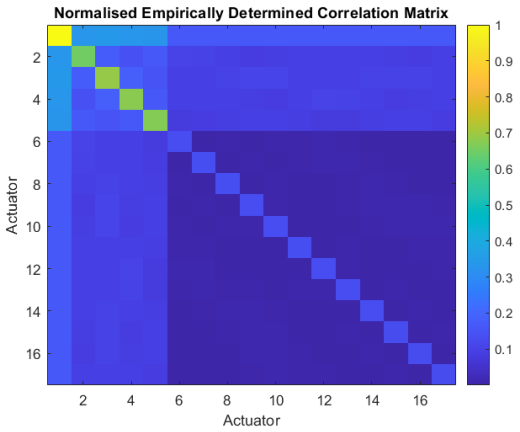


**Figure 10-1:** Empirically Determined Correlation Matrix from Simulations, for 17 actuator MMDM.

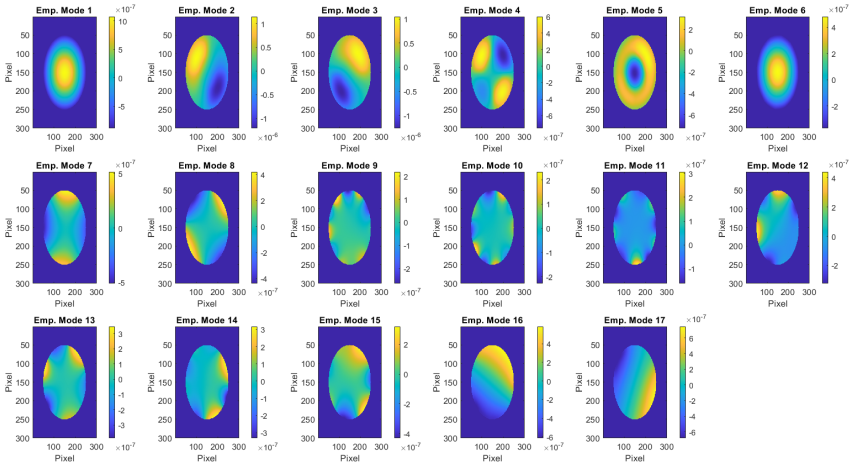


**Figure 10-2:** New set of modes, based on the empirically determined correlation catrix

Starting with the GMBA, followed by the SMBA and finally also the CMBA.

### 10.1.2-i General Model Based Approach

In this section the simulation results of the GMBA will be displayed. In Figure 10-3 and Figure 10-4 respectively the mean initial metric and RMSE values are plotted in pink and the resulting metric values and RMSE values, after the optimisation, are plotted in the boxplots, for different levels of noise and magnitudes of the aberrations. The results of these boxplots will be used for the comparison of the different methods. The boxplots also visualise the trends in the results due to the varying Signal to Noise Ratio (SNR) and aberration magnitude. These trends will also be discussed in the discussion.

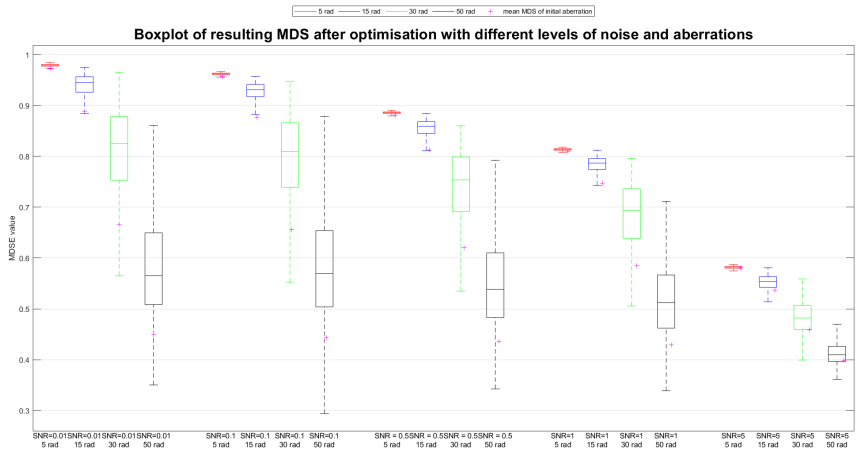


**Figure 10-3:** Results for the residual MDS for the simulations of the GMBA.

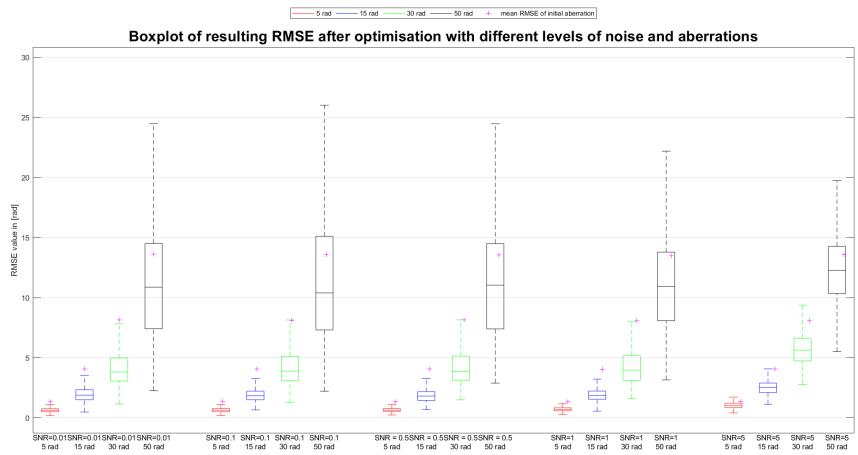


**Figure 10-4:** Results for the residual RMSE for the simulations of the GMBA.

### 10.1.2-ii Synchronous Model Based Approach

In this section the simulation results of the SMBA will be displayed. In Figure 10-5 and Figure 10-6 respectively the mean initial metric and RMSE values are plotted in pink and the resulting metric values and RMSE values, after the optimisation, are plotted in the boxplots, for different levels of noise and magnitudes of the aberrations. The results of these boxplots will be used for the comparison of the different methods. The boxplots also visualise the trends in the results due to the varying SNR and aberration magnitude. These trends will also be discussed in the discussion.

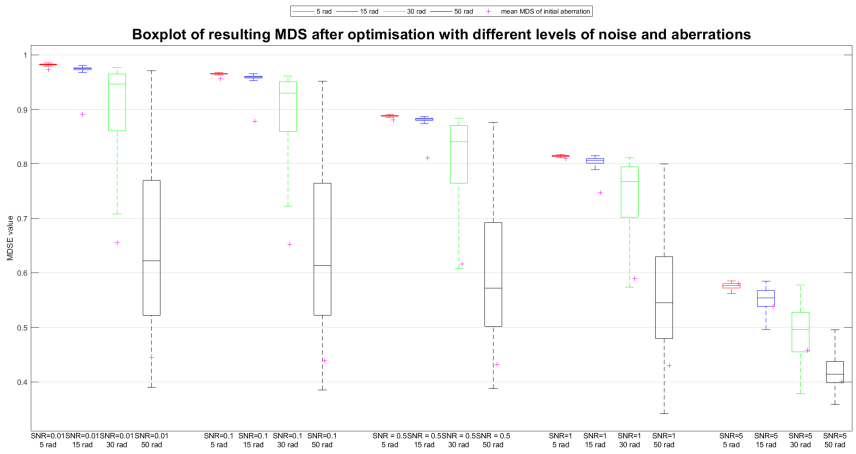


**Figure 10-5:** Results for the residual MDS for the simulations of the SMBA.

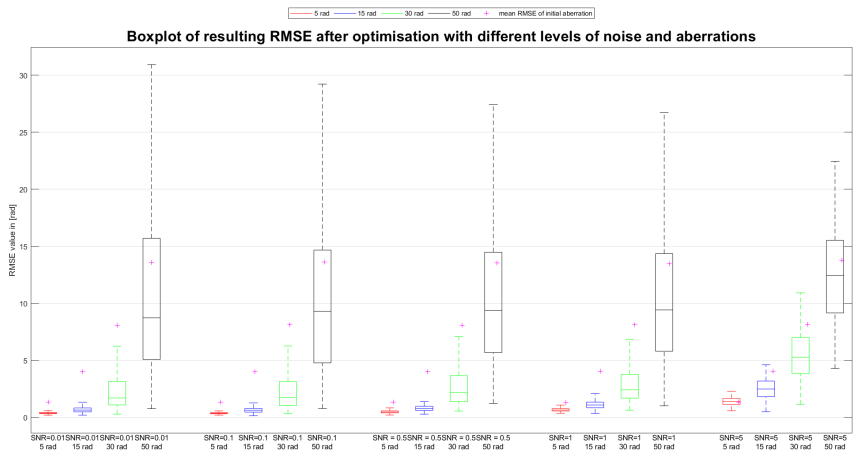


**Figure 10-6:** Results for the residual RMSE for the simulations of the SMBA.

### 10.1.2-iii Continuous Model Based Approach

In this section the simulation results for the CMBA will be displayed, which are used for comparison in the discussion. In Figure 10-7 and Figure 10-8 respectively the mean initial metric and RMSE values are plotted in pink and the resulting metric values and RMSE values, after the optimisation, are plotted in the boxplots, for different levels of noise and magnitudes of the aberrations. However, the results plotted in these figures are only results of succesfull convergences of the method, as explained in subsection 9.3.4. The succes rates can be found in Table 10-1, where the bold printed values represent the compared values, as will be explained in the discussion of these success rates.

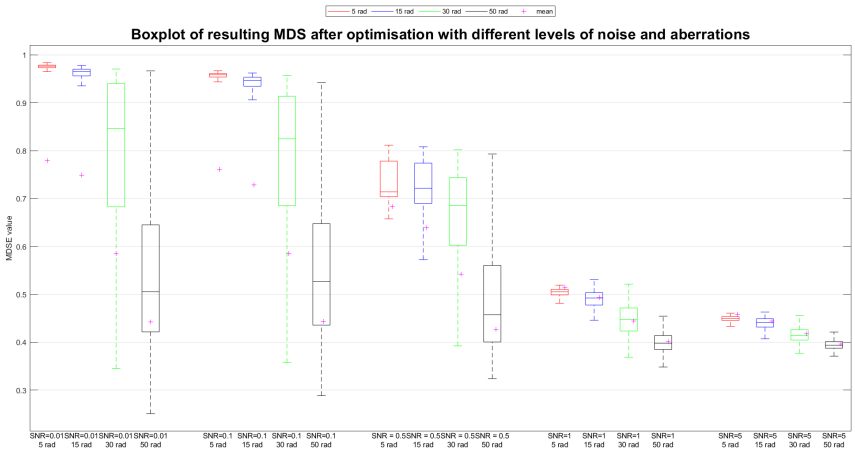


**Figure 10-7:** Results for the residual MDS for the simulations of the CMBA.

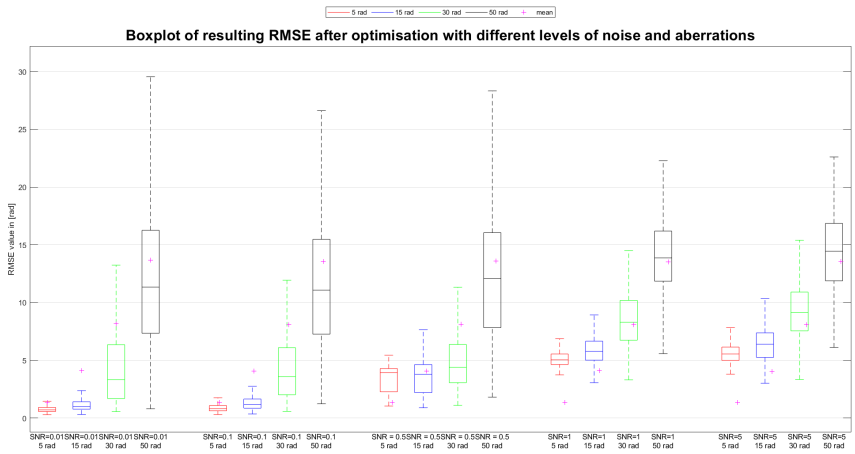


**Figure 10-8:** Results for the residual RMSE for the simulations of the CMBA.

| | | Aberration Magnitude | | | |
|---|---|---|---|---|---|
| | | 5 [rad] | 15 [rad] | 30 [rad] | 50 [rad] |
| SNR | 0.01 | 47.71% | 66.31% | 79.87% | **98.04**% |
| | 0.1 | 48.03% | 65.70% | **86.36**% | **97.85**% |
| | 0.5 | **81.43**% | **95.60**% | **100**% | **100**% |
| | 1 | **100**% | **100**% | **100**% | **100**% |
| | 10 | **100**% | **100**% | **100**% | **100**% |

**Table 10-1:** Percentages of succesfull convergence of the CMBA

### 10.1.3 Overview of the different methods

To get a better overview of the efficiency of the different methods, in Table 10-2 and Table 10-3 an overview is displayed that summarizes the improvement rates for the different approaches for the different levels of noise and initial aberrations. This is done for both the MDS and the RMSE of the initial aberration. It must be noted that the results for the CMBA, only include the succesfull optimisations. This will be further discussed in the Discussion section.

| | | Aberration Magnitude 5 [rad] | | | Aberration Magnitude 15[rad] | | |
|---|---|---|---|---|---|---|---|
| | | GMBA | SMBA | CMBA | GMBA | SMBA | CMBA |
| SNR | 0.01 | 0.58% | 0.94% | 25.19% | 5.81% | 9.43% | 27.68% |
| | 0.1 | 0.57% | 0.97% | 25.68% | 5.60% | 9.17% | 28.60% |
| | 0.5 | 0.51% | 0.86% | 7.20% | 5.21% | 8.59% | 13.51% |
| | 1 | 0.44% | 0.63% | -2.10% | 4.89% | 7.70% | -0.84% |
| | 10 | 0.17% | -0.70% | -2.13% | 2.84% | 2.53% | -1.06% |
| | | Aberration Magnitude 30 [rad] | | | Aberration Magnitude 50[rad] | | |
| | | GMBA | SMBA | CMBA | GMBA | SMBA | CMBA |
| SNR | 0.01 | 21.67% | 37.58% | 37.00% | 30.06% | 46.78% | 22.07% |
| | 0.1 | 21.31% | 36.53% | 34.47% | 31.33% | 46.98% | 24.38% |
| | 0.5 | 19.51% | 31.03% | 22.05% | 26.54% | 38.85% | 14.06% |
| | 1 | 16.61% | 25.72% | 0.55% | 20.95% | 30.18% | 0.15% |
| | 10 | 5.35% | 6.96% | -0.47% | 3.87% | 5.10% | -0.26% |

**Table 10-2:** Overview of the average improvement rates for the MDS of the different approaches for different levels of noise and initial aberration magnitudes

| | | Aberration Magnitude 5 [rad] | | | Aberration Magnitude 15[rad] | | |
|---|---|---|---|---|---|---|---|
| | | GMBA | SMBA | CMBA | GMBA | SMBA | CMBA |
| SNR | 0.01 | -53.26% | -70.29% | -43.01% | -53.20% | -82.88% | -69.90% |
| | 0.1 | -53.40% | -71.00% | -35.52% | -53.83% | -83.27% | -66.09% |
| | 0.5 | -50.90% | -63.43% | 158.05% | -54.76% | -79.55% | -13.01% |
| | 1 | -47.40% | -48.89% | 276.20% | -52.88% | -71.94% | 43.85% |
| | 10 | -23.44% | 4.08% | 319.51% | -37.90% | -37.86% | 58.57% |
| | | Aberration of 30 [rad] | | | Aberration of 50[rad] | | |
| | | GMBA | SMBA | CMBA | GMBA | SMBA | CMBA |
| SNR | 0.01 | -49.20% | -69.65% | -48.35% | -17.24% | -22.52% | -12.52% |
| | 0.1 | -47.45% | -70.44% | -47.12% | -16.42% | -25.35% | -13.69% |
| | 0.5 | -48.18% | -65.46% | -38.20% | -15.65% | -22.47% | -10.77% |
| | 1 | -46.87% | -63.04% | 4.90% | -17.37% | -22.39% | 4.07% |
| | 10 | -29.10% | -32.63% | 14.11% | -9.19% | -10.13% | 6.21% |

**Table 10-3:** Overview of the average improvement rates of the RMSE of the different approaches for different levels of noise and initial aberration magnitudes

## 10.2 Experimental Results

In order to verify the new proposed method, besides simulations, experiments are also conducted. The used setup is described in subsection 9.5.1. For comparison, two known methods will be used, i.e. the GMBA and SMBA. Before the optimisation processes are conducted, first the correlation matrix for this setup must be determined. The resulting matrix is then used in all the different approaches, to minimise the differences between the different experiments. A static aberration is added to the system to validate the efficiency.

### 10.2.1 Empirical Calibration

As described in the literature summary, a large number of system induced errors can be present. These errors can occur due to misalignment, wrong focussing points or errors from the optical elements in the setup. In order to take these errors into account, an online empirical calibration is preferred. Using the described method of subsection 9.1.3 the correlation matrix displayed in Figure 10-9 is obtained.

### 10.2.2 Optimisation of Image Quality

Once the correlation matrix is determined, the optimisation process is executed. In the literature summary, two model based approaches are explained. A comparison is made between these two existing methods and the new method. In subsubsection 10.2.2-i and subsubsection 10.2.2-ii the results of these approaches are displayed. In subsubsection 10.2.2-iii the results of the proposed method are displayed. Before the optimisation algorithms can be implemented, first the proportionality parameter $c_0$ must be tuned, which scales the difference between the initial and excited metric value, see Equation 5-17. The results for this are displayed in the corresponding subsection.

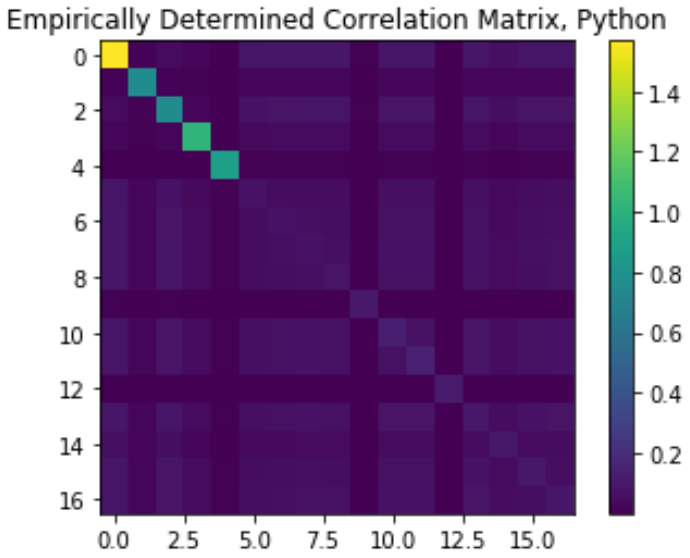


**Figure 10-9:** Experimentally determined Correlation Matrix for the experiments.

### 10.2.2-i General Model Based Approach

First the proportionality parameter $c_0$ must be tuned. In Figure 10-10, the resulting metric value before (red) and after (blue) optimisation are displayed for a fixed aberration with different values for the proportionality parameter. Once the $c_0$-parameter is tuned, the optimisation of the image quality can start. For 50 different random aberrations the mean initial, resulting metric values and the mean improvements in percentage are computed and displayed in Table 10-4. In total 4 runs are performed, each consisting of 50 different aberrations. Also, for every aberration a simple coordinate search algorithm is run, to compute the most optimal and achievable MDS of the aberration. This value is also displayed in Table 10-4, in order to make a comparison, the highest achievable improvement percentage is also computed and presented.

| Run: | Mean Initial MDS | Mean Resulting MDS | Mean Optimal MDS | Mean Improvement % | Mean Max Improvement % |
|---|---|---|---|---|---|
| 1 | 0.8162 | 0.8362 | 0.8949 | 2.4424% | 9.6388% |
| 2 | 0.8399 | 0.8718 | 0.9106 | 3.7978% | 8.4097% |
| 3 | 0.8131 | 0.8328 | 0.8864 | 2.4263% | 9.0218% |
| 4 | 0.7851 | 0.8016 | 0.8538 | 2.1055% | 8.7523% |

**Table 10-4:** Mean experimental results for the initial, resulting and optimal MDS value and the improvement rates for the GMBA.

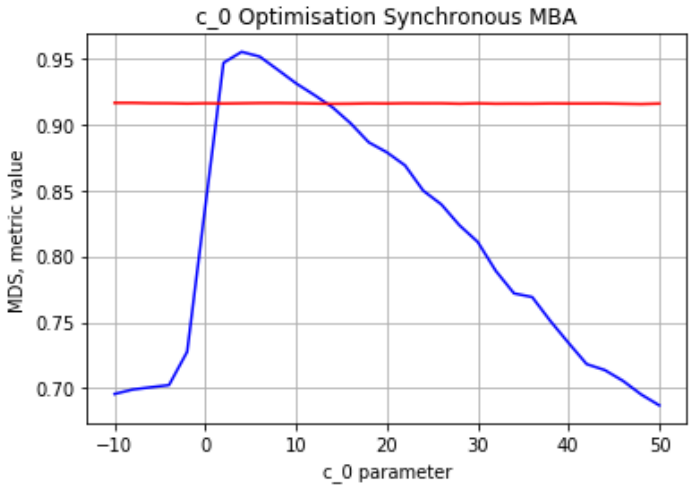


**Figure 10-10:** Experimentally optimised c_0 parameter for the GMBA. In red the metric value of the initial aberration is displayed and in blue the resulting metric value after optimisation.

### 10.2.2-ii Synchronous Model Based Approach

First the proportionality parameter $c_0$ must be tuned. In Figure 10-10, the resulting metric value before (red) and after (blue) optimisation are displayed for a fixed aberration with different values for the proportionality parameter $c_0$. It can be seen that this approach is able to correct and improve the used metric value. Once the proportionality parameter $c_0$ is tuned, the optimisation process can be started for different added random aberrations. The results are presented in Table 10-5.

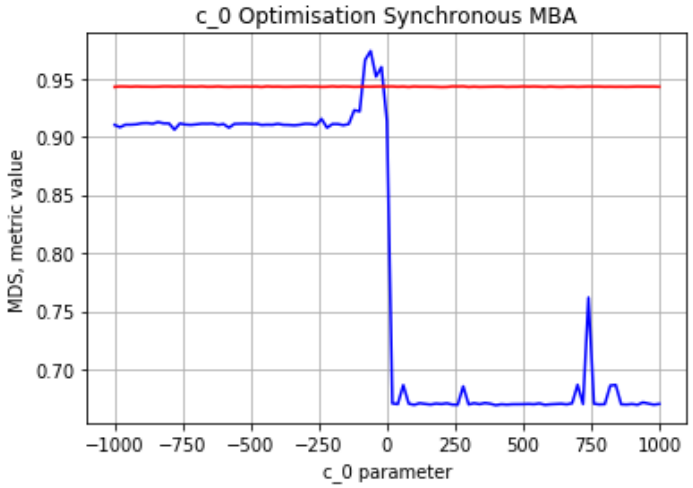


**Figure 10-11:** Experimentally optimised c_0 parameter for the SMBA.

| Run: | Mean Initial MDS | Mean Resulting MDS | Mean Optimal MDS | Mean Improvement % | Mean Max Improvement % |
|---|---|---|---|---|---|
| 1 | 0.8162 | 0.8471 | 0.8949 | 3.7746% | 9.6388% |
| 2 | 0.8399 | 0.8821 | 0.9106 | 5.0201% | 8.4097% |
| 3 | 0.8199 | 0.8356 | 0.8864 | 2.7679% | 9.0218% |
| 4 | 0.7953 | 0.8082 | 0.8538 | 2.9447% | 8.7523% |

**Table 10-5:** Mean experimental results for the initial, resulting and optimal MDS value and the improvement rates for the SMBA. In red the metric value of the initial aberration is displayed and in blue the resulting metric value after optimisation.

#### 10.2.2-iii Continuous Model Based Approach

The CMBA does not converge to a solution. A large number of tests have been done, but there is no value for the proportionality parameter, for which this method converges to a solution. The algorithm computes the projection of the optimal control input and the corresponding MDS, which should by definition be lower than 1 (see Equation B-3). But for the experimental implementation of this approach, the algorithm constantly computes values higher than 1 and these runs are classified as failed runs, see subsection 9.3.4. In chapter 11, this behaviour will be evaluated and compared with simulations, in which more successful runs are observed. Due to the aforementioned reasons, it is not possible to obtain results in the form of Table 10-4 and Table 10-5.

# Chapter 11

# Discussion

In this chapter the results of the simulations and experiments will be discussed. The discussion will be divided into two parts. First, the results of the simulations will be discussed. Next, the experimental results will be discussed.

## 11.1 Simulations

In this section, the results of the simulations will be discussed. First, the empirical calibration results will be evaluated, followed by the evaluation of the optimisation processes. The trends that can be seen in the results of the simulations of the optimisation processes can be divided into the following categories; a difference in magnitude of aberrations, a difference in the level of noise and the differences between the three approaches. Each category will be discussed separately in the following subsections. In the last subsection, the results of the Continuous Model Based Approach (CMBA) will be discussed, here the focus is on the converging percentages of this method.

### 11.1.1 Empirical Calibration

With the empirical calibration procedure, a correlation matrix can be computed. This correlation matrix is displayed in Figure 10-1. It can be seen that the resulting correlation matrix looks similar to the numerically computed correlation matrix of Figure 4-2 (right). In the correlation matrix obtained in the simulations, a lot of details can be found in the off-diagonal parts of the matrix. These details can also be seen in the numerically computed correlation matrix, but some differences can still be observed. The use of the empirically determined correlation matrix in the different optimisation methods yields the expected results; convergence of every method. To compare the methods, the same procedure will be used for all three different optimisation processes. In order to judge the quality of the correlation matrix, a large number of simulations need to be run for comparison. Further research is recommended, as this procedure already yields promising results and optimising the used parameters shall

lead to an increase in the performance.

Besides the optimisation of the different parameters, it is also recommended to look into the inputs that are used for the calibration procedure. This is because the optimal control input is used as an input for the system and is usually not equal to zero. This implies that a different combination of modes can be used (with different magnitudes) and that the combination is not necessarily bounded by the input proposed by Booth [2011]. It is recommended to continue with this research in order to study the effects of different control inputs and different sets of modes that can be used for the calibration procedure.

### 11.1.2 Aberration Magnitudes

Increasing the aberration magnitude has a negative influence on the results of the optimisation processes. The resulting metric values remain smaller and the Root Mean Squared Error (RMSE) of the residual wavefronts remain larger after optimisation. The percentage of improvement is higher for larger aberrations, which can be explained by the fact that the initial aberration is larger. This implies that there is a larger aberration in the initial measurement and thus more aberration to correct for. This explains the higher improvement percentages for the higher initial aberrations in Table 10-2 and Table 10-3. Also, the largest initial aberration (50 [rad]), has a larger range for the residual Masked Detector Signal (MDS) and RMSE. For the largest aberration, the different methods resulted in a mide range of values for the MDS, ranging from 0.35 to 0.95. Which implies that the approaches might find an optimum or fail in the optimisation process. Yet, for all of the methods, the mean resulting MDS and RMSE have improved for the larger aberrations, compared to the mean initial MDS and RMSE.

### 11.1.3 Noise Levels

The level of noise, implemented as the Signal to Noise Ratio (SNR), significantly influences the results of the optimisation processes. It can be seen that the MDS and the RMSE after optimisation degrade, with an increasing level of SNR, for all of the optimisation procedures. Looking at the boxplots in Figure 10-4, Figure 10-6 and Figure 10-8 it can be seen that the mean initial RMSE does not change for higher levels of noise, whilst the resulting RMSE of the residual aberrations degrades for higher levels of SNR. Comparing the values in Table 10-2 and Table 10-3 shows that the noise negatively effects all optimisation methods for all aberrations, as could be expected.

However, the CMBA is effected more significantly than the General Model Based Approach (GMBA) and Synchronous Model Based Approach (SMBA). It can be seen that the CMBA does not improve the quality of the image for higher noise levels, but in some cases it actually results in a decrease of the image quality. This behaviour will be discussed more elaborately in the next subsection, where the CMBA will be evaluated.

### 11.1.4 Continuous Model Based Approach

The results for the CMBA must be processed with caution. Occasionally error build-ups can cause the algorithm to 'fail', as was explained in subsection 9.3.4. It can be seen that these fail-cases occur mainly when the metric value converges to 1 or if the initial value starts close to 1. Due to this characteristic, it can be seen that for the successful runs the initial values for the MDS are lower and the initial mean RMSE of the initial aberration are higher.

For the CMBA, only the combinations of noise and aberration magnitude for which a success rate of approximately 100% was reached can be accurately compared. Combinations with a success rate of 80% or more are used in the analysis, which are marked in bold in Table 10-1. These are the combinations that will be compared in the next subsection.

For the higher noise levels, it can be seen that the CMBA does not correct for the small aberrations (e.g. 5 [rad]). This can be seen in Table 10-3, where relatively large increases in the residual RMSE can be observed, for small aberrations with larger noise levels. The CMBA shows this behaviour when the MDS of the image starts to converge to 1. For higher levels of noise the CMBA does not succeed in optimising the image quality, which can be explained by the method of optimisation. Previous measurements are used to predict the optimal wavefront, which then in turn are used for the computation of optimal control input for the next mode. Any error in the first measurement builds up and causes an integration error in the new computations.

### 11.1.5 Comparison of the Different Approaches

Looking at the resulting RMSE of the residual aberrations and the resulting MDS, it can be seen that the SMBA results in the largest percentage increase, compared to the other two approaches. However, it also uses almost twice the number of measurements, so this must be taken into account as well when comparing the different approaches.

The second best performing approach is the GMBA. Compared to the SMBA, the resulting values of the RMSE and MDS after optimisation of the GMBA have a larger variation and are less concentrated around the mean resulting values, implying that the GMBA is less precise. One reason for this can be the process of the SMBA, in which every mode is updated an optimised after two iterations. The optimised control vector is then used for the optimisation of the next mode. Due to this, the quality of the image increases after every 2 iterations. As was shown in the results of the simulations, less aberrated images will have a better resulting MDS and RMSE. Combined with the increasing image quality during the optimisation process, this might be why the SMBA yields more precise results.

The CMBA does not perform as good as the other two approaches and yields a lot of (so-called) 'failure' runs. These aspects must be weighted against the advantages of decreasing the number of iterations and reducing the frozen window time. These characteristics were required and form the basis of this approach, but due to the non-optimal performance of the procedure, it is highly doubtful if this method will increase the overall performance of the system.

## 11.2 Experiments

The results for the experiments can also be divided into two parts. First, the empirically determined correlation matrix will be discussed. Next, the results for the optimisation processes will be evaluated for all three discussed approaches. The setup for the experiments is discussed in section 9.5.

### 11.2.1 Empirical Calibration

The matrix obtained with the experimental empirical calibration is displayed in Figure 10-9. By comparing it to the matrix obtained with simulations, it can be seen that the values on the diagonal are more present for the first five modes. The ratio of the diagonal values can be compared to the results of the simulations. This ratio can be explained by the rings in which the actuators are positioned and the values of the diagonal show the same ratio as in the simulations. However, the off-diagonal values are different from the simulations. This can be partly explained by the system induced errors, which are the main reason for implementing an online calibration procedure. More details were expected to be present in these regions, since these were observed in both the numerically determined correlation matrix and the correlation matrix from the simulations.

The calibration procedure was not changed between the different tests, such that the tests could be accurately compared. However, it is highly recommended for further research to optimise the calibration procedure, but this is beyond the scope of this thesis project.

Further research on this procedure is recommended, since it shows promising results and is easy to implement on any system which exhibits non-diagonal features in the correlation matrix, i.e. deformable mirrors where the set of actuators correspond to the set that is to be optimised. In further research the efficiency of all the methods could be compared if a Wavefront Sensor (WFS) is incorporated in the system for the computation of the correlation matrix.

### 11.2.2 Optimisation Algorithms

The results of the different optimisation algorithms were not as good as expected, when compared to the simulations. Both the GMBA and SMBA showed an improvement in the metric value, where the SMBA resulted in the largest improvements. However, both methods do not optimise the image quality as well as the Coordinate Search (CS) algorithm, which is used as a ground truth.

The SMBA shows the largest improvement in the metric value, compared to the other two methods. This was also seen in the simulations for any combination of noise and initial aberration magnitude. From the simulations it can also be seen that for some combinations of noise and aberration magnitude the CMBA does not converge to a more optimal solution in terms of the used metric value. This might be one of the reasons why this method does not converge to a solution in the experiments either. If the aberration is too large and the noise

is too large as well, thus potentially explaining the behaviour of the CMBA in experiments.

It is also important to notice that the simulations of the CMBA show that the CMBA fails relatively fast if the metric value is close to one. This was also observed in all the experiments. To overcome this problem, the radius of the mask of the MDS is made smaller, resulting in lower values for the MDS. However, this radius must contain every part of the intensity distribution that is of importance and can thus only be reduced up till a suitably chosen detector radius. Still, for smaller radii and lower initial values for the MDS, the success rate of the CMBA does not improve.

Another reason for the difference between the simulations and real-time experiments might be the CCD camera and its implementation in the simulations. In the experiments, an 8-bit camera is used, which means that its outputs are integers between 0 and 255. In the simulations, the values for the measured PSF are not integers and can take any value. Saturation of the sensor is also not taken into account in the simulations. Therefore, it is one of the main recommendations to take the characteristics of the camera into account for the simulations and compare the different methods, if more research is to be put into this topic.

# Chapter 12

# Conclusion and Recommendations

The goal of this thesis was the design and control of a portable Adaptive Optics (AO) system. A system should be designed that is implementable on very simple AO-systems and make the technology of WFSless AO accessible to a larger audience. In the process a niche in this field of research was found, where the important assumption of the frozen window time is not valid for more dynamic situations and that proposed solutions for this problem require more measurements than the original approach. The new goal was to find a method that reduces the number of measurements, whilst keeping the frozen window time as low as possible. The Continuous Model Based Approach (CMBA) is proposed as a solution. The proof for the CMBA is mathematically worked out. This approach is verified with the use of simulations and experiments. Due to the implementation of real-time experiments, the need for an online calibration procedure rose and a new procedure was proposed. This procedure can be implemented on any system and aims to find the correlation matrix of the set of modes, which can be used in any of the model based approaches.

Tests have been done on both the calibration procedure and the CMBA, using computer simulations and an experimental setup. The results of these tests are presented in chapter 10 and discussed in chapter 11. In this chapter, conclusions will be drawn on both new methods and their advantages and disadvantages will be discussed. First the online calibration procedure will be evaluated, followed by the new approach for the optimisation.

The new online calibration procedure shows promising results. Especially in the simulations, where a reliable correlation matrix is obtained after the calibration procedure. This matrix can be used for the GMBA and after decoupling of the modes with a SVD also for the SMBA. In the experiments, the calibration procedure shows different behaviour. One of the differences is that the values on the diagonal are more present in the experiment for the first 5 modes, compared to the simulations. Next, the off-diagonal values are different. In the simulations, more structured details can be seen in the off-diagonal values, compared to the off-diagonal parts of the correlation matrix obtained in the experiments. In the experimentally obtained correlation matrix, the influence of the system induced aberration is more present. To conclude, it is recommended to further investigate the optimisation of the

control inputs and the parameters of this approach. As it is easy to implement and can be implemented on any system without the need for a WFS. It is also recommended to verify the resulting correlation matrix with an included WFS, instead of comparing the results of the optimisation processes. This will reduce the time and measurements needed for this research.

The results of the optimisation processes show that the new proposed method, the CMBA, works in simulations, but the results are less optimal, compared to the other approaches. In experiments, the error-build-up in the new method seems to be too large to overcome and the method does not work in the experimental setup. These results are also observed in the simulations for combinations of (higher) noise and (larger) aberrations and this might cause the CMBA to fail in finding the optimal solution.

Another reason for the difference between the simulations and experiments is the implementation of the CCD camera in the simulations. The CMBA might be successful in the simulations, due to the more precise approximation of the PSF, compared to the real time experiments, where a bit-depth of 255 bits is used. It is recommended to check this more thoroughly, by simulating the camera. Lastly, the used approach for acquiring the correlation matrix might cause the CMBA to fail in finding the optimal solution, so it is recommended to compare this approach with predetermined and correct correlation matrices, obtained with an incorporated WFS.

For further research it is recommended to test the different optimisation processes with more different aberrations, such as dynamic aberrations or static aberrations with extended objects as the image source. For these dynamic aberrations the MATLAB toolbox OOMAO [Conan and Correia, 2014] is recommended. For the extended object, the known optimisation algorithms (GMBA and SMBA) have been implemented and shown to work in some preliminary simulations, but more research is needed for this implementation.

To conclude and summarise the results of this research, it was shown that the CMBA can be implemented in simulations, yet is unable to converge to an optimal solution in experiments. The CMBA does not improve the image quality in real time experiments, compared to known methods, such as the GMBA and the SMBA. The online calibration procedure shows promising results and can be implemented on simple systems, such as telescopes used by (amateur) astronomers. This calibration procedure accounts for the system induced error of any system and can be used for systems with off-diagonal elements in the correlation matrix, such as systems with a DM. This approach does not increase the cost of the system and will contribute to making this part of science more accessible for anyone.

# Appendices

# Appendix A

# Proportionality Mean Squared Gradient and Intensity Distribution

This Appendix shows the derivation proposed in [Yang et al., 2015]. It shows the proportionality of the intensity distribution to the mean squared gradient. Starting with the PSF of the aberrated pupil function

$$I(\mathbf{u}) = |\mathcal{F}(aP(\mathbf{x})e^{-i\phi(\mathbf{x})})|^2 \equiv |\mathcal{F}(A(\mathbf{x}))|^2, \tag{A-1}$$

where $P(\mathbf{x})$ is the unaberrated pupil function, which is one when inside the lens aperture and zero if it outside the aperture. Also $A(\mathbf{x}) = aP(\mathbf{x})e^{-i\phi(\mathbf{x})}$ and the object function is defined as: $o(\boldsymbol{\xi}) = a\delta(\boldsymbol{\xi})$. Using the Fourier property:

$$\mathcal{F}(f \star g) = \mathcal{F}(f)^* \cdot \mathcal{F}(g), \tag{A-2}$$

where the $\star$ denotes the cross correlation and the $^*$ denotes the complex conjugate. The next thing that is used is

$$\mathcal{F}(f'_x(\mathbf{x})) = 2\pi i u \mathcal{F}(f(\mathbf{x})), \tag{A-3}$$

where the above equations are all combined into

$$\begin{aligned} I(\mathbf{u})\mathbf{u}^2 &= |\mathcal{F}(A(\mathbf{x}))|^2\mathbf{u}^2 && \text{(A-4)}\\ &= \mathcal{F}(A(\mathbf{x})\mathbf{u})^*\mathcal{F}(A(\mathbf{x})\mathbf{u}) && \text{(A-5)}\\ &= -\frac{1}{2\pi i}\mathcal{F}(A'_x(\mathbf{x}))^*\frac{1}{2\pi i}\mathcal{F}(A'_x(\mathbf{x})) && \text{(A-6)}\\ &= \frac{1}{4\pi^2}\mathcal{F}(A'_x(\mathbf{x}) \star A'_x(\mathbf{x})). && \text{(A-7)} \end{aligned}$$

Now the following property is used:

$$\int_{\mathbb{R}^2} \mathcal{F}(f)(\mathbf{u})\mathrm{d}\mathbf{u} = f(0) \tag{A-8}$$

The goal is to show that the integral of the Second-Moment (SM) of the intensity distribution is proportional to Mean Squared Gradient (MSG). Here it is used that the Fourier transform of $A(\mathbf{x})$ results in a coordinate change to the angular coordinates.

$$\int_{\mathbb{R}^2} I(\mathbf{u})\mathbf{u}^2 \mathrm{d}\mathbf{u} = \int_{\mathbb{R}^2} \frac{1}{4\pi^2} \mathcal{F}(A'_x(\mathbf{x}) \star A'_x(\mathbf{x})) \mathrm{d}\mathbf{u} \tag{A-9}$$

$$= \frac{1}{4\pi^2} (A'_x \star A'_x)(0) \tag{A-10}$$

$$= \frac{1}{4\pi^2} \int_{\mathbb{R}^2} (A'_x(\mathbf{x}) \cdot A'_x(\mathbf{x}+0)) \mathrm{d}\mathbf{x} \tag{A-11}$$

$$= \frac{1}{4\pi^2} \int_{\mathbb{R}^2} |A'_x(\mathbf{x})|^2 \mathrm{d}\mathbf{x}. \tag{A-12}$$

Rewriting $|A'_x(\mathbf{x})|^2$, in order to substitute it later, using $A(\mathbf{x}) = aP(\mathbf{x})e^{-i\phi(\mathbf{x})}$ yields

$$|A'_x(\mathbf{x})|^2 = |aP'_x(\mathbf{x})e^{-i\phi(\mathbf{x})} - i\phi'_x(\mathbf{x})aP(\mathbf{x})e^{-i\phi(\mathbf{x})}|^2 \tag{A-13}$$

$$= |A(\mathbf{x})|^2 \left| \left( \frac{P'_x(\mathbf{x})}{P(\mathbf{x})} - i\phi'_x(\mathbf{x}) \right) \right|^2 \tag{A-14}$$

$$= aP(\mathbf{x})aP(\mathbf{x})e^{-i\phi(\mathbf{x})}e^{i\phi(\mathbf{x})} \left( \left( \frac{P'_x(\mathbf{x})}{P(\mathbf{x})} \right)^2 + (\phi'_x(\mathbf{x}))^2 \right) \tag{A-15}$$

$$= a^2 \left( P'_x(\mathbf{x})^2 + P(\mathbf{x})^2 \phi'_x(\mathbf{x})^2 \right). \tag{A-16}$$

Substituting Equation A-12 yields

$$\int_{\mathbb{R}^2} I(\mathbf{u})\mathbf{u}^2 \mathrm{d}\mathbf{u} = \frac{1}{4\pi^2} \int_{\mathbb{R}^2} a^2 \left( P'_x(\mathbf{x})^2 + P(\mathbf{x})^2 \phi'_x(\mathbf{x})^2 \right) \mathrm{d}\mathbf{x}. \tag{A-17}$$

For PSF's (apertures in $P(\mathbf{x})$) with sharp boundaries the first part of the above integral won't converge. This problem can be overcome using the following steps. First an unaberrated PSF is denoted as $\phi(\mathbf{x}) = const.$ Then it can be said that two parts arise. One part that is constant and the second part that is variable and dependent on the gradient of the aberration. The first part can be written as the unaberrated intensity distribution

$$\int_{\mathbb{R}^2} (P'_x(x)^2) \mathrm{d}\mathbf{x} = \int_{\mathbb{R}^2} I_0(\mathbf{u})\mathbf{u}^2 \mathrm{d}\mathbf{u}. \tag{A-18}$$

$$\int_{\mathbb{R}^2} I(\mathbf{u})\mathbf{u}^2 \mathrm{d}\mathbf{u} = \int_{\mathbb{R}^2} I_0(\mathbf{u})\mathbf{u}^2 \mathrm{d}\mathbf{u} + \frac{a^2}{4\pi^2} \int_{\mathbb{R}^2} \left( P(\mathbf{x})\phi'_x(\mathbf{x}) \right)^2 \mathrm{d}\mathbf{x}, \tag{A-19}$$

$$\int_{\mathbb{R}^2} \left( I(\mathbf{u}) - I_0(\mathbf{u}) \right) \mathbf{u}^2 \mathrm{d}\mathbf{u} = \frac{a^2}{4\pi^2} \int_{\mathbb{R}^2} \left( P(\mathbf{x})^2 \phi'_x(\mathbf{x}) \right)^2 \mathrm{d}\mathbf{x} \tag{A-20}$$

$$= \frac{a^2}{4\pi^2} \int_{\mathbb{R}^2} P(\mathbf{x})^2 \left| \bigtriangledown \phi(\mathbf{x}) \right|^2 \mathrm{d}\mathbf{x}. \tag{A-21}$$

The last step is to normalise this using the total power

$$\int_{\mathbb{R}^2} I(\boldsymbol{u}) \mathrm{d}\boldsymbol{u} = \int_{\mathbb{R}^2} I_0(\boldsymbol{u}) \mathrm{d}\boldsymbol{u} = \int_{\mathbb{R}^2} o(\xi)^2 \mathrm{d}\xi \int_{\mathbb{R}^2} P^2(x) \mathrm{d}x, \tag{A-22}$$

$$\frac{\int_{\mathbb{R}^2} \left( I(\boldsymbol{u}) - I_0(\boldsymbol{u}) \right) |\boldsymbol{u}|^2 \mathrm{d}\boldsymbol{u}}{\int_{\mathbb{R}^2} I(\boldsymbol{u}) \mathrm{d}\boldsymbol{u}} = \frac{1}{4\pi^2} \frac{\int_{\mathbb{R}^2} \left( P(x)\varphi'_x(x) \right)^2 \mathrm{d}x}{\int_{\mathbb{R}^2} P^2(x) \mathrm{d}x}. \tag{A-23}$$

# Appendix B

# Derivation MDS and MDSE

In this appendix a summary will be presented on the derivation of the Masked Detector Signal and the Masked Detector Signal for Extended Objects based on the derivation of [Yang et al., 2015]. It is an important derivation for this thesis as it forms the bases of the working principle of the Model-Based approach in chapter 5 and chapter 6. Also chapter 8 is based on this derivation. The most important parts will be explained in this appendix in three steps. First, using Appendix A, the Masked Detector Signal (MDS) will be computed for a point source. Then, following the same structure as [Yang et al., 2015], this is done for a point source with any arbitrary coordinates and at last an extended object will be used to come up with the Masked Detector Signal for Extended Objects (MDSE).

## B.1 Masked Detector signal for a Centered Point Source

Using Equation A-23, only one more step is needed to come up with the MDS. In [Booth, 2007] and [Yang et al., 2015], it is suggested that only a certain radius of the intensity measurement should be taken into account and a so-called detector radius is introduced as

$$m(r) = \begin{cases} (1 - \frac{r^2}{R^2}) & \text{if} \quad |r| \leq R \\ 0 & \text{if} \quad |r| > R, \end{cases} \tag{B-1}$$

where $r$ is equal to the distance from the centre to the measured point

$$r = \sqrt{(x - x_0)^2 + (y - y_0)^2}. \tag{B-2}$$

Using this mask instead of $|u|^2$ yields

$$\text{MDS} = \frac{\iint_{\mathbb{R}^2} I(\boldsymbol{u}) \left(1 - \frac{|r|^2}{R^2}\right) \mathrm{d}\boldsymbol{u}}{\iint_{\mathbb{R}^2} I(\boldsymbol{u}) \mathrm{d}\boldsymbol{u}}. \tag{B-3}$$

## B.2 Proportionality of Intensity Distribution of a Point Source with Arbitrary Coordinates

In this section the important steps of this derivation will be summarized, as these are needed for the next section, in which a metric for an extended object will be derived. First, an unaberrated point source is introduced with coordinates that are not on the optical axis, which is related to the unaberrated central point source by

$$I_{0,\boldsymbol{\xi}}(\boldsymbol{u}) = I_0(\boldsymbol{u}-\boldsymbol{\xi}) = \left|\mathcal{F}(aP(\boldsymbol{x})\mathrm{e}^{-ik\boldsymbol{\xi}\boldsymbol{x}})\right|^2. \tag{B-4}$$

Then a very important assumption is stated on aberrations that introduce tip or tilt. As these aberrations would be indistinguishable from a point source with any coordinates that are not on the optical axis, they are excluded from the derivation and it is assumed that the average gradient in x- and y-direction is equal to zero. Then, the aberrated shifted point source is introduced with

$$I_{\xi}(\boldsymbol{u}) = I(\boldsymbol{u}-\boldsymbol{\xi}) \equiv \left|\mathcal{F}\left(aP(\boldsymbol{x})\mathrm{e}^{-\mathrm{i}(\varphi(x)+k\boldsymbol{\xi}\cdot\boldsymbol{x})}\right)\right|^2. \tag{B-5}$$

Using the same approach as the derivation from Equation A-9 up till Equation A-21, the following steps are proposed in [Yang et al., 2015]:

$$\int_{\mathbb{R}^2} I_{\xi}(\boldsymbol{u})|\boldsymbol{u}|^2 \,\mathrm{d}\boldsymbol{u} = \int_{\mathbb{R}^2} I_0(\boldsymbol{u})|\boldsymbol{u}|^2 \,\mathrm{d}\boldsymbol{u} + \frac{a^2}{4\pi^2}\int_{\mathbb{R}^2}(P(\boldsymbol{x})(\nabla\varphi(\boldsymbol{x}) + k|\boldsymbol{\xi}|))^2 \,\mathrm{d}\boldsymbol{x} \tag{B-6}$$

$$= \int_{\mathbb{R}^2} I_0(\boldsymbol{u})|\boldsymbol{u}|^2 \,\mathrm{d}\boldsymbol{u} + \frac{a^2k^2}{4\pi^2}\int_{\mathbb{R}^2} P^2(\boldsymbol{x})\cdot|\boldsymbol{\xi}|^2 \,\mathrm{d}\boldsymbol{x} \tag{B-7}$$

$$+ \frac{2a^2k}{4\pi^2}\int_{\mathbb{R}^2} P^2(\boldsymbol{x})\cdot|\boldsymbol{\xi}|\nabla\varphi(\boldsymbol{x})\mathrm{d}\boldsymbol{x} + \frac{a^2}{4\pi^2}\int_{\mathbb{R}^2}(P(\boldsymbol{x})\nabla\varphi(\boldsymbol{x}))^2 \,\mathrm{d}\boldsymbol{x} \tag{B-8}$$

$$= \int_{\mathbb{R}^2} I_{0,\xi}(\boldsymbol{u})|\boldsymbol{u}|^2 \,\mathrm{d}\boldsymbol{u} + 0 + \frac{a^2}{4\pi^2}\int_{\mathbb{R}^2}(P(\boldsymbol{x})\nabla\varphi(\boldsymbol{x}))^2 \,\mathrm{d}\boldsymbol{x}, \tag{B-9}$$

which proves the same proportionality between the change in the second moment and the Mean Squared Gradient (MSG) as for the central point source

$$\int_{\mathbb{R}^2} I_{\xi}(\boldsymbol{u})|\boldsymbol{u}|^2 \,\mathrm{d}\boldsymbol{u} - \int_{\mathbb{R}^2} I_{0,\xi}(\boldsymbol{u})|\boldsymbol{u}|^2 \,\mathrm{d}\boldsymbol{u} = \frac{a^2}{4\pi^2}\int_{\mathbb{R}^2}(P(\boldsymbol{x})\nabla\varphi(\boldsymbol{x}))^2 \,\mathrm{d}\boldsymbol{x}. \tag{B-10}$$

It should be taken into account that point sources closer to the edge might not work with this rule, as the detector can only measure in a certain region. The next step is combining this derivation with the assumption on how extended objects are formed.

## B.3 Masked Detector Signal for Extended Objects

For the last step of this derivation point sources are evaluated. The image of a point source can be described by (see Equation 3-1)

$$i(\boldsymbol{u}) = h(\boldsymbol{x}) * o(\boldsymbol{\xi}), \tag{B-11}$$

where $i(\boldsymbol{u})$ is the intensity distribution of the image in the image plane with the coordinates $\boldsymbol{u} = (u, v)$. $h(\boldsymbol{x})$ represents the Point Spread Function (PSF) of the aberration in the pupil plane with the coordinates $\boldsymbol{x} = (x, y)$ and $o(\boldsymbol{\xi})$ is the (true) intensity distribution of the object in the object plane with the coordinates $\boldsymbol{\xi} = (\xi, \eta)$. The $*$ denotes a convolution operator.
As the image is formed of a convolution of the PSF and the object intensity distribution, every point in the image can be seen as a point source and the image can be made of the superposition of the images of all point sources [Yang et al., 2015]. This superposition can be used to represent an (unaberrated) image

$$i_0(\boldsymbol{u}) = \int_{\mathbb{R}^2} I_{0,\boldsymbol{\xi}}(\boldsymbol{\xi}) \mathrm{d}\boldsymbol{\xi}. \tag{B-12}$$

Now using the superposition of all point sources, the intensity can be computed. First summing up the intensity for every point source individually and the adding all point sources up, one obtains the difference in the total intensity. This is the same relation as before and can thus be used to compute the MSG. This can be summarised by

$$\begin{aligned} \int_{\mathbb{R}^2} \left(i(\boldsymbol{u}) - i_0(\boldsymbol{u})\right) |\boldsymbol{u}|^2 \mathrm{d}\boldsymbol{u} &= \int_{\mathbb{R}^2} \int_{\mathbb{R}^2} \left(I_{\boldsymbol{\xi}}(\boldsymbol{u}) - I_{0,\boldsymbol{\xi}}(\boldsymbol{u})\right) |\boldsymbol{u}|^2 \mathrm{d}\boldsymbol{u} \mathrm{d}\boldsymbol{\xi} \\ &= \frac{1}{4\pi^2} \int_{\mathbb{R}^2} o(\boldsymbol{\xi}) \mathrm{d}\boldsymbol{\xi} \int_{\mathbb{R}^2} (P(\boldsymbol{x}) |\nabla \varphi|)^2 \mathrm{d}\boldsymbol{x}. \end{aligned} \tag{B-13}$$

The last step in this derivation is the conversion to a suitable metric. In [Yang et al., 2015], the Masked Detector Signal for Extended Objects (MDSE) is introduced, to be distinguished from the MDS and it is computed by normalising Equation B-13 with the total power of the intensity, which can be computed with

$$\int_{\mathbb{R}^2} \left(i(\boldsymbol{u})\right) |\boldsymbol{u}|^2 \mathrm{d}\boldsymbol{u} = \int_{\mathbb{R}^2} \left(i_0(\boldsymbol{u})\right) |\boldsymbol{u}|^2 \mathrm{d}\boldsymbol{u} = \int_{\mathbb{R}^2} o(\boldsymbol{\xi}) \mathrm{d}\boldsymbol{\xi} \int_{\mathbb{R}^2} P(\boldsymbol{x})^2 \mathrm{d}\boldsymbol{x}. \tag{B-14}$$

Now the MDSE can be defined as Equation 8-2 and the Equation 8-3 is obtained.

# Appendix C

# Zernike Polynomials

In Figure C-1 and Figure C-7 the Zernike polynomials are plotted. In Figure C-2 the LB polynomials are plotted. Table C-1 [Hernández-Gómez et al., 2014] shows a table containing the first 16 Zernike polynomials, index-numbering and their formulas.
In Figure C-3 and Figure C-4 the DM representations of the Zernike and LB polynomials are plotted using the small aperture. In section 4.5, it is described how the LB polynomials are computed and in section 4.6 the method of obtaining the DM approximations is discussed. From the polynomials and their DM representations, also the correlations matrices are computed, they can be found in Figure C-5 and Figure C-6. The acquisition of these matrices is discussed in section 4.2, in Equation 4-2 and Equation 4-3.

| **Name** | **Index** | **Formula** |
|---|---|---|
| Piston | $\mathcal{Z}_0^0$ | $1$ |
| tip | $\mathcal{Z}_1^1$ | $x$ |
| tilt | $\mathcal{Z}_1^{-1}$ | $y$ |
| defocus | $\mathcal{Z}_2^0$ | $2x^2 + 2y^2 - 1$ |
| primary astigmatism | $\mathcal{Z}_2^2$ | $x^2 - y^2$ |
| primary astigmatism | $\mathcal{Z}_2^{-2}$ | $2xy$ |
| coma | $\mathcal{Z}_3^1$ | $3x^3 + 3y^2x - 2x$ |
| coma | $\mathcal{Z}_3^{-1}$ | $3y^3 + 3x^2y - 2y$ |
| trefoil | $\mathcal{Z}_3^3$ | $x^3 - 3xy^2$ |
| trefoil | $\mathcal{Z}_3^{-3}$ | $3x^2y - y^3$ |
| spherical | $\mathcal{Z}_4^0$ | $6x^4 + 12y^2x^2 - 6x^2 + 6y^4 - 6y^2 + 1$ |
| fifth order astigmatism | $\mathcal{Z}_4^2$ | $4x^4 - 3x^2 - 4y^43y^2$ |

**Table C-1:** Zernike polynomials, expressions, indexing and numbering of first 16 polynomials

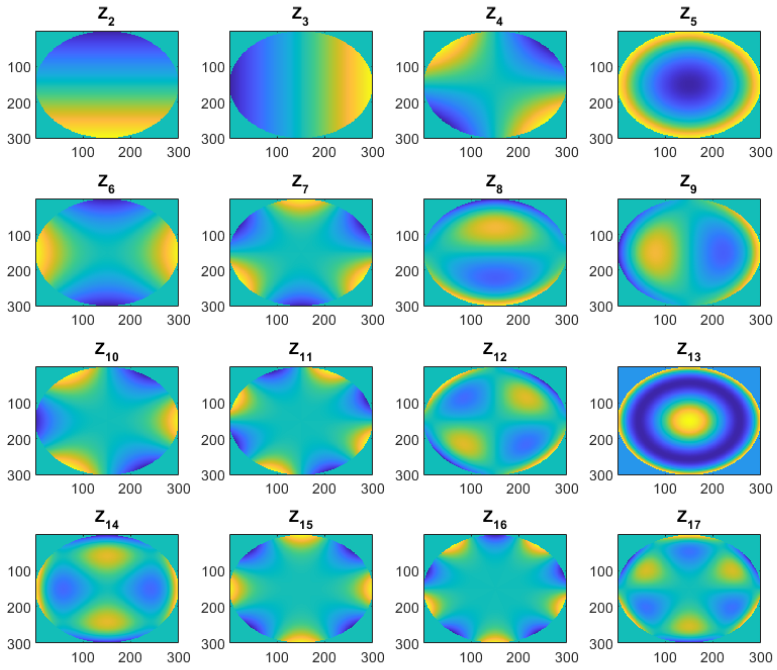


**Figure C-1:** Flat plots of first 16 Zernike polynomials

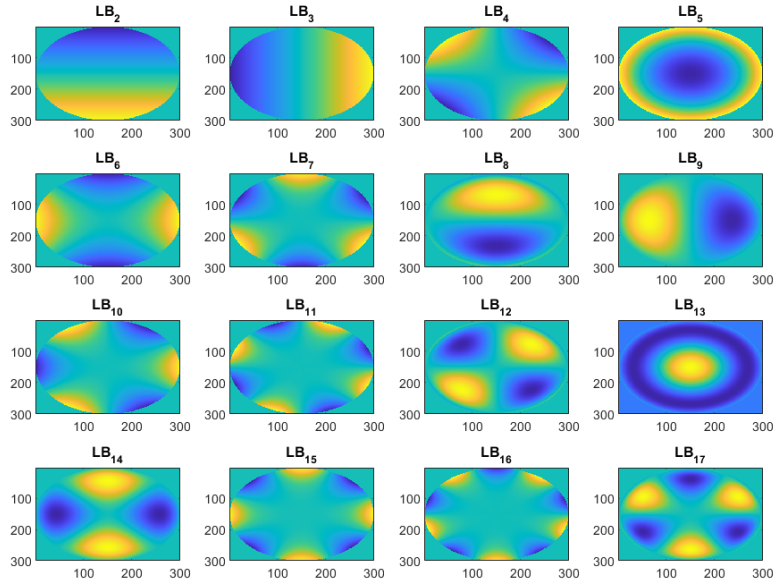


**Figure C-2:** Flat plots of first 16 LB polynomials

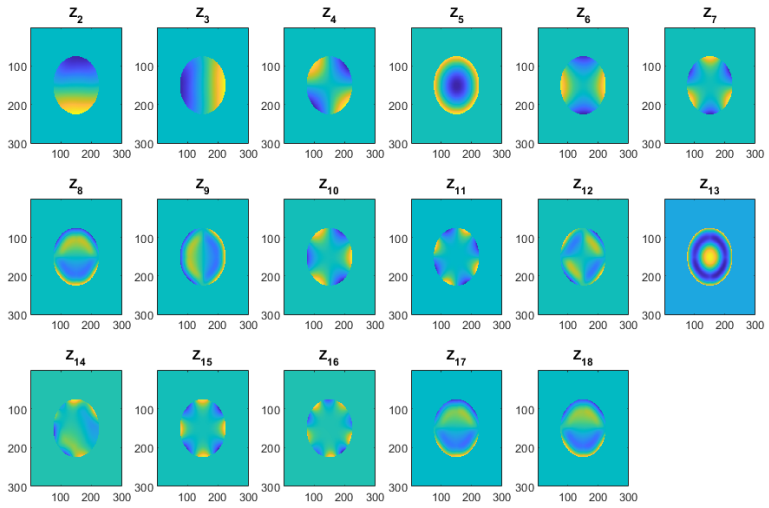


**Figure C-3:** Approximation of the Zernike Polynomials by the 17 actuator MMDM, using the small aperture.

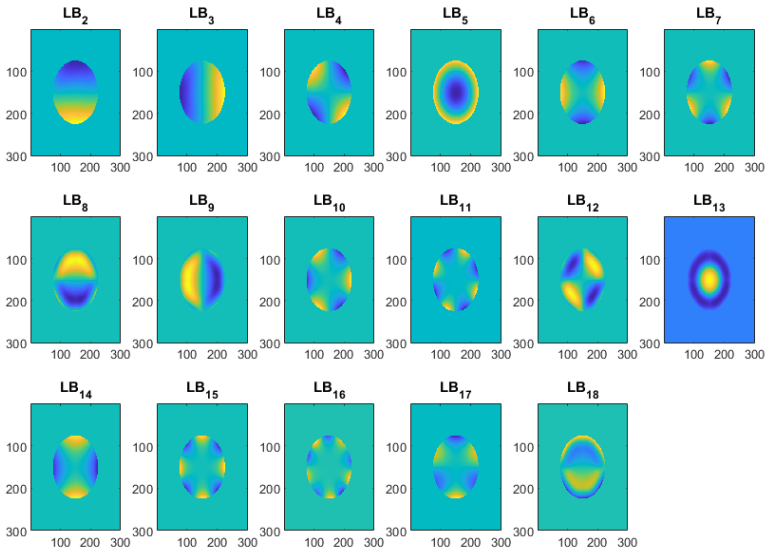


**Figure C-4:** Approximation of the LB Polynomials by the 17 actuator MMDM, using the small aperture.

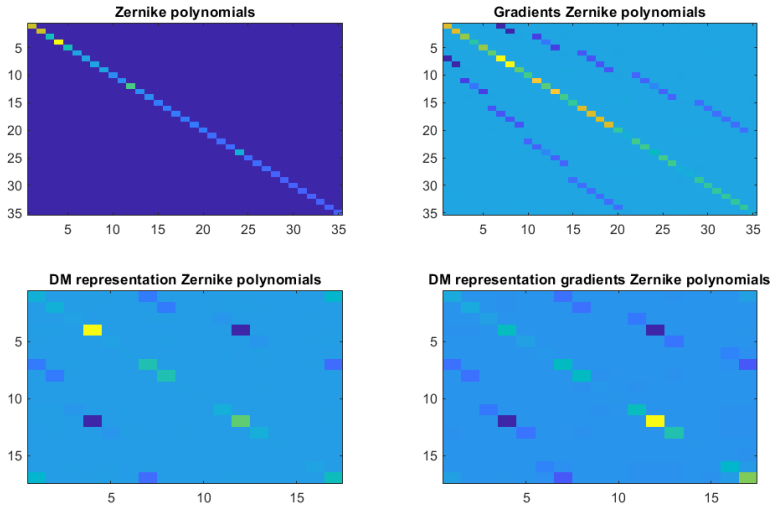


**Figure C-5:** In this figure four correlation matrices are plotted. In the top left corner the correlation matrix of the Zernike polynomials is plotted. In the top right corner the correlation matrix of the gradients and in the bottom left, the correlation matrix of the representations by the DM and in the bottom right figure, the correlation matrix of the gradients of the representations is plotted.

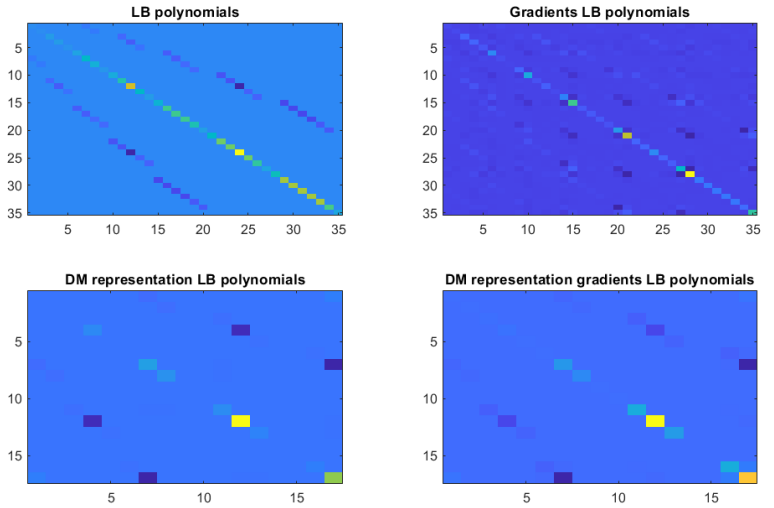


**Figure C-6:** In this figure four correlation matrices are plotted. In the top left corner the correlation matrix of the LB polynomials is plotted. In the top right corner the correlation matrix of the gradients and in the bottom left, the correlation matrix of the representations by the DM and in the bottom right figure, the correlation matrix of the gradients of the representations is plotted.

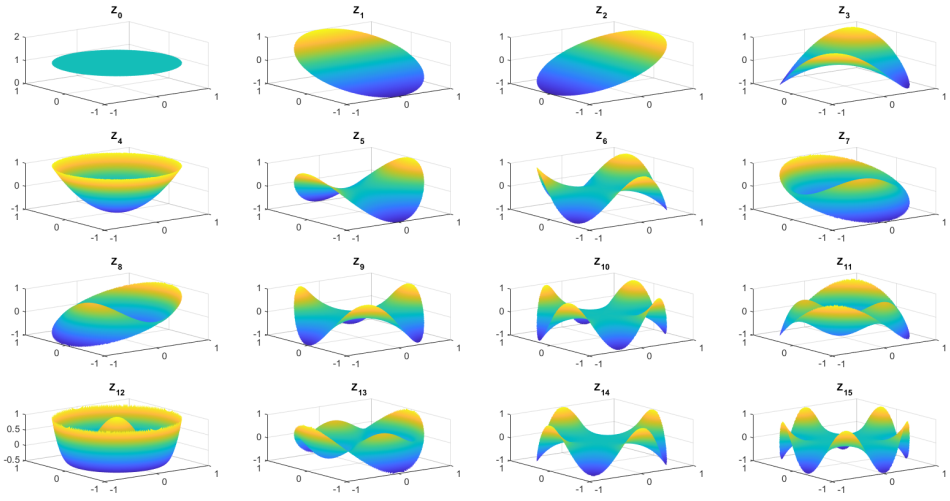


**Figure C-7:** Surface plots of first 16 Zernike polynomials

# Appendix D

# Least Squares Approximation

In order to approximate the wavefront with a DM, the least squares approximation can be used [Verhaegen and Verdult, 2007] to find the control vector that approximates the wavefront in the most 'correct' way. In order to do this, the following minimisation problem must be solved:

$$\boldsymbol{v}_\psi = \arg \min_{\boldsymbol{v} \in [-1,1]^N} \|\psi - \varphi(\boldsymbol{v})\|_2^2 \tag{D-1}$$

where $\psi$ represents the incoming wavefront and $\varphi(\boldsymbol{v})$ the delay introduced by the Deformable Mirror (DM). This delay can be represented by $\varphi = \sum_{i=1}^{N} \nu_i F_i(x,y)$, where every column in $F_i(x,y)$ represents a mode of a set that is chosen in advance and $(x,y)$ are coordinates on the DM. The set of actuator responses or an orthogonal base can be used for the set. The choice for this set is dependent on the usage of the system and is discussed in chapter 4. The coefficients $\nu_i$ are coefficients of the control vector and the goal is to find the most optimal combination of these coefficients.

$$\boldsymbol{v}_\psi = \arg \min_{\boldsymbol{v} \in [-1,1]^N} (\boldsymbol{\psi} - \sum_{i=1}^{N} \nu_i F_i(x,y))^T (\boldsymbol{\psi} - \sum_{i=1}^{N} \nu_i F_i(x,y)) \tag{D-2}$$

This can be written in vector and matrix notation, by substituting

$$\sum_{i=1}^{N} v_i F_i(x,y) = \boldsymbol{F}\boldsymbol{v} \tag{D-3}$$

yields

$$\boldsymbol{v}_\psi = \arg \min_{\boldsymbol{v} \in [-1,1]^N} (\boldsymbol{\psi} - \boldsymbol{F}\boldsymbol{v})^T (\boldsymbol{\psi} - \boldsymbol{F}\boldsymbol{v}) \tag{D-4}$$

There are two ways of computing the most optimal control vector. Both are discussed in [Verhaegen and Verdult, 2007]. The first computes the derivative wrt the control vector and equals it to zero to find the most optimal solution. The second method uses the Schur Complement to find the most optimal control vector. In order to do so, first the column rank of the matrix $\boldsymbol{F}$ must be checked.

## D.1 Computing the Optimal Solution Using the derivative

Calculating the derivative w.r.t. $\boldsymbol{v}$, and setting this equal to zero yields the least squares solution:

$$\frac{\partial}{\partial v}(\boldsymbol{\psi} - \boldsymbol{F}\boldsymbol{v})^T(\boldsymbol{\psi} - \boldsymbol{F}\boldsymbol{v}) = 0 \tag{D-5}$$

$$\frac{\partial}{\partial v}(\boldsymbol{\psi}^T\boldsymbol{\psi} - \boldsymbol{\psi}^T\boldsymbol{F}\boldsymbol{v} - (\boldsymbol{F}\boldsymbol{v})^T\boldsymbol{\psi} + (\boldsymbol{F}\boldsymbol{v})^T\boldsymbol{F}\boldsymbol{v}) = 0 \tag{D-6}$$

$$2\boldsymbol{F}^T\boldsymbol{F}\boldsymbol{v} - 2\boldsymbol{F}^T\boldsymbol{\psi} = 0 \tag{D-7}$$

$$\boldsymbol{F}^T\boldsymbol{F}\boldsymbol{v} = \boldsymbol{F}^T\boldsymbol{\psi} \tag{D-8}$$

$$\boldsymbol{v} = (\boldsymbol{F}^T\boldsymbol{F})^{-1}\boldsymbol{F}^T\boldsymbol{\psi} \tag{D-9}$$

## D.2 Computing the Optimal Solution Using the Schur Complement

The second (and more elegant) way of computing the optimal solution is by using the Schur complement and completion of squares [Kailath et al., 2000]. First, the rank of the matrix $\boldsymbol{F}$ must be checked and it is full rank for this set. Then, again, the optimisation problem of Equation D-4 must be solved. Then the term $(\boldsymbol{\psi} - \boldsymbol{F}\boldsymbol{v})^T(\boldsymbol{\psi} - \boldsymbol{F}\boldsymbol{v})$ is rewritten into

$$(\boldsymbol{\psi} - \boldsymbol{F}\boldsymbol{v})^T(\boldsymbol{\psi} - \boldsymbol{F}\boldsymbol{v}) = \boldsymbol{\psi}^T\boldsymbol{\psi} - \boldsymbol{\psi}^T\boldsymbol{F}\boldsymbol{v} - (\boldsymbol{F}\boldsymbol{v})^T\boldsymbol{\psi} + (\boldsymbol{F}\boldsymbol{v})^T\boldsymbol{F}\boldsymbol{v} \tag{D-10}$$

$$= \begin{bmatrix} 1 & \boldsymbol{v}^T \end{bmatrix} \underbrace{\begin{bmatrix} \boldsymbol{\psi}^T\boldsymbol{\psi} & -\boldsymbol{\psi}^T \\ -\boldsymbol{v}^T\boldsymbol{F}^T\boldsymbol{\psi} & \boldsymbol{v}^T\boldsymbol{F}^T\boldsymbol{F}\boldsymbol{v} \end{bmatrix}}_{M} \begin{bmatrix} 1 \\ \boldsymbol{v} \end{bmatrix}. \tag{D-11}$$

Now the Schur Complement can be used to rewrite the matrix $M$ in the last expression into

$$M = \begin{bmatrix} I & -\hat{\boldsymbol{v}} \\ 0 & I \end{bmatrix} \begin{bmatrix} \boldsymbol{\psi}^T\boldsymbol{\psi} - \boldsymbol{\psi}^T\boldsymbol{F}\hat{\boldsymbol{v}} & 0 \\ 0 & \boldsymbol{F}^T\boldsymbol{F} \end{bmatrix} \begin{bmatrix} I & 0 \\ -\hat{\boldsymbol{v}} & I \end{bmatrix}, \tag{D-12}$$

where $\hat{\boldsymbol{v}}$ must satisfy

$$\boldsymbol{F}^T\boldsymbol{F}\hat{\boldsymbol{v}} = \boldsymbol{F}^T\boldsymbol{\psi}. \tag{D-13}$$

With this expression, the minimisation problem of Equation D-4 can be rewritten into

$$\arg\min_{\boldsymbol{v}\in[-1,1]^N}(\boldsymbol{\psi} - \boldsymbol{F}\boldsymbol{v})^T(\boldsymbol{\psi} - \boldsymbol{F}\boldsymbol{v}) = (\boldsymbol{\psi}^T\boldsymbol{\psi} - \boldsymbol{\psi}^T\boldsymbol{F}\hat{\boldsymbol{v}}) - (\boldsymbol{v} - \hat{\boldsymbol{v}})^T\boldsymbol{F}^T\boldsymbol{F}(\boldsymbol{v} - \hat{\boldsymbol{v}}), \tag{D-14}$$

where a minimum is reached if $\boldsymbol{v} = \hat{\boldsymbol{v}}$, which is (again)

$$\hat{\boldsymbol{v}} = (\boldsymbol{F}^T\boldsymbol{F})^{-1}\boldsymbol{F}^T\boldsymbol{\psi}. \tag{D-15}$$

## D.3 QR-factorisation

To reduce the computational complexity of some systems, a so-called QR-factorisation can be used. This factorisation aims to reduce the dimensions of the system

$$\min_{\boldsymbol{x}}\|A\boldsymbol{x} - b\|, \tag{D-16}$$

where the QR-factorisation of A can be written as

$$A = QR. \tag{D-17}$$

This can be substituted in the part of Equation D-16 that is to be minimised

$$A\boldsymbol{x} = b \tag{D-18}$$
$$QR\boldsymbol{x} = b \tag{D-19}$$
$$Q^T QR\boldsymbol{x} = Q^T b \tag{D-20}$$
$$R\boldsymbol{x} = Q^T b \tag{D-21}$$

$$\underset{\boldsymbol{x}}{min} \|R\boldsymbol{x} - Q^T b\|, \tag{D-22}$$

Then, this minimisation problem can be solved with the least squares approximation for example.

# Bibliography


Martin Booth. Wave front sensor-less adaptive optics: a model-based approach using sphere packings. *Optics Express*, 14(4):1339, 2006. ISSN 1094-4087. doi: 10.1364/oe.14.001339.

Martin Booth and Alexander Jesacher. *Sensorless Adaptive Optics for Microscopy*. 2013. ISBN 9789462036734. doi: 10.1201/b14898-14.

Martin J. Booth. Wavefront sensorless adaptive optics for large aberrations. *Optics Letters*, 32(1):5, 2007. ISSN 0146-9592. doi: 10.1364/ol.32.000005.

Martin J Booth. Self Calibration of Sensorless adaptive optical microscopes. 2011.

R. Conan and C. Correia. Object-oriented Matlab adaptive optics toolbox. *Adaptive Optics Systems IV*, 9148:91486C, 2014. ISSN 1996756X. doi: 10.1117/12.2054470.

Guang-ming Dai. Modal compensation of atmospheric turbulence with the use of Zernike polynomials and Karhunen – Lo ‘ eve functions. 12(10):2182–2193, 1995.

Delphine Debarre, Martin J. Booth, and Tony Wilson. Image based adaptive optics through optimisation of low spatial frequencies. *Optics Express*, 15(13):8176, 2007. ISSN 1094-4087. doi: 10.1364/oe.15.008176.

Delphine Débarre, Edward J. Botcherby, Martin J. Booth, and Tony Wilson. Adaptive optics for structured illumination microscopy. *Optics Express*, 16(13):9290, 2008. ISSN 1094-4087. doi: 10.1364/oe.16.009290.

Delphine Débarre, Biru Wang, Tony Wilson, and Martin J. Booth. Optimum schemes for wavefront sensorless adaptive optics in microscopy. *MEMS Adaptive Optics III*, 7209: 720904, 2009. ISSN 0277786X. doi: 10.1117/12.810512.

David L. Fried. Least-square fitting a wave-front distortion estimate to an array of phase-difference measurements. *Journal of the Optical Society of America*, 67(3):370, 1977. ISSN 0030-3941. doi: 10.1364/josa.67.000370.

Geovanni Hernández-Gómez, Daniel Malacara-Doblado, Zacarías Malacara-Hernández, and Daniel Malacara-Hernández. Modal processing of Hartmann and Shack–Hartmann patterns by means of a least squares fitting of the transverse aberrations. *Applied Optics*, 53(31): 7422, 2014. ISSN 0003-6935. doi: 10.1364/ao.53.007422.

Karel Hinnen. *Data-Driven Optimal Control for Adaptive Optics*. 2007. ISBN 9789090211886. doi: uuid:4f6533b5-eb0a-44af-9e9a-e3252b49f30e. URL http://resolver.tudelft.nl/uuid:4f6533b5-eb0a-44af-9e9a-e3252b49f30e.

Karel Hinnen, Michel Verhaegen, and Niek Doelman. A data-driven H2-Optimal control approach for adaptive optics. *IEEE Transactions on Control Systems Technology*, 16(3): 381–395, 2008. ISSN 10636536. doi: 10.1109/TCST.2007.903374.

Stefan Hippler. Adaptive Optics for Extremely Large Telescopes. 8(2):1–21, 2019. doi: 10.1142/S2251171719500016.

Thomas Kailath, Ali Sayed, and Babak Hassibi. *Linear Estimation*. 2000.

Wen Lianghua, Ping Yang, Yang Kangjian, Chen Shanqiu, Wang Shuai, Liu Wenjing, and Bing Xu. Synchronous model-based approach for wavefront sensorless adaptive optics system. *Optics Express*, 25(17):20584, 2017. ISSN 1094-4087. doi: 10.1364/oe.25.020584.

Huang Linhai and Changhui Rao. Wavefront sensorless adaptive optics: a general model-based approach. *Optics Express*, 19(1):371, 2011. ISSN 1094-4087. doi: 10.1364/oe.19.000371.

Robert J. Noll. Zernike Polynomials and Atmospheric Turbulence. *J Opt Soc Am*, 66(3): 207–211, 1976. ISSN 2375-1037. doi: 10.1364/JOSA.66.000207.

OKO Technologies. 17-Channel Micromachined Deformable Mirror With Built-in Tip-Tilt Stage: Technical Passport. 2011.

Pieter Piscaer, Oleg Soloviev, and Michel Verhaegen. Predictive wavefront sensorless adaptive optics for time-varying aberrations. *Journal of the Optical Society of America A*, 36(11): 1810, 2019. ISSN 1084-7529. doi: 10.1364/josaa.36.001810.

Pieter Piscaer, Oleg Soloviev, and Michel Verhaegen. Phase retrieval of large-scale time-varying aberrations using a non-linear Kalman filtering framework. pages 1–10, 2020.

P. Pozzi, D. Wilding, O. Soloviev, H. Verstraete, L. Bliek, G. Vdovin, and M. Verhaegen. High speed wavefront sensorless aberration correction in digital micromirror based confocal microscopy. *Optics Express*, 25(2):949, 2017. ISSN 1094-4087. doi: 10.1364/oe.25.000949.

Paolo Pozzi, Oleg Soloviev, Dean Wilding, Gleb Vdovin, and Michel Verhaegen. Optimal model-based sensorless adaptive optics for epifluorescence microscopy. *PLoS ONE*, 13(3), 2018. ISSN 19326203. doi: 10.1371/journal.pone.0194523.

François Roddier, editor. *Adaptive Optics in Astronomy*. Cambridge University Press, jun 1999. ISBN 9780521553759. doi: 10.1017/cbo9780511525179. URL https://www.cambridge.org/core/product/identifier/9780511525179/type/book.

Bart De Schutter. Optimization in Systems and Control. (September), 2018.

On Semiconductor. MT9M001: 1/2-Inch Megapixel Digital Image Sensor Features. Technical report. URL www.onsemi.com.

Oleg Soloviev. Alias-free basis for modal sensorless adaptive optics using the second moment of intensity. *International Journal of Wavelets, Multiresolution and Information Processing*, (1):1–17, 2020. ISSN 02196913. doi: 10.1142/S0219691320400081.

H. Song, R. Fraanje, G. Schitter, H. Kroese, G. Vdovin, and M. Verhaegen. Model-based aberration correction in a closed-loop wavefront-sensor-less adaptive optics system. *Optics Express*, 18(23):24070, 2010. ISSN 1094-4087. doi: 10.1364/oe.18.024070.

J Spyromilio. The European Extremely Large telescope : the Arne way. 6986:1–8, 2008. doi: 10.1117/12.801256.

Tatarskii. The effects of the turbulent atmosphere on wave propagation. *Jerusalem: Israel Program for Scientific Translations*, 1971.

G Taylor. The Royal Society is collaborating with JSTOR to digitize, preserve, and extend access to Proceedings of the Royal Society of London. Series A, Mathematical and Physical Sciences. ® www.jstor.org. *Proceedings of the Royal Society of London A*, 313:509–529, 1969.

Michel Verhaegen and Vincent Verdult. *Filtering and system identification: A least squares approach*, volume 9780521875. Cambridge University Press, jan 2007. ISBN 9780511618888. doi: 10.1017/CBO9780511618888.

Michel Verhaegen, Paulo Pozzi, Oleg Soloviev, Gleb Vdovin, and Dean Wilding. Control for High Resolution Imaging. *Control for High Resolution Imaging*, page 247, 2017.

M A Vorontsov and G W Carhart. Adaptive phase-distortion correction based on parallel gradient-descent optimization. 22(12):907–909, 1997.

Biru Wang and Martin J Booth. Optimum deformable mirror modes for sensorless adaptive optics. *Optics Communications*, 282(23):4467–4474, 2009. ISSN 0030-4018. doi: 10.1016/j.optcom.2009.08.010. URL http://dx.doi.org/10.1016/j.optcom.2009.08.010.

Huizhen Yang, Oleg Soloviev, and Michel Verhaegen. Model-based wavefront sensorless adaptive optics system for large aberrations and extended objects. *Optics Express*, 23(19):24587, 2015. ISSN 1094-4087. doi: 10.1364/oe.23.024587.

# Glossary

## List of Acronyms

| | |
|---|---|
| **AO** | Adaptive Optics |
| **WFS** | Wavefront Sensor |
| **DM** | Deformable Mirror |
| **WFSless AO** | Wavefront Sensorless Adaptive Optics |
| **PSF** | Point Spread Function |
| **SM** | Second-Moment |
| **SH** | Shack-Hartmann |
| **CS** | Coordinate Search |
| **SGD** | Stochastic Gradient Descent |
| **MDS** | Masked Detector Signal |
| **MDSE** | Masked Detector Signal for Extended Objects |
| **MSG** | Mean Squared Gradient |
| **PSD** | Power Spectral Density |
| **VAR** | Vector Auto-Regressive |
| **SVD** | Singular Value Decomposition |
| **SH** | Shack-Hartman |
| **GMBA** | General Model Based Approach |
| **SMBA** | Synchronous Model Based Approach |
| **CMBA** | Continuous Model Based Approach |
| **SNR** | Signal to Noise Ratio |
| **RMSE** | Root Mean Squared Error |